9-5-2019

Development of Reduced-Order Models for Engine Applications

Yunchao Wu
University of Connecticut - Storrs, yunchao.wu@uconn.edu

Development of Reduced-Order Models for Engine Applications

Yunchao Wu, Ph.D.

University of Connecticut, 2019

Detailed chemical kinetics is critical for accurate prediction of complex flame behaviors, such as ignition and extinction in engine applications, but difficult to be applied in multi-dimensional flame simulations due to their large sizes. Reduced-order models are needed in such cases to enable high fidelity combustion simulations. This dissertation is focused on developing new model reduction strategies and reduced-order models for engine combustion applications. First, a linearized error propagation (LEP) method for skeletal mechanism reduction is proposed. LEP is based on Jacobian analysis of perfectly stirred reactors (PSR) and can more accurately predict the propagation of small reduction errors compared with the previous methods of directed relation graph (DRG) and DRG with error propagation (DRGEP). Skeletal models generated by using LEP are further validated for auto-ignition and 1-D laminar premixed flames to demonstrate the feasibility of reaction state sampling using only PSR for mechanism reduction. Second, a direct method is developed to accurately and efficiently compute the ignition and extinction turning points of PSR by solving a local optimization problem formulated based on analytic Jacobian. It is shown that the direct method features significantly better accuracy and efficiency compared with the continuation methods that march along the *S*-curves. Third, reduced and skeletal mechanisms for gasoline surrogates with and without ethanol are developed based on a 1389-species detailed mechanism developed by the Lawrence Livermore National Laboratory (LLNL). The skeletal reduction was performed with DRG, sensitivity analysis, isomer lumping, and the time-scale based

reduction is based on linearized quasi-steady-state approximations. The skeletal and reduced mechanisms are extensively validated against the detailed mechanism and available experimental data for ignition delay time and flame speed. The skeletal mechanism is employed in cooperative fuel research engine simulations and the results agree well with experimental data. Lastly, skeletal mechanisms are generated for three gasoline/bio-blend-stock surrogates respectively based on a 2878-species detailed LLNL mechanism for engine simulations. An upgraded solver combining analytical Jacobian and sparse matrix techniques is employed to accelerate the reduction process, such that the reduction time becomes linearly proportional to the mechanism size and a speedup factor of approximately 100 is achieved.

Development of Reduced-Order Models for Engine Applications

Yunchao Wu

B.S., Peking University, 2012

A Dissertation

Submitted in Partial Fulfillment of the

Requirements for the Degree of

Doctor of Philosophy

at the

University of Connecticut

2019

2019

APPROVAL PAGE

Doctor of Philosophy Dissertation

Development of Reduced-Order Models for Engine Applications

Presented by

Yunchao Wu, B.S.

Major Advisor _____
Tianfeng Lu

Associate Advisor _____
Baki Cetegen

Associate Advisor _____
Xinyu Zhao

University of Connecticut
2019

Acknowledgments

Looking back on my Ph.D. journey at UConn, it has been full of thorns and I even thought about quitting the program several times when I was suffering from severe health issues. Fortunately, with the support of my family, colleagues, and friends, I finally recovered from the illness and could complete the degree.

Firstly, I would like to express my sincere gratitude to my advisor Professor Tianfeng Lu for his continuous support and guidance through my Ph.D. studies. He did not give up on me during my most difficult time and his encouragement helped me beat the disease. He is patient, kind and knowledgeable such that I can always get the answer when approaching him for help. I could not imagine having a better advisor for my Ph.D. studies.

I would like to thank Professor Baki Cetegen and Professor Xinyu Zhao for serving in my thesis committee and providing me a lot of insightful comments and feedback. I also want to thank Professor Chih-Jen Sung, Professor Bryan Weber and Professor Claudio Bruno for their suggestions in improving this dissertation.

I thank my fellow lab mates Dr Chao Xu, Dr. Yang Gao, Ji-Woong Park, Shubhangi Bansude, Cong Li, Yufeng Liu, Dr. Ruiqin Shan, Dr. Zhaoyu Luo, Dr. Pengfei Li, Dr. Xianming Wang, Brian Magda and Dr. Mike Kuron for the stimulating discussions, collaborations, and all the fun we have had at UConn.

Words cannot express how grateful I am to my mother Guoping Zhu and my father Lin Wu. My mom took care of me and helped me get through the days when I was in the hospital. Her encouragement accompanied me throughout my Ph.D. studies. My father passed away during my pursuit of the Ph.D. and his guidance during my teenage years is still the source of my power and

courage. Furthermore, I want to thank Xueyan Zhang for her company and support for all these years.

This research has been supported by the National Science Foundation, the US Department of Energy and the Air Force Office of Scientific Research.

List of Figures

List of Tables

Table of Contents

Chapter 1. Introduction

1.1. Motivation

Combustion is a fundamental and essential energy conversion process and is vital to almost every aspect of our daily life. Combustion energy has been a primary energy source to our heating and cooking needs since the ancient time. Combustion of fossil fuels, such as coal, natural gas, gasoline, kerosene, and diesel, has been the major energy source for electricity generation, transportation, and propulsion in modern days. It is shown in Table 1-1 that more than 80% of the global energy consumption in 2018 was attributed to the combustion of fossil fuels [1]. Figure 1-1 further shows BP's energy outlook of the next thirty years [2], that fossil fuels will remain as the major energy source despite the rapid growth in renewable energy sources.

Table 1-1. Global energy consumption by fuel in 2018 [1]

Category	Energy consumption (Mtoe)	Shares (%)
Oil	4662.1	33.62
Natural gas	3309.4	23.87
Coal	3772.1	27.21
Nuclear energy	611.3	4.41
Hydro-electricity	948.8	6.84
Renewables	561.3	4.05
Total	13864.9	100

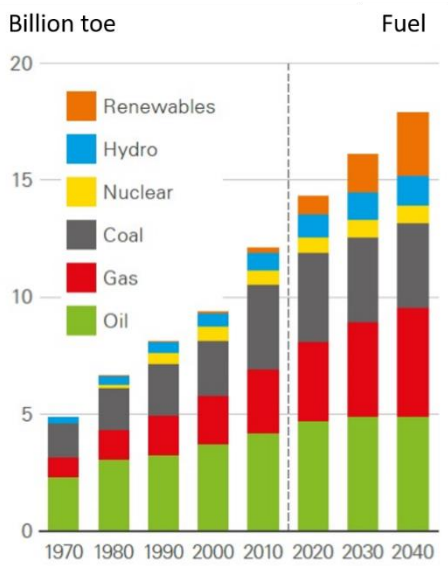

Figure 1-1. Energy outlook predicted by the BP Company [2].

However, although combustion energy is vital to the society, combustion applications inevitably contribute to the emission of pollutants, such as carbon monoxide, sulfur oxides, and nitrogen oxides, which lead to many health, environmental and societal issues [3]. Therefore, one of the primary objectives of combustion research is to improve fuel efficiency and reduce pollutant emissions through improving engine design. Thanks to the rapid growth in computational capabilities and improvement in computing techniques, high-fidelity computational fluid dynamics (CFD), such as large-eddy simulations (LES) and direct numerical simulations (DNS), has been playing a more and more important role in understanding combustion processes and optimizing engine designs over the last few decades [4].

Detailed chemistry has been critical to accurate prediction of complex flame behaviors and limit combustion phenomena, such as ignition, extinction and flame propagation [4,5]. A major challenge of incorporating detailed chemistry in CFD simulations is attributed to the large number of species and reactions as shown in Figure 1-2 [4]. It is seen that combustion of transportation fuels may involve thousands of species and tens of thousands of reactions, and newer mechanisms

tend to be larger because newly measured and/or calculated reaction pathways keep on being added to existing mechanisms. To address this challenge and reduce the computational cost associated with large detailed chemistry, the present study is focused on developing reduced mechanisms and new reduction strategies for engine applications.

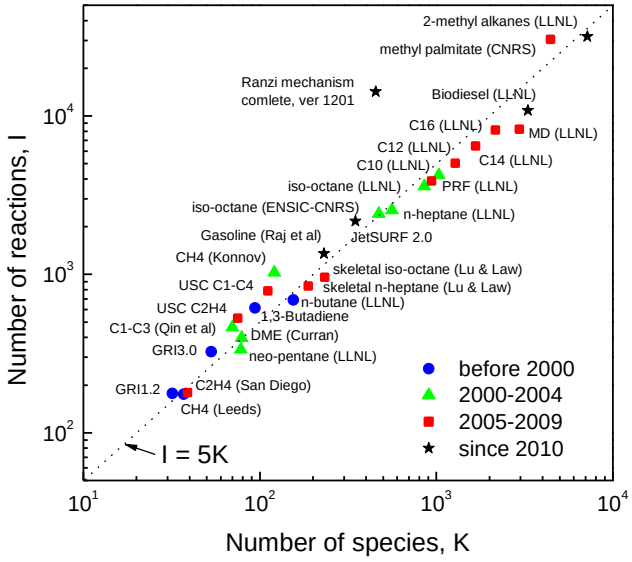

Figure 1-2. Dependence of mechanism size for selected hydrocarbon fuels on molecular sizes and mechanism release dates [4].

1.2. Background

1.2.1. Mechanism Reduction Methods

Various mechanism reduction methods have been developed over the last few decades at two primary levels. The first level is skeletal reduction, which is to identify and retain a subset of species and reactions in the detailed mechanism while still being able to predict selected flame features with reasonable accuracy. Methods for skeletal reduction include, for example, sensitivity

analysis [6], principal component analysis [7], Jacobian analysis [8], optimization [9,10], detailed reduction [11], directed relation graph (DRG) [12–14], DRG with error propagation (DRGEP) [15], path flux analysis (PFA) [16], transport-flux-based DRG [17], multi-element flux analysis [18], betweenness centrality [19], and the combination of sensitivity analysis and graph-based methods, such as DRG aided sensitivity analysis (DRGASA) [20,21] and DRGEP and sensitivity analysis (DRGEPSA) [22]. The second level of reduction is based on timescale analyses that approximate exhausted fast chemical processes with algebraic equations. Quasi-steady-state approximations (QSSA) [23] and partial equilibrium assumptions (PEA) [24] are canonical examples of timescale analyses. In particular, QSSA have been extensively applied and automated for systematic mechanism reduction [25]. Timescale analyses for general systems typically require eigenanalysis to decouple the fast and slow modes, e.g. in the method of intrinsic low-dimensional manifold (ILDM) [26–28]. Computational singular perturbation (CSP) can decouple fast and slow processes in nonlinear problems with a higher order of accuracy [29–32]. Eigenanalysis can be employed to further distinguish between quasi-steady state and partial equilibrium processes in complex kinetic systems [33], and equilibrium-controlled fast species can be approximated by using rate-controlled constrained equilibrium (RCCE) [34–36].

In addition to skeletal reduction and timescale analyses, lumping is another reduction approach that is worth mentioning. Mechanisms of large hydrocarbons typically consist of a large number of isomers, which feature similar thermodynamic and transport properties, therefore the governing equations of the isomers can frequently be grouped if their intragroup mole fractions can be predicted based on the concentration of the entire group [37–40]. The method of isomer lumping can be particularly useful in reducing large hydrocarbon mechanisms, such as gasoline, diesel, and biodiesel fuels [41,42].

1.2.2. Turning Points of Perfectly Stirred Reactors

Ignition and extinction are transitions between burning and non-burning states. There are many practical applications that are relevant to ignition and extinction phenomena, such as engine start-up, flame stabilization, and fire safety applications. Therefore, it is important to include ignition and extinction states in the sample reaction states for mechanism reduction, such that the resulting mechanisms can predict the limit flame behaviors.

Steady-state perfectly stirred reactors (PSR) provide a simple and effective approach to study ignition and extinction limits relevant to continuous flow combustors. The ignition and extinction states of PSR are typically associated with the turning points on the *S*-curves as illustrated in Figure 1-3 [43]. The *S*-curve is a profile of a dependent variable, e.g. temperature or burning rate, as a function of residence time or the Damköhler number, Da, which represents the ratio of characteristic mixing time to a chemical reaction timescale.

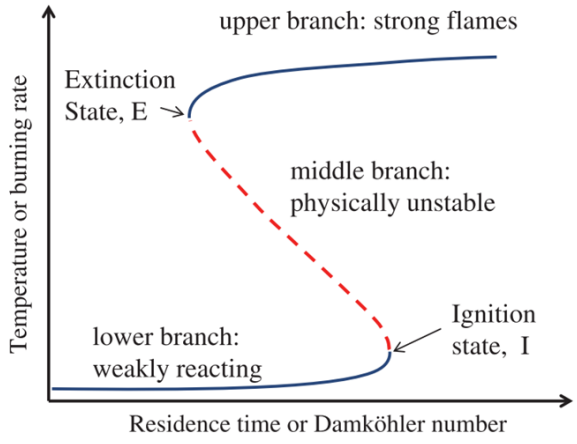

Figure 1-3. A representative *S*-curve with ignition and extinction states [43].

The *S*-curve typically consists of three branches, namely the upper, middle and lower branches, connected by two turning points. The upper and lower branches are physically stable and involve strongly- and weakly-reacting states, respectively. While the middle branch is physically unstable and thus is typically inaccessible in experiments. The upper turning point is commonly regarded as the extinction state of strong flames, as further reducing the residence time quenches the system and the solution jumps to the lower branch. The lower turning point is known as the ignition state as the system jumps to the upper branch with further increased residence time.

Due to the importance of the limit phenomena, numerically obtained ignition and extinction states associated with the turning points on *S*-curves have been routinely compared with experimentally measured limit flame conditions [20,44–48]. Moreover, the extinction residence time is frequently selected as a target parameter in mechanism reduction and validation processes [4,14,20,49,50].

1.2.3. Engine Simulations with Gasoline and Gasoline/Ethanol Surrogates

Transportation powered by combustion engines burning liquid petroleum-based fuels is critical to the modern economy and accounts for about 20% of the total energy consumed [51] and 14% of the emission of global greenhouse gases (GHG) [52]. About 40% of the global transport energy demand is attributed to gasoline spark-ignition (SI) engines commonly used in cars [53]. As such improving SI engine efficiency can significantly reduce the global fuel consumption and pollutant emissions. Knocking is a major issue limiting the fuel efficiency in SI engines, and is caused by end-gas auto-ignition before spark-triggered flame propagation consumes the end gas in the combustion chamber. Knocking can cause rapid pressure fluctuations and can potentially

damage critical engine parts such as the liner and piston. Therefore, developing knock mitigation strategies is critical in improving the performance of SI engines [54].

Multidimensional computational fluid dynamics (CFD) can serve as a valuable tool in understanding the interaction between fuel properties and engine operating conditions. However, gasoline fuels derived from petroleum comprise thousands of individual hydrocarbons including alkanes, olefins, cycloalkanes, and aromatics, rendering the determination of the exact composition impractical [55]. Such that, simple surrogate fuels, consisting of a small number of compounds, are often adopted to approximate the physical and chemical properties of real gasoline fuels. For example, commonly used gasoline surrogates are the primary reference fuels (PRF), which are binary mixtures of n-heptane and iso-octane. The anti-knocking behavior of gasoline is characterized by research and motor octane numbers (RON, MON), and a higher octane number indicates a higher knock resistance [56]. RON and MON are evaluated in a standard "Cooperative Fuels Research" (CFR) engine under two differing engine conditions respectively [57]. Since by definition, the PRF surrogates have zero sensitivity (S = RON-MON), it fails to emulate the ignition behavior of commercial gasoline fuels with high non-paraffinic content due to the fact that high non-paraffinic gasoline fuels have a relatively high octane sensitivity. Therefore, to match both RON and MON, toluene primary reference fuel (TPRF) comprised of iso-octane, n-heptane, and toluene have been proposed as a more suitable gasoline surrogate recently [58,59]. The composition of a TPRF to match the target RON and MON can be determined by a simple correlation for a wide range of octane numbers [60]. Meanwhile, alcohols have been suggested as an engine fuel almost since the automobile was invented [61] and among the various alcohols, ethanol is known as the most suited fuel for SI engines and has already been widely used in the

United States as an additive to gasoline since it has high ON and can be produced from renewable energy sources such as agricultural feedstock [62,63].

Therefore, accurate kinetic models for TPRF with ethanol are needed to predict knocking in engine simulations. While the detailed mechanism for gasoline surrogates developed by the Lawrence Livermore National Laboratory (LLNL) is comprised of 1389 species and 5935 elementary reactions [64], an accurate reduction and comprehensive validation process, involving low-temperature chemistry, is required to generate a suitable sized mechanism for CFD.

1.2.4. Bio-blend-stock with the Potential to Optimize Engine Performance

To more appropriately quantify the antiknock quality of fuels under different in-cylinder conditions, octane index, OI=RON-K*S, is proposed [65,66], where K is determined by the pressure-temperature history of the unburnt mixture in the combustion chamber and K equals zero and unit at the RON and MON conditions respectively by definition. It is seen that as K becomes negative, which is typically true for modern downsized boosted SI engines, fuel with a high RON and S can be more knock resistance [67–71]. Such that, investigating potential bio-blend-stock that can be blended with gasoline to increase both RON and S is one focus of the U.S. Department of Energy's Co-Optimization of Fuels & Engines (Co-Optima) initiative, which aims to maximize energy efficiency and minimize environmental impact.

In Co-Optima, a three-stage tiered process is used to comprehensively assess the blendstocks. Tier 1 focused on the properties of the individual bio-blend-stocks and bio-blend-stocks that meet the requirement of melting and boiling points, solubility, corrosivity, toxicity, handling safety and biodegradability were identified [72]. Tier 2 focused on the properties of mixtures of the bio-blend-stocks and various gasoline. In Tier 2, a combination of experimental

measurements and computational approaches based on machine learning and group contribution were used and gasoline/bio-blend-stocks blends that meet the requirement of octane number, vaporization heat, and heating value were identified. After Tier 1 and 2 assessments, eight representative bio-blend-stocks shown in Figure 1-4 were identified and are currently undergoing the Tier 3 assessment which focuses on evaluating their ability in improving engine efficiency [73]. In the Tier 3 evaluations, engine simulations are widely adopted to assess the engine performance of different gasoline/bio-blend-stocks blends and efficient mechanism reduction methods are required to incorporate the extreme large-sized detailed mechanism consisting of 2878 species developed by LLNL [74] in CFD simulations.

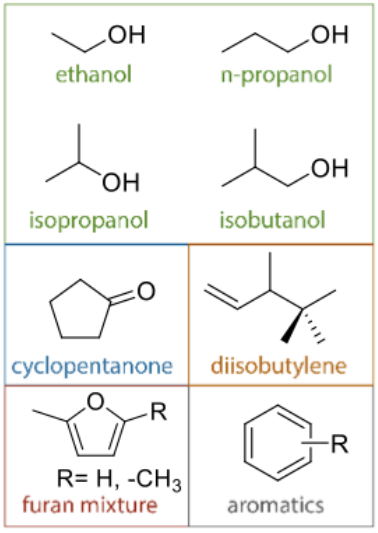

Figure 1-4. Eight representative bio-blend-stocks identified for the Tier 3 evaluation [73].

1.3. Objectives and Structure of the Dissertation

This dissertation aims to develop improved reduction strategies and generate accurate reduced mechanisms amenable for 3-D SI engine simulations. In Chapter 2, a linearized error propagation (LEP) method for skeletal mechanism reduction is proposed. The basic concepts and

formulations of DRG and DRGEP are first reviewed. The error estimation in LEP is then compared with that in the DRG and DRGEP methods for both local and global reduction cases. Lastly, global skeletal mechanisms for ethylene and n-heptane are obtained by using LEP and validated against the detailed mechanisms.

In Chapter 3, a direct method for calculating the turning points of PSR is proposed and compared with the commonly used arch-length continuation method. Sensitivity analyses of the ignition and extinction turning points in PSR are performed by the newly developed analytical method. Important reactions to the ignition and extinction turning points of PSR are identified and discussed.

In Chapter 4, reduced and skeletal mechanisms for SI engine combustion of gasoline and gasoline/ethanol surrogates were developed from the detailed LLNL mechanism by using DRG, sensitivity analysis, isomer lumping and the linearized quasi-steady-state approximations (LQSSA). The reduction was based on reaction states sampled under a wide range of temperature, pressure and equivalence ratio, including the negative temperature coefficient (NTC) region. The reduced and skeletal mechanisms were extensively validated against the detailed mechanism and available experimental data for ignition delay time and flame speed, which are of great importance to SI engine simulations, over a wide range of surrogate compositions and operating conditions. The skeletal mechanism was further employed to predict the critical compression ratio in a CFR engine simulation, which agrees well with experimental data.

Chapter 5 presents three highly reduced skeletal mechanisms for TPRF/di-isobutylene, TPRF/anisole, and TPRF/iso-butanol, developed by using DRG, LEP and sensitivity analysis, and validated against the detailed mechanism for ignition delay time, PSR extinction residence time and flame speed. To speed up the iterative ignition delay time evaluations in the sensitivity analysis,

the ODE solver was improved by using analytical Jacobian and sparse matrix techniques, and the computational time was significantly reduced.

Chapter 6 presents the major conclusions obtained through the present study and discusses possible future extensions.

1.4. List of Publications

1. **Yunchao Wu**, Tianfeng Lu, "A direct method for calculating the turning points of perfectly stirred reactors", under review
2. **Yunchao Wu**, Yufeng Liu, Tianfeng Lu, "A linearized error propagation method for skeletal mechanism reduction", under review
3. Tai Jin, **Yunchao Wu**, Xujiang Wang, Kai H. Luo, Tianfeng Lu, Kun Luo, Jianren Fan, "Ignition dynamics of DME/methane-air reactive mixing layer under Reactivity Controlled Compression Ignition conditions: Effects of cool flames", Applied Energy, 249 (2019) 343-354.
4. Pinaki Pal, Christopher P Kolodziej, Seungmok Choi, Sibendu Som, Alberto Broatch, Josep Gomez-Soriano, **Yunchao Wu**, Tianfeng Lu, Yee Chee See, "Development of a Virtual CFR Engine Model for Knocking Combustion Analysis", SAE Int. J. Engines, 11 (2018) 1069-1082.
5. Pinaki Pal, **Yunchao Wu**, Tianfeng Lu, Sibendu Som, Yee Chee See, Alexandra Le Moine, "Multidimensional Numerical Simulations of Knocking Combustion in a Cooperative Fuel Research Engine", Journal of Energy Resources Technology, 140 (2018) 102205.
6. Sibo Wang, **Yunchao Wu**, Ran Miao, Mingwan Zhang, Xingxu Lu, Bo Zhang, Alexander Kinstler,a Zhuyin Ren, Yanbing Guo, Tianfeng Lu, Steven L. Suibc, Pu-Xian Gao,

"Scalable continuous flow synthesis of ZnO nanorod arrays in 3-D ceramic honeycomb substrates for low-temperature desulfurization", CrystEngComm, 19 (2017) 5128-5136.

Chapter 2. A Linearized Error Propagation Method for Skeletal Mechanism Reduction

2.1. Introduction

Skeletal reduction is to obtain a subset of species and reactions in a detailed chemical kinetic mechanism that can reasonably predict selected flame features with a reduced computational cost. Methods of skeletal reduction are extensively reviewed in Section 1.2.1.

The key to skeletal reduction is to eliminate species and/or reactions without incurring errors larger than a tolerable threshold value. Due to the nonlinearity in detailed chemical kinetics, probably the only approach to obtain the exact errors induced by the elimination of species is the global sensitivity analysis (GSA), which directly compares the solutions before and after elimination to measure the actual reduction errors. However, brute-force GSA involves a large number of possible sequences for species eliminations, such that an exhaustive search for the smallest skeletal mechanism using GSA is typically computationally infeasible. To avoid the expensive GSA, reduction algorithms with *a priori* error control, that is to use a pre-specified threshold value to effectively limit the worst-case reduction error, is required. Due to the strong nonlinearity of chemical kinetics, systematic *a priori* error control can only be achieved for small reduction errors as the error propagation can be linearized. For instance, in the literature, DRG has been able to effectively control the worst-case errors for all the species in skeletal mechanisms for an error threshold of O(0.1), by assuming that errors may not decay along the graph-search paths [75]. However, if only the errors in the target species are of interest, the no-decay assumption in DRG may overestimate the reduction errors in the target species in certain cases, such that the resulting skeletal mechanisms may be further reduced, for example, by using GSA based methods [20]. In contrast, DRGEP aims at controlling the errors only in selected target species and assumes geometric error-decay along graph-search paths. The geometric error-decay model in DRGEP is

nevertheless rather aggressive and may under-estimate reduction errors in species far downstream of the graph-search paths, resulting in unsafe species eliminations [76]. As such, accurate error propagation models are needed to minimize the possibility of unsafe species eliminations in graph-based skeletal reduction methods.

In the present study, a linearized error propagation (LEP) method is developed based on Jacobian analysis to accurately predict the propagation of small reduction errors. First, LEP is formulated based on steady-state PSR, which involves reaction states relevant to both ignition and extinction problems. LEP is then compared with DRG and DRGEP for reduction of ethylene mechanism in term of reduction error prediction. Lastly global skeletal mechanisms are obtained with LEP for ethylene and n-heptane based on reaction states sampled from PSR. The skeletal mechanisms are further validated in auto-ignition and 1-D laminar premixed flames to demonstrate the feasibility of using only PSR for the reaction state sampling.

2.2. Methodology

2.2.1. Reaction State Sampling

In skeletal mechanism reduction, an unimportant reaction can be slow due to a small reaction rate coefficients, which is typically in the Arrhenius form and is temperature dependent, and/or low reactant concentrations. Therefore, skeletal reduction is sensitive to the selection of the species composition space, and typically must be performed based on reaction states sampled from selected elementary reactors or flames such as auto-ignition, PSR, and 1-D laminar premixed or non-premixed flames. Multi-dimensional simulations using detailed chemistry are typically computationally expensive and are rarely employed for the reaction state sampling. To extend the reduced mechanisms obtained from elementary reactors to the more complex multi-dimensional flames, the solutions from the selected elementary reactors must be relevant to the reaction states

involved in the complex flames. Therefore, the selection of elementary reactors for reaction state sampling is a critical step in mechanism reduction.

Previous studies show that reduced mechanisms based on reaction states sampled from auto-ignition and PSR over an adequate range of temperatures, pressures, and equivalence ratios can typically be extended to more complex flames without incurring significantly larger errors [4]. This is because most practical combustors are built based on two major reaction modes. The first depends on auto-ignition, which is rate-controlled by the radical explosion process. An example of this type of combustor is the compression ignition engines, where a hot flame does not exist initially such that radicals can only build up through the relatively slow chain branching reactions. The thermal runaway subsequent to radical explosion is typically significantly faster, such that the ignition delay time for auto-ignition is typically dominated by the radical explosion stage. The second type of combustion mode is relevant to PSR, in which reactants are quickly mixed into hot products with high radical concentrations. The slow radical explosion stage is therefore bypassed, and the overall combustion process can be significantly faster. This type of combustion is typical for flames in recirculation zones, which can be induced by a bluff body or cavity, the reaction zone of non-premixed flames, propagation of premixed flames, and flame extinction problems.

In the present study, only reaction states sampled from PSR will be employed for the reduction considering that the *S*-curve of PSR including both the ignition states, which are near the lower turning point and are typically rate-controlled by radical pool build-up, in addition to the extinction states near the upper turning point. The reaction states from auto-ignition can, therefore, be replaced by those from the lower portion of the PSR *S*-curve. Note that the entire PSR *S*-curves can be obtained by the arc-length continuation method [77,78] or simply switching between temperature and residence time as the dependent variable when marching across the turning points.

2.2.2. Formulation LEP Based on PSR Solutions

The key component of the LEP method is to accurately predict errors in selected target species induced by the elimination of other species. In the following, LEP will be formulated based on solutions from steady-state PSR, the governing equations for which can be expressed as

$$\begin{gathered} \omega_i + s_i = 0, i = 1, \dots, n_s + 1 \\ \omega_i = \frac{\dot{m}_i}{\rho}, s_i = \frac{Y_i^0 - Y_i}{\tau}, i = 1, \dots, n_s \\ \omega_{n_s+1} = -\frac{\sum_{i=1,K}(\dot{m}_i h_i)}{\rho c_p}, s_{n_s+1} = \frac{\sum_{i=1,K}\left(Y_i^0 (h_i^0 - h_i)\right)}{\tau c_p} \end{gathered} \tag{2-1}$$

where ω and s denote the reaction and mixing source terms, respectively, $\dot{m}$ is species mass production rate, ρ is density, Y is species mass fraction, h is species-specific enthalpy, which is a function of temperature T, c_p is the mixture-averaged constant-pressure heat capacity, and τ is the residence time. Subscript i indicates the i^{th} species, n_s is the total number of species. Superscript 0 indicates the inlet condition. Note that the above n_s+1 equations can be used to solve for all the species mass fractions together with T or τ, whichever selected to be a dependent variable with the other being a specified parameter.

When a species is eliminated in skeletal reduction, all the reactions involving this species are eliminated and excluded from the evaluation of $\dot{m}$. The remaining equations in (2-1) change from

$$\boldsymbol{\omega}^{\boldsymbol{r}}(\boldsymbol{y}^*) + \boldsymbol{\omega}^{\boldsymbol{e}}(\boldsymbol{y}^*, Y_e^*) + \boldsymbol{s}(\boldsymbol{y}^*) = 0 \tag{2-2}$$

to

$$\boldsymbol{\omega}^{\boldsymbol{r}}(\boldsymbol{y}) + \boldsymbol{s}(\boldsymbol{y}) = 0 \tag{2-3}$$

where $\boldsymbol{\omega^r}$ and $\boldsymbol{\omega^e}$ indicate reaction source terms related to the remaining reactions and eliminated reactions, respectively, and $\boldsymbol{s}$ is the mixing term. $\boldsymbol{y}$ is the vector of the remaining species mass fractions and temperature. The superscript * indicates the original solution without the species elimination and Y_e^* is the mass fraction of the eliminated species. Comparing Eqs. (2-2) and (2-3), the errors induced to the remaining variables, $\delta\boldsymbol{y} = \boldsymbol{y} - \boldsymbol{y}^*$, can be linearly approximated as

$$\delta\boldsymbol{y} \approx (\boldsymbol{J_s} + \boldsymbol{J_\omega})^{-1}\boldsymbol{\omega^e},$$
$$\boldsymbol{J_\omega} = \frac{\partial\boldsymbol{\omega^r}}{\partial\boldsymbol{y}^*}, \qquad \boldsymbol{J_s} = \frac{\partial\boldsymbol{s}}{\partial\boldsymbol{y}^*} \tag{2-4}$$

where $\boldsymbol{J_\omega}$ and $\boldsymbol{J_s}$ are the Jacobian matrices of $\boldsymbol{\omega^r}$ and $\boldsymbol{s}$, respectively. The Jacobian matrices in the present study are evaluated analytically to ensure a high accuracy [79]. Note the right-hand side of Eq. (2-4) is assessed based on the original solution $\boldsymbol{y}^*$ and Y_e^*, therefore the errors are estimated without solving the new governing equations. Based on Eq. (2-4), the relative error of species *A* induced by the elimination of species *B* can be approximated as

$$R_{AB}^{\mathrm{LEP}} = \frac{|\delta Y_A|}{Y_A + |\delta Y_A|} \tag{2-5}$$

The importance of species *B* to species *A* can thereby be determined by comparing the relative error with a small threshold value, say 0.1. Note that the relative error in temperature or residence time, whichever selected to be a dependent variable, can be defined similarly to that for a species.

2.2.3. Review of DRG and DRGEP

DRG and DRGEP are first reviewed to make a comparison with LEP. The key step in DRG is to quantify the pair-wise relative error directly induced to species *A* by the elimination of a species *B* as

$$r_{AB}^{\mathrm{DRG}} = \frac{\max_i \left| \nu_{i,A} \omega_i \delta_B^i \right|}{\max_i \left| \nu_{i,A} \omega_i \right|}$$

$$\delta_B^i = \begin{cases} 1, & \text{if the } i^{\text{th}} \text{ reaction involves species } B, \\ 0, & \text{otherwise,} \end{cases} \tag{2-6}$$

where the subscripts i, A, and B indicate the i^{th} elementary reaction and species A and B, respectively. ν is the stoichiometric coefficient, and ω is the net reaction rate. A large r_{AB}^{DRG} indicates that B is important for the reaction rate of species A and thus should be retained if A is retained. Note that Eq. (2-6) is a definition that works better for mechanisms with a large number of isomers [14] than the original definition in Ref. [12]. In addition to the directly induced error, eliminating B may induce errors to A indirectly by affecting other species that directly or indirectly affect A.

DRG assumes that the error does not decay along the graph-search paths, and the indirect error for a specific search-path p from A to B is controlled by the smallest r-value along the path, i.e.

$$r_{AB,p}^{\mathrm{DRG}} = \min_i r_{S_i S_{i+1}}^{\mathrm{DRG}}, S_1 = A, S_n = B. \tag{2-7}$$

The overall relative error in species A induced by the elimination of species B can then be estimated as the maximum error among all the paths from A to B:

$$R_{AB}^{\mathrm{DRG}} = \max_p r_{AB,p}^{\mathrm{DRG}}. \tag{2-8}$$

If a species A is to be retained in a skeletal mechanism, every species B with $R_{AB}^{\mathrm{DRG}} > \varepsilon$, where ε is a threshold error tolerance, should be retained as well. Calculation of the R-values in Eq. (2-8) was achieved in DRG through a recursive graph search starting from species A, which can be the H radical or any other species of interest.

In contrast, DRGEP assumes geometric error damping along a graph-search path, and the path-specific error in species *A* induced by the elimination of species *B* is defined as

$$r_{AB,p}^{\mathrm{DRGEP}} = \prod_{i=1}^{n-1} r_{S_i S_{i+1}}^{\mathrm{DRGEP}}, S_1 = A, S_n = B, \tag{2-9}$$

with the direct error defined as

$$r_{AB}^{\mathrm{DRGEP}} = \frac{\left|\sum_{i=1,n_R} \nu_{i,A}\omega_i \delta_B^i\right|}{max(P_A, C_A)}$$
$$P_A = \sum_{i=1}^{n_R} max\left(0, \nu_{i,A}\omega_i\right), \; C_A = \sum_{i=1}^{n_R} max\left(0, -\nu_{i,A}\omega_i\right) \tag{2-10}$$

where n_R is the total number of reactions. P_A and C_A are the production and consumption rates of species *A*, respectively. Note that the definition in Eq. (2-10) ensures that $r_{S_i S_{i+1}}^{\mathrm{DRGEP}} \leq 1$. Similar to Eq. (2-8), the overall reduction error in species *A* induced by the elimination of species *B* in DRGEP is estimated as

$$R_{AB}^{\mathrm{DRGEP}} = \max_p r_{AB,p}^{\mathrm{DRGEP}}. \tag{2-11}$$

2.3. Results and Discussion

2.3.1. Comparison of Reduction Errors

LEP is first compared with DRG and DRGEP in error estimation based on PSR solutions for stoichiometric ethylene/air under inlet temperature of 1000 K and pressure of 0.5-10 atm. The USC-Mech II [80] is used as the detailed mechanism and H radical is selected as the target species in the following comparison since H is an essential radical for hydrocarbon fuels and has been used as the starting species in DRG [9, 24, 26].

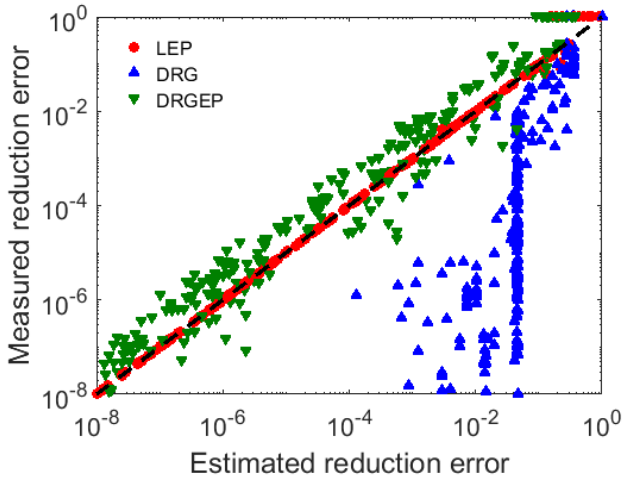

Figure 2-1. Measured vs. estimated reduction errors for the target species, H, induced by single-species eliminations, at the extinction states for PSR of stoichiometric ethylene/air under inlet temperature of 1000 K and pressure of 0.5-10 atm.

Single-species eliminations are performed on the extinction states of the *S*-curves, and the error in H concentration induced by a species elimination is measured by comparing the PSR solutions at given temperatures with and without the species elimination. Meanwhile, the reduction errors induced to H are estimated by LEP, DRG, and DRGEP respectively based on Eqs. (2-3) to (2-10). Figure 2-1 shows the measured vs. estimated errors with the dashed trend line showing the ideal scenario. It's seen that the errors estimated by using LEP is mostly identical to the measured values for small errors, say less than about 0.1, while discrepancies are observed for larger errors as the linear approximation in Eq. (2-3) starts to fail. In contrast, the measured errors are almost always smaller than the estimated errors for DRG, as the data points scatter mostly below the 1:1 trend line, indicating that the species elimination in DRG is safe but may result in under-reduction if only the target species is of interest. In DRGEP, the data points scatter on both sides of the 1:1 trend line, and thus the species elimination may result in errors larger than the specified threshold

values. In the literature, threshold values in the order of 10^{-2} are typically used in DRGEP-based reduction, while threshold values in the order of 10^{-1} are typically used for DRG-based reduction.

Skeletal mechanisms are then derived locally by eliminating all the species with an estimated error smaller than the specified threshold value for the extinction states of PSR in the same parameter range as that of Figure 2-1. It is noted that due to the nonlinearity of chemical kinetics, the error induced by the elimination of a group of species is typically not equal to the summation of the errors induced by eliminating each individual species. Figure 2-2a shows the measured worst-case error in the target species vs. the user-specified threshold value. It is seen that the measured errors for the skeletal mechanisms obtained by using LEP are no longer identical to the threshold value due to the error accumulation and/or cancellation effect in the multi-species elimination process. However, the errors by LEP are overall significantly closer to the ideal 1:1 trend line than those of DRG and DRGEP, showing that LEP can estimate the errors in the target species more accurately than the other two methods.

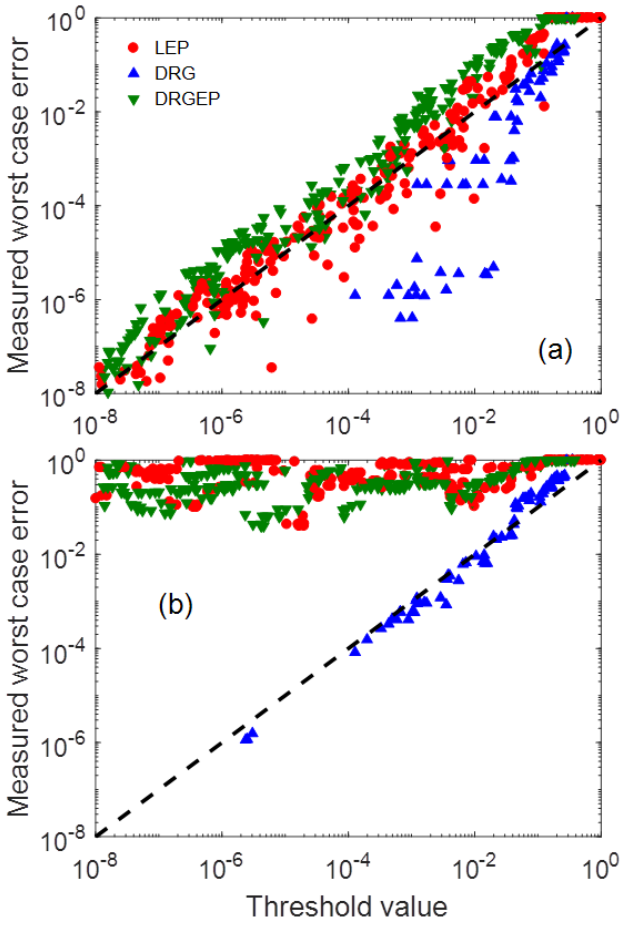

Figure 2-2. Worst-case reduction error in (a) the target species only, and (b) all the retained species, as a function of the user-specified threshold value in LEP, DRG, and DRGEP, at the extinction turning point for PSR of stoichiometric ethylene–air under inlet temperature of 1000 K and pressure of 0.5 to 10 atm.

Figure 2-2b further shows the worst-case errors among all the retained species in the skeletal mechanisms vs. the user-specified threshold value. It is seen that DRG accurately controls the worst-case error in such cases, while LEP and DRGEP cannot effectively control the error with the user-specified threshold value. This unique feature of DRG in controlling the worst-case errors among all the retained species renders it suitable for reduction tasks where post-reduction

validations are not feasible, e.g. for on-the-fly reduction in multi-dimensional flow simulations. In contrast, LEP and DRGEP, as well any other method that cannot effectively limit the worst-case errors may result in unsafe species elimination, and thus the selection of a working threshold value should be determined iteratively by using post-reduction validation, which is typically computationally demanding.

2.3.2. Error Control for Group-eliminations

To more accurately estimate the error induced by the elimination of a group of species, $\boldsymbol{G}$, the LEP model is slightly modified as

$$\boldsymbol{\delta y} \approx (\boldsymbol{J}_s^{\boldsymbol{G}} + \boldsymbol{J}_\omega^{\boldsymbol{G}})^{-1} \cdot \boldsymbol{\omega}^{\boldsymbol{G}} \tag{2-12}$$

where $\boldsymbol{\omega}^{\boldsymbol{G}}$ are the reaction source term attributed to reactions involving any species in $\boldsymbol{G}$. $\boldsymbol{J}_s^{\boldsymbol{G}}$ and $\boldsymbol{J}_\omega^{\boldsymbol{G}}$ are Jacobian matrixes related to the mixing and reaction terms, respectively, in the remaining governing equations. A new reduction strategy similar to DRGASA [20] is then proposed for LEP. Specifically, species are eliminated one at a time in the ascending order of the estimated error by single-species elimination, until the reduction error estimated with Eq. (2-12) exceeds a user-specified threshold value. The above procedure is then repeated until no species can be further eliminated, such that the largest extent of reduction is achieved.

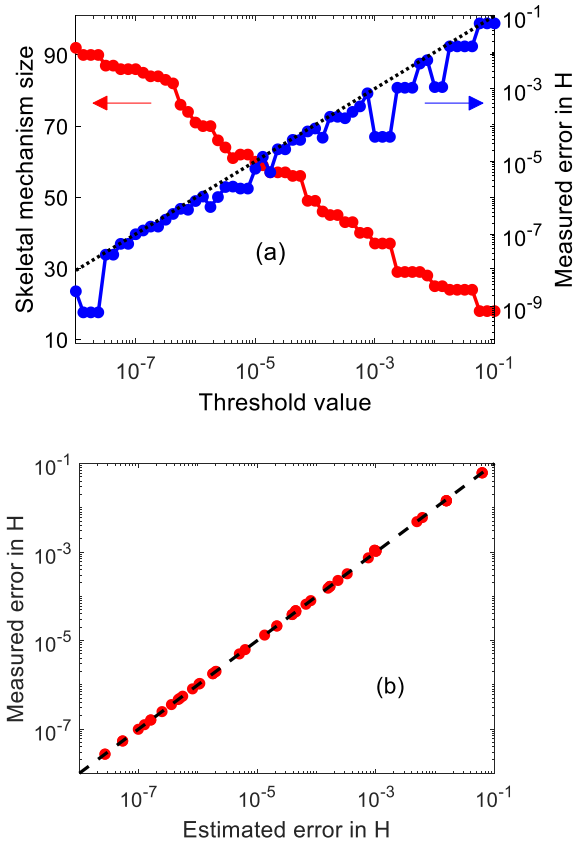

Figure 2-3. (a) Number of species in the skeletal mechanism and measured errors in H concentration as functions of the user-specified threshold value. (b) Measured vs. estimated reduction errors in H radical for the skeletal mechanisms obtained by LEP at the extinction turning point for PSR with stoichiometric ethylene–air under atmospheric pressure and inlet temperature of 1000 K.

LEP with the new reduction strategy is applied at the extinction turning point for PSR of stoichiometric ethylene/air under atmospheric pressure and inlet temperature of 1000 K. Different skeletal mechanisms are obtained for threshold values ranging from 10^{-8} to 0.1, with H radical being the target species. Figure 2-3a shows the number of species in the skeletal mechanism and measured errors in H radical as functions of the user-specified threshold value. It is seen that the

skeletal mechanism size overall decreases as the threshold value increases and the measured errors in H radical scatter slightly below the 1:1 trend line, indicating that the reduction errors of the skeletal mechanisms obtained from LEP are rather accurately controlled by the threshold value. Figure 2-3b further shows that the estimated errors in H radical are nearly identical to the measured errors, which is the reason that LEP can effectively control the reduction error for the elimination of a group of species. Therefore, LEP based reduction can be significantly more computationally efficient than DRGASA as the time-consuming sensitivity analysis is not involved in LEP.

2.3.3. Obtaining Global Skeletal Mechanisms

While LEP is formulated for local reduction based on an individual reaction state, global skeletal mechanisms can be obtained by performing reduction based on multiple reaction states sampled from a wide range of operating conditions. In this section, the error control in global skeletal mechanisms obtained with LEP is investigated. The sample space is constructed by the stoichiometric ethylene–air PSR solutions ranging from 1600 K to 2400 K under atmospheric pressure and inlet temperature of 1000 K. The sample space, which is a part of the *S*-curve including the extinction point, is illustrated by the solid line in Figure 2-4a. A 28-species skeletal mechanism henceforth referred to as sk28, is generated using LEP with a threshold value of 0.1 and H radical as target species. To measure the reduction errors, species concentrations and residence time in PSR are solved for specified temperatures using sk28 as shown in Figure 2-4a. It is seen that the *S*-curve from sk28 is almost identical to that from the detailed mechanism. Figure 2-4b further shows the mass fraction of H radical calculated with the detailed mechanism and sk28, respectively. It is seen that the error in H in sk28 is effectively controlled by the threshold value of 0.1.

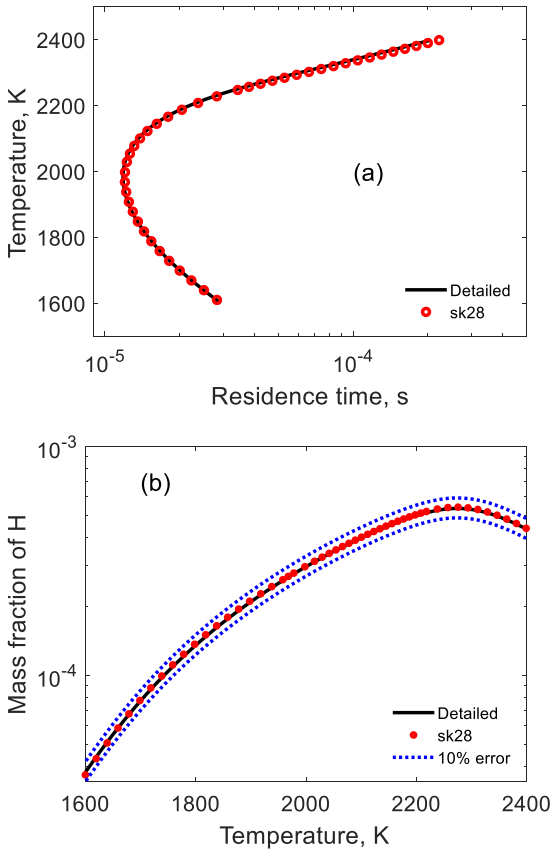

Figure 2-4. (a) The *S*-curve, and (b) H radical mass fraction, of PSR of stoichiometric ethylene−air under atmospheric pressure and inlet temperature of 1000 K, calculated with the detailed mechanism (solid lines) and sk28 (symbols), respectively. The dashed lines in (b) indicate ±10% errors, respectively.

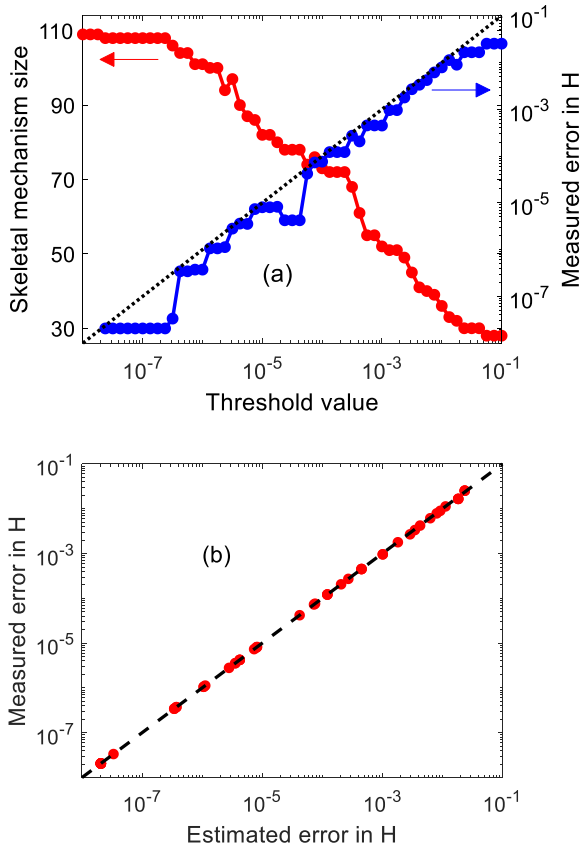

Figure 2-5. (a) Number of species in the global skeletal mechanism and measured worst-case errors in H radical as functions of the user-specified threshold value. (b) Measured vs. estimated worst-case reduction error in H radical in the global skeletal mechanisms obtained with LEP.

Global skeletal mechanisms are then obtained by using different threshold values ranging from 10^{-8} to 0.1 based on the reaction states sampled along the PSR *S*-curve. The mechanism size (number of species) and measured worst-case error in H radical are shown in Figure 2-5a, and it is seen that the worst-case reduction errors in H radical are bounded by the threshold values, which is similar to the local reduction shown in Figure 2-3. Figure 2-5b further shows that the measured worst-case errors in H are mostly identical to the estimated errors, indicating that LEP can

accurately estimate the worst-case error in the target species and thus can effectively control the reduction error by using a user-specified error tolerance.

2.3.4. Global Skeletal Mechanisms for Ethylene and n-Heptane

Global skeletal mechanisms are then developed with LEP for two different fuels, namely ethylene and n-heptane. The skeletal mechanism for ethylene/air is obtained from the detailed USC-Mech II based on reaction states sampled from PSR with an inlet temperature of 1000 K over the parameter space of pressure from 0.5 to 10 atm, equivalence ratio from 0.5 to 1.5, with the temperature range of from 1000 K to 100 K below the adiabatic flame temperature such that the sample space covers both the ignition and the extinction turning points. A threshold value of 0.1 is specified with H radical being the target species and then a skeletal mechanism with 35 species and 228 reactions is obtained.

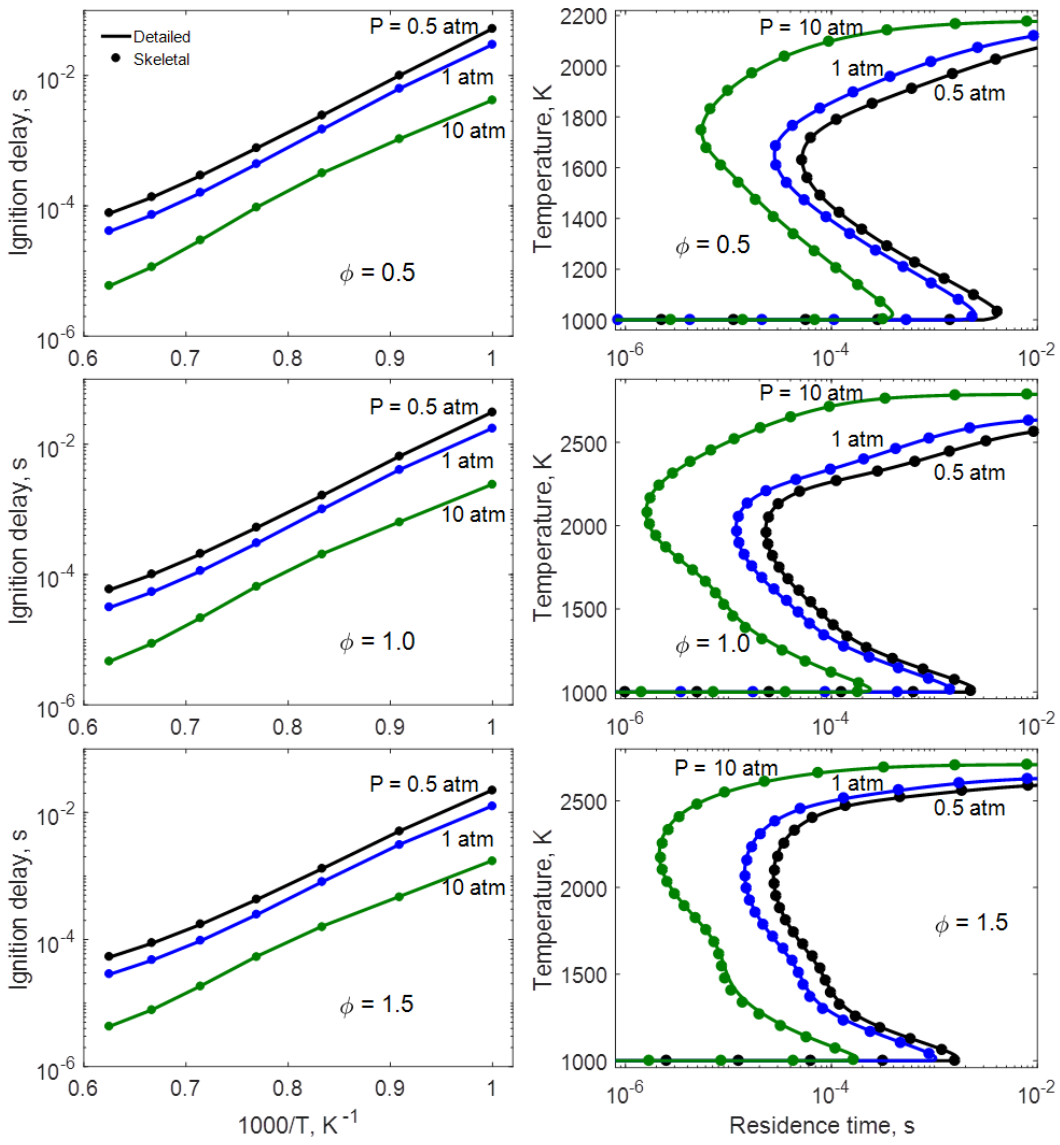

Figure 2-6. Ignition delay time of constant-pressure auto-ignition as a function of initial temperature (left panels) and PSR *S*-curves at inlet temperature of 1000 K (right panels) for ethylene–air under different pressures and equivalence ratios, calculated with the detailed and skeletal mechanisms, respectively.

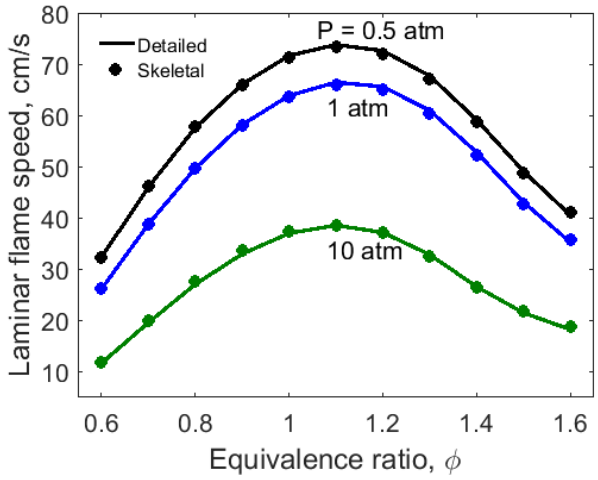

Figure 2-7. Laminar flame speed as a function of equivalence ratio for ethylene/air under different pressures and inlet temperature of 300 K, calculated with the detailed and skeletal mechanism, respectively.

Figure 2-6 shows the validation of the skeletal mechanism for auto-ignition and PSR over the same range of pressures and equivalence ratios to that for the reduction. Figure 2-7 further shows the validation of laminar flame speed for different equivalence ratios and pressures. It is seen that the skeletal mechanism derived from PSR alone is not only valid for PSR but also can be extended to auto-ignition and premixed flames with high accuracy. This is because the reaction states sampled from PSR involve both the extinction state (the upper turning point), where the radical pool is present, and the ignition state (the lower turning point), where the radical pool is building up through the relatively slow chain branching processes. Therefore reaction states sampled from the entire PSR curve can cover both the fast flame chemistry and the slow ignition chemistry, and the resulting skeletal mechanisms feature similar extendibility as those based on the sampling from both PSR and auto-ignition in previous studies.

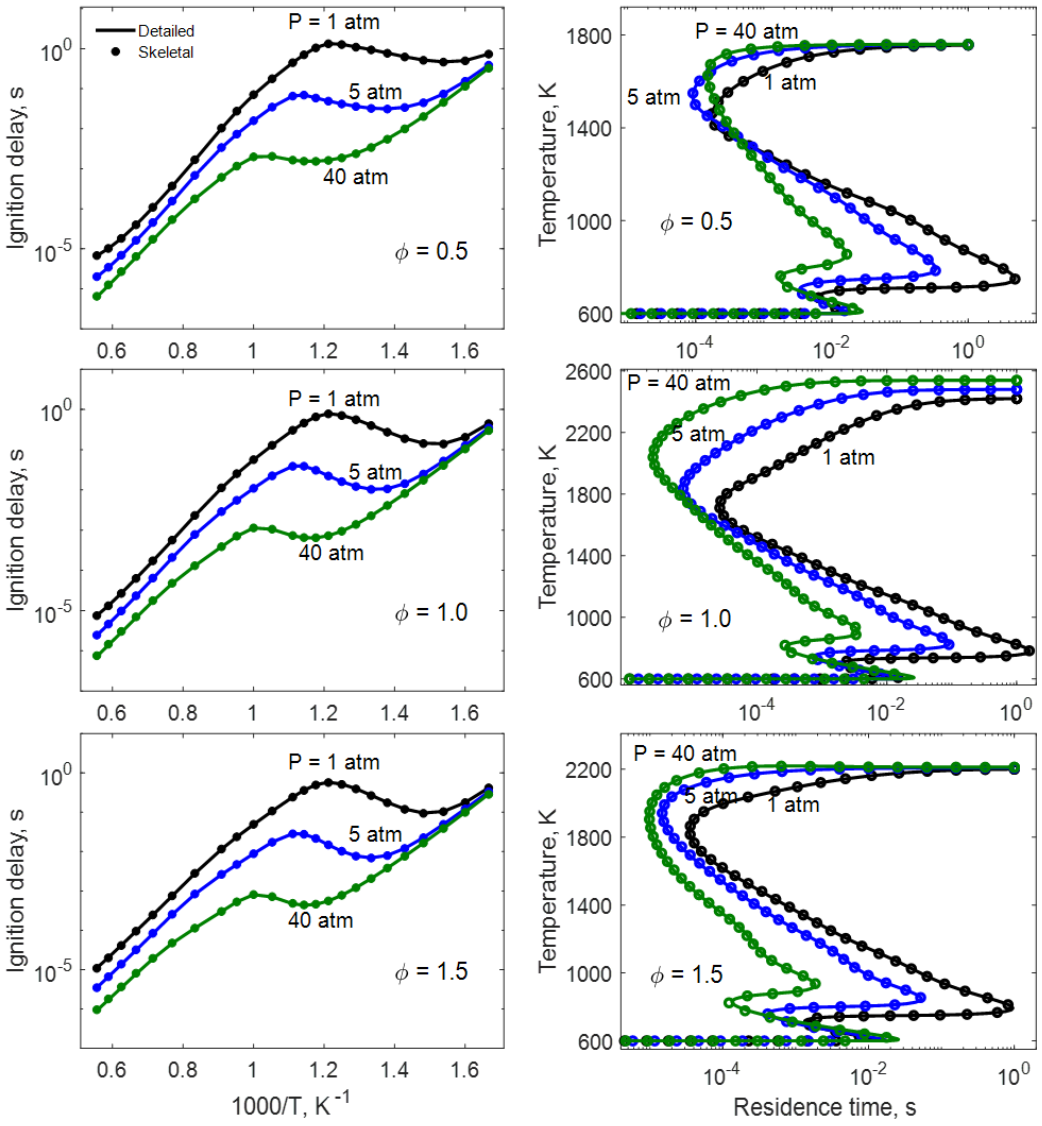

Figure 2-8. Ignition delay time of constant-pressure auto-ignition as a function of initial temperature (left panels), and PSR *S*-curves at inlet temperature of 600 K (right panels), for *n*-heptane/air under different pressures and equivalence ratios, calculated with the detailed and skeletal mechanisms, respectively.

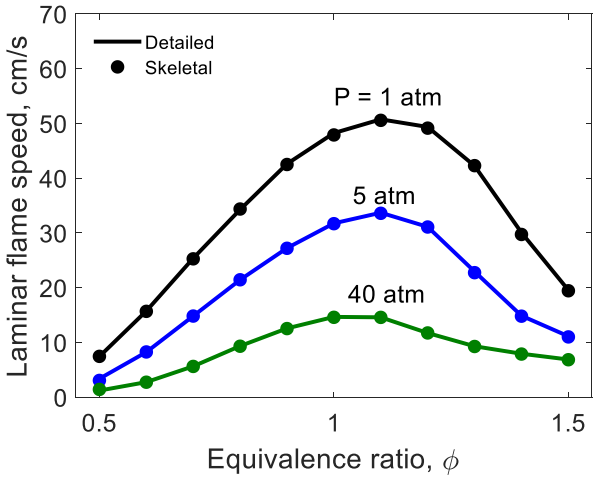

Figure 2-9. Laminar flame speed as a function of equivalence ratio for *n*-heptane/air under different pressures and inlet temperature of 300 K, calculated with the detailed and skeletal mechanisms, respectively.

To further test the new reduction method with more complex chemistry, a skeletal mechanism for n-heptane/air is developed from a 188-species skeletal mechanism previously developed by using DRG [13]. The reduction is based on reaction states sampled from PSR with inlet temperature of 600 K under pressure from 1 to 40 atm, equivalence ratio from 0.5 to 1.5, and temperature range from 600 K to 100 K below the adiabatic flame temperature, such that the negative temperature coefficient (NTC) behaviors of the n-heptane chemistry are included in the sample. Note that the pressure and equivalence ratio ranges are exactly the same as those used to develop the 188-species skeletal mechanism using DRG. A skeletal mechanism with 146 species and 631 reactions are then obtained with a user-specified threshold value of 0.1 and H radical being the target species.

Figure 2-8 and Figure 2-9 show the validation of the skeletal mechanism for auto-ignition, PSR and laminar flame speed over the same pressure and equivalence ratio range for the reduction.

It is seen that the skeletal mechanism accurately predicts all these flames as did for the ethylene case. Figure 2-9 further shows that the NTC behaviors are also precisely captured by the skeletal mechanism.

2.4. Conclusion

A linearized error propagation (LEP) method is developed based on Jacobian analysis and reaction state sampling from PSR to achieve effective error control on selected target species in skeletal mechanism reduction. The new method is compared with previous methods of DRG and DRGEP. It was shown that DRG can tightly control the worst-case errors among all the species retained in the skeletal mechanism, but typically overestimates the error in the selected target species and thus results in under-reduced mechanisms. It is further shown that DRGEP may underestimate the errors in the selected target species due to the rather aggressive geometric error decay model, and result in reduction errors larger than the user-specified threshold values. In contrast, LEP can more accurately estimate the reduction error in the selected target species than DRG and DRGEP and thus can more effectively control the reduction error in the resulting skeletal mechanism.

A 35-species skeletal mechanism was developed using the LEP method for ethylene–air from the detailed USC-Mech II, and then a 146-species skeletal mechanism was developed for n-heptane–air from a 188-species skeletal mechanism previously developed using DRG. Both reduction cases are based on reaction states sampled from a wide range of pressures, temperatures, and equivalence ratios. Validation shows that the skeletal mechanisms can accurately predict such important flame behaviors as ignition delay time, extinction residence time, and laminar premixed flame speed.

It is further shown that reaction states sampled from PSR alone, including both the extinction and the ignition turning points, can be adequate to develop reduced mechanisms involving both the fast flame chemistry and the slow ignition chemistry, while such reaction states were sampled from both PSR and auto-ignition in previous studies.

Chapter 3. A Direct Method for Calculating the Turning Points of Perfectly Stirred Reactors

3.1. Introduction

As mentioned in section 1.2.2, steady-state PSR provides a simple and effective approach to study ignition and extinction limits of continuous flow combustors, which are typically associated with the turning points on the *S*-curves. The turning points on the PSR *S*-curves can typically be obtained by the marching-based methods such as arc-length continuation [77,78]. By automatically switching between temperature and residence time as the dependent variable, the solution can march across the turning points, where the Jacobian is singular for the original equations [81]. However, the marching method is computationally inefficient, particularly when high accuracy is required for turning point solution, and can be rather involved to be implemented. This is because the accuracy of the turning points obtained by the continuation method depends on the marching step size, such that marching step refinements are required to capture turning points for specific accuracy requirements.

In the present study, a direct method based on local optimization is proposed to accurately and efficiently obtain the turning points of PSR based on analytic Jacobian, and is compared with the arc-length continuation method. Then an analytical sensitivity evaluation method is proposed for reaction states of PSR, and the sensitivity of the ignition and extinction residence times in PSR are compared with the sensitivity of the ignition delay time and the laminar flame speed.

3.2. Methodology

The governing equations for the steady-state PSR can be expressed as

$$f_j(\boldsymbol{y}) = r_j(\boldsymbol{y}) + s_j(\boldsymbol{y}) = 0, j = 1,2,\dots,n_s + 1 \tag{3-1}$$

where r and s denote the spatially homogeneous reaction and mixing terms, respectively. The vector of dependent variables, $\boldsymbol{y}$, includes species mass fractions, $\boldsymbol{Y}$, and temperature, T. subscript j denotes the j^{th} governing equation. The detailed form of Eq. (3-1) can be found in Eq. (2-1). By solving the n_s+1 governing equations, the steady-state solution can be obtained for given residence time. Note that the system of equations can also be solved with residence time as a dependent variable for a specified temperature.

On the *S*-curve, the ignition point has the local maximum and the extinction point has the local minimum residence time. Therefore, the problem of computing such turning points can be formulated as a local optimization problem for residence time subject to Eq.(3-1), and the optimization problem can be transformed into the following algebraic equations using Lagrange multipliers.

$$\nabla\tau + \lambda_j \nabla f_j = 0, j = 1,2,\dots,n_s + 1 \tag{3-2}$$

where λ is the Lagrange multiplier and The vector form of Eq. (3-2) is

$$\begin{bmatrix} \frac{\partial f_1}{\partial Y_1} & \frac{\partial f_2}{\partial Y_1} & \cdots & \frac{\partial f_{n_s+1}}{\partial Y_1} \\ \frac{\partial f_1}{\partial Y_2} & \frac{\partial f_2}{\partial Y_2} & \cdots & \frac{\partial f_{n_s+1}}{\partial Y_2} \\ \vdots & \vdots & \ddots & \vdots \\ \frac{\partial f_1}{\partial T} & \frac{\partial f_2}{\partial T} & \cdots & \frac{\partial f_{n_s+1}}{\partial T} \\ \frac{\partial f_1}{\partial \tau} & \frac{\partial f_2}{\partial \tau} & \cdots & \frac{\partial f_{n_s+1}}{\partial \tau} \end{bmatrix} \begin{bmatrix} \lambda_1 \\ \lambda_2 \\ \vdots \\ \lambda_{n_s+1} \end{bmatrix} = \begin{bmatrix} 0 \\ 0 \\ \vdots \\ 0 \\ -1 \end{bmatrix} \tag{3-3}$$

The Jacobian matrix in Eq. (3-3) is analytically evaluated by using automatically generated subroutines for any specific mechanism [81], rather than through numerical perturbations, to achieve high accuracy and computational efficiency. It's noted that the Jacobian matrix with respect to $\boldsymbol{Y}$ and T is singular at the turning points, while the Jacobian matrix with respect to $\boldsymbol{Y}$ and τ is not [81].

To compute the reaction state $\boldsymbol{y}$ at the turning points, Eqs. (3-1) and (3-2) can be solved together through the Newton solver given a reasonably good initial guess, e.g. a solution from a neighboring state [82]. A reasonably good initial guess of the Lagrange multipliers can be obtained through inverting Eq. (3-3).

3.3. Results and Discussion

3.3.1. Validation of Turnings Points of PSR

The direct method is first validated against the continuation method for stoichiometric ethylene/air under atmospheric pressure and inlet temperature of 1000 K using the detailed USC-Mech II mechanism [80]. In the present study, a 10 K maximum temperature step size is utilized in the continuation method to ensure a high resolution of the *S*-curve. The results are shown in Figure 3-1, in which the *S*-curve is obtained by using the continuation method and the turning points are calculated by the new direct method. It is seen that both the extinction and the ignition turning points are captured by the direct method.

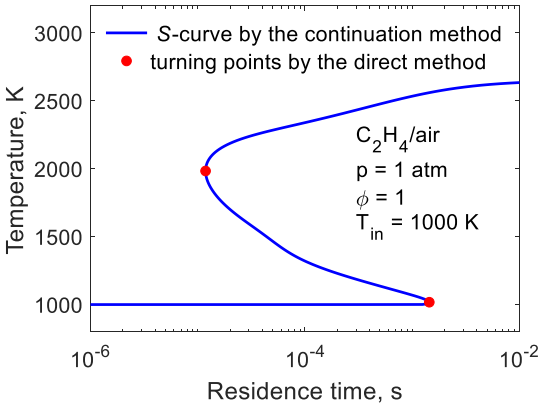

Figure 3-1. The *S*-curve of PSR for stoichiometric C_2H_4/air obtained by using the continuation method with the turning points calculated by using the direct method.

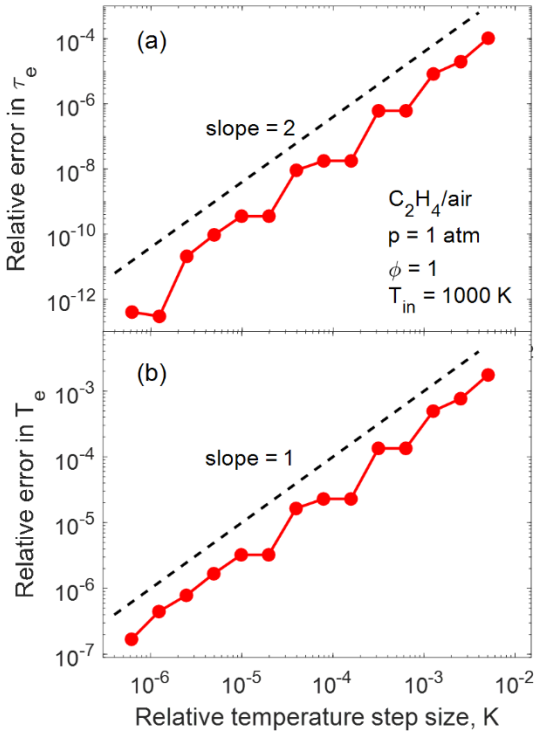

Figure 3-2. Relative errors in (a) residence time, and (b) temperature, at the extinction turning point in Figure 3-1 between the continuation method and the direct method as a function of the relative temperature step size in the marching.

Figure 3-2 shows the relative errors in the extinction residence time (τ_e) and extinction temperature (T_e) at the extinction turning point of the *S*-curve in Figure 3-1 between the continuation method and the direct method, as a function of the relative temperature step size for the marching. Note that the relative temperature marching step size is defined as the temperature marching step size normalized by T_e and the relative error is defined as the absolute value of the difference between the two solutions normalized by the value from the direct method. Since the error in the direct method is directly controlled by the error tolerance of the Newton solver, the solution from the direct method can be regarded as the exact solution for the comparison. It is seen that the relative errors in both panels of Figure 3-2 decrease as the marching step size decreases,

while an overall quadratic trend is observed for errors in τ_e and a linear trend is observed for errors in T_e. The different trend line slopes can be readily explained as the *S*-curve can be locally approximated as a parabola near the turning point, and this result indicates that a small marching step size is required by the continuation method to achieve high accuracy, particularly for T_e, resulting in a substantially higher computational cost than the direct method.

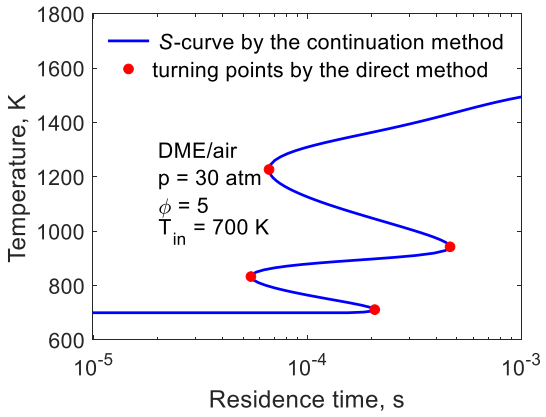

Figure 3-3. The *S*-curve of PSR for DME/air under 30 atm obtained by using the continuation method with the turning points calculated by using the direct method.

The *S*-curve can consist of multiple turning points resulting from the NTC and cool flame behaviors [81]. Figure 3-3 shows the *S*-curve of the dimethyl ether (DME)/air mixture, which features NTC behaviors, with an equivalence ratio of 5.0, pressure at 30 atm, and inlet temperature of 700 K calculated based on with a 39-species skeletal mechanism [83]. It is noted that the fuel-rich and high-pressure condition is selected such that the *S*-curve shows a pronounced cool flame branch. It is observed that the direct method can successfully capture the multiple turning points on the *S*-curve.

Similar to the *S*-curve, an additional mapping of the solutions of steady-state PSR is the *O*-curves, where the steady-state solution is computed with various equivalence ratios at fixed residence time [50]. The *O*-curve consists of a stable upper branch and an unstable lower branch which are analogous to the upper and middle branches of the *S*-curve. On the *O*-curve the leftmost turning point is the lean blow out (LBO) limit since no strongly burning flame exists with a leaner mixture, while the rightmost turning point is the rich blow out (RBO) limit. LBO limits are critical to the operational performance of combustion systems in propulsion and power generation. The direct method can be extended to calculate the LBO and RBO limits where the equivalence ratio has the local extrema value. Figure 3-4 shows the *O*-curve for ethylene/air under atmospheric pressure, inlet temperature of 700 K and residence time of 10^{-4} s. It is seen that the LBO and RBO are again successfully captured by the direct method.

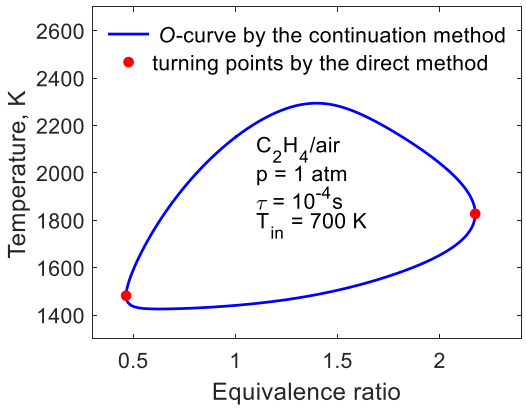

Figure 3-4. The *O*-curve of PSR for ethylene/air under atmospheric pressure, inlet temperature of 700 K and residence time of 10^{-4} s obtained by using the continuation method with the turning points calculated by using the direct method.

3.3.2. Turning Point Calculation for Various Reactor Conditions

The direct method is next employed to obtain the extinction and ignition states for ethylene/air of different equivalence ratios under atmospheric pressure and inlet temperature of 1000 K. To obtain the entire solution profiles, the turning points for stoichiometric mixture are first calculated by using the direct method with manually constructed initial guesses, and the turning points for rich and lean mixtures are subsequently obtained by marching from the stoichiometric solution. Figure 3-5 shows the profiles calculated by using the continuation and the direct methods, and it is noted that to obtain the turning points by using the continuation method, a segment of the *S*-curve needs to be solved for each equivalence ratio such that the computational cost is substantially higher than the direct method. In the present case, the continuation method shows a speedup factor of approximately 30. It is seen that the results collapse for the continuation and direct method, further demonstrating the validity of the new direct method in computing ignition and extinction states at different reactor conditions. Figure 3-6 further shows errors in residence time, and temperature, at the ignition and extinction turning points between the continuation method and the direct method, which is defined as the solution of the continuation method minus the solution of the direct method. Since the ignition and extinction turning points feature the local extreme residence time, the continuation method almost always under-predicts the ignition residence time and over-predicts the extinction residence time, which is evident in Figure 3-6a showing that the residence time errors are positive for extinction and negative for ignition. Furthermore, it is seen in Figure 3-6b that the errors in temperature are comparable to the marching step size in the continuation method, e.g. $\Delta T=10$ K, as the error in the temperature at the turning points obtained by the continuation method is bounded by the marching step size.

It is noted that extinction and ignition states under different inlet temperatures and pressures can be readily marched by using the direct method in a similar manner, while the results are not shown here.

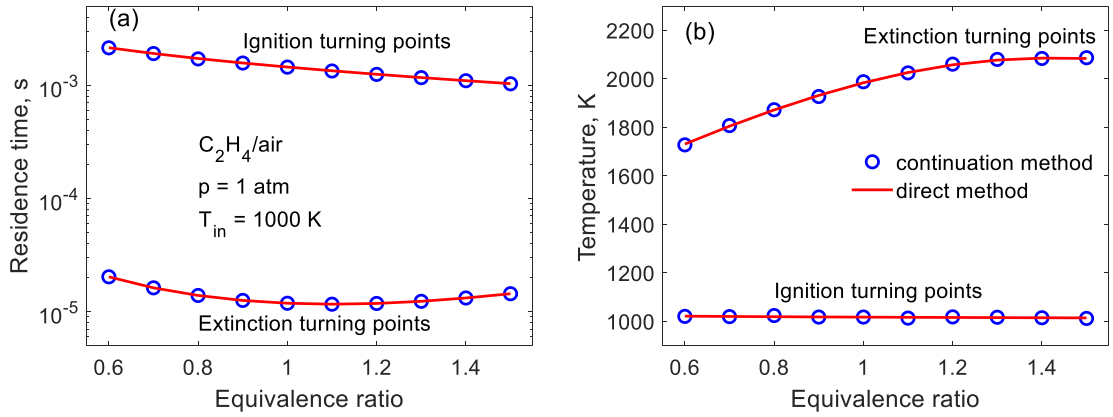

Figure 3-5. (a) Residence time and (b) temperature at the ignition and extinction turning points obtained by the continuation and direct methods, respectively, for ethylene/air of different equivalence ratios under atmospheric pressure and inlet temperature of 1000 K.

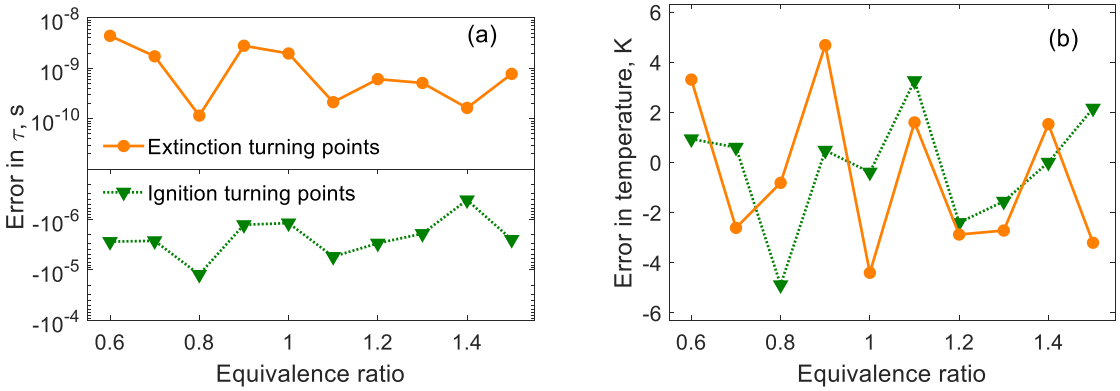

Figure 3-6. Errors in (a) residence time, and (b) temperature, at the ignition and extinction turning points between the continuation method and the direct method, for ethylene/air of different equivalence ratios under atmospheric pressure and inlet temperature of 1000 K.

3.3.3. Sensitivity Analysis of the Ignition and Extinction Points

Sensitivity analysis of the extinction and/or ignition turning points is frequently performed to identify the important reactions and optimize the kinetic mechanism [84]. The sensitivity of the residence time is defined as $\frac{d \ln \tau}{d \ln k_i}$, where k_i is the reaction rate coefficient of the i^{th} reaction, and it is typically evaluated numerically via the finite difference approach by perturbing the reaction rate coefficient and solving the PSR under fixed temperature, i.e.,

$$\frac{d\ln\tau}{d\ln k_i} \approx \frac{\ln \tau\big((1+\delta)k_i\big) - \ln \tau(k_i)}{\ln(1+\delta)} \tag{3-4}$$

where δ is the perturbation factor. The numerical evaluation is nevertheless known to be computationally expensive due to the large number of rate parameter perturbations and subsequent simulations. Meanwhile, δ should be chosen carefully, typically 1%, such that it is large enough to avoid numerical noise (discretization error) and small enough to avoid nonlinear effects. To accurately and efficiently evaluate the sensitivities, an analytical way is proposed.

Under a fixed temperature, the perturbed governing equations are

$$\boldsymbol{f}(\boldsymbol{y} + d\boldsymbol{y}, \boldsymbol{k} + d\boldsymbol{k}) = \boldsymbol{0} \tag{3-5}$$

where $\boldsymbol{k}$ is the vector of reaction rate coefficients and $\boldsymbol{y}$ is the vector of dependent variables, which consist of species mass fraction $\boldsymbol{Y}$ and residence time τ. By comparing Eqs. (3-1) and (3-5), the sensitivities can be formulated as:

$$\begin{gathered} \frac{\mathrm{d}\boldsymbol{y}}{d(\ln \boldsymbol{k})} = -\boldsymbol{J}^{-1} \cdot \boldsymbol{M} \\ M_{i,j} = \frac{W_i \nu_{i,j} \omega_j}{\rho}, i = 1, 2, \dots, n_s, j = 1, 2, \dots, n_r \\ M_{n_s+1,j} = \frac{-\sum_{i=1}^{KK} H_i \nu_{i,j} \omega_j}{\rho c_p} \end{gathered} \tag{3-6}$$

where $\boldsymbol{J}$ is the Jacobian matrix with respect to $\boldsymbol{Y}$ and τ, which is invertible on the turning points and $\boldsymbol{M}$ is the normalized stoichiometric matrix. W is the molecular weight, v is the stoichiometric coefficient, ω is the reaction rate, H is the enthalpy, ρ is the density and c_p is the mixture-averaged constant-pressure heat capacity. The subscript i indicates the i^{th} species and j indicates the j^{th} reaction and n_r is the number of reactions. Through solving the linear algebraic equations in Eq. (3-6), the sensitivities can be accurately obtained, which is far more efficient compared with the numerical perturbation method.

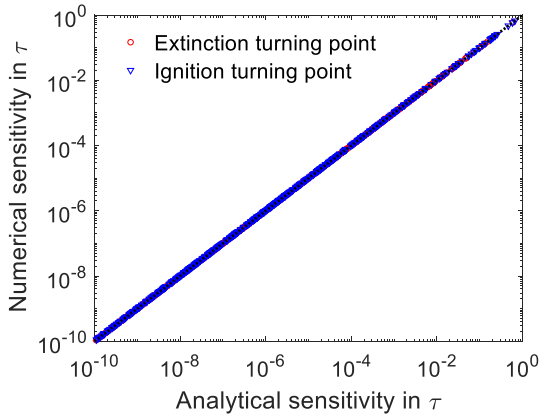

Figure 3-7. The analytical sensitivity vs. numerical sensitivity of τ for the extinction and ignition states on the *S*-curve of the stoichiometric ethylene/air under atmospheric pressure and inlet temperature of 1000 K.

Figure 3-7 shows the analytical sensitivity vs. numerical sensitivity of τ for the extinction and ignition states on the *S*-curve of the stoichiometric ethylene/air under atmospheric pressure and inlet temperature of 1000 K. It is seen that all the data points scatter on the 1:1 trend line, demonstrating the validity of the analytical method in evaluating the sensitivities.

To identify the relative importance of each reaction, the sensitivity vector is normalized by the maximum value, i.e.

$$SA_i = \frac{\frac{d\ln\tau}{d\ln k_i}}{\max_i \left|\frac{d\ln\tau}{d\ln k_i}\right|} \tag{3-7}$$

Such that an important reaction has an absolute *SA* value close to unity.

Firstly, the normalized residence time sensitivity of the ignition states in PSR is compared with the normalized ignition delay time sensitivities, which is defined as $\frac{\frac{d\ln\tau_{IDT}}{d\ln k_i}}{\max_i \left|\frac{d\ln\tau_{IDT}}{d\ln k_i}\right|}$, where τ_{IDT} is the ignition delay time. Figure 3-8 lists the ten most important reactions and their normalized sensitivity values for the ignition residence time of PSR and ignition delay time for stoichiometric ethylene/air under atmospheric pressure and inlet temperature of 1000 K. It is seen that the ten most important reactions to ignition delay time are similar to that of the ignition residence time and both of them contains R194, R195, R14, R254, R96, R251, and R266. It is further seen that the ignition processes are typically dominant by chain branching reactions containing fuel-related species such as C_2H_4 and C_2H_3. Figure 3-9 further shows an overall linear correlation between the normalized ignition delay time sensitivities and the normalized ignition residence time sensitivities. The level of alignment is also assessed by the inner product between the two sensitivity directions, which is around 0.9, indicating that the ignition reaction state on PSR can capture the important chemistry for the auto-ignition process.

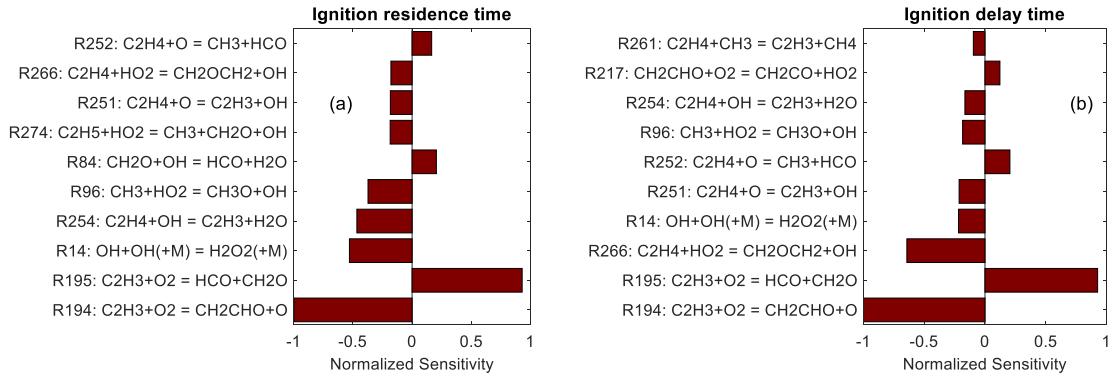

Figure 3-8. The ten most important reactions for (a) the ignition residence time of PSR and (b) the ignition delay time of stoichiometric ethylene/air under atmospheric pressure and inlet temperature of 1000 K

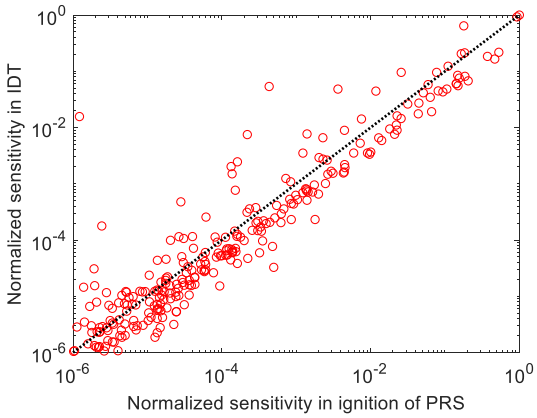

Figure 3-9. The normalized ignition delay time sensitivities vs. the normalized ignition residence time sensitivities.

Since the extinction turning point on PSR is related to the strongly burning states, the normalized extinction residence time sensitivities are then compared with the normalized flame speed sensitivities defined as $\frac{\frac{d\ln SL}{d\ln k_i}}{\max_i\left|\frac{d\ln SL}{d\ln k_i}\right|}$, where *SL* indicates the laminar flame speed. Figure 3-10 lists the most important ten reactions and their normalized sensitivity values for the extinction

residence time of PRS and flame speed of stoichiometric ethylene/air under atmospheric pressure and inlet temperature of 300 K. It is again seen that the most important ten reactions to the flame speed and the extinction in PSR are similar. Both of the flame speed and PSR extinction residence time are most sensitive to the rate of R1 $H+O_2=O+OH$, which is the major branching step. The second-ranked reaction is R31 $CO+OH=CO_2+H$, whose reaction rate determines the final heat release and temperature of the system, which are the key elements to sustaining oxidation in the extinction region. It is further observed that the strongly burning chemistry is primarily controlled by the reactions involving small molecules, such as H, OH, CO, and HCO. Similar to Figure 3-10, Figure 3-11 further shows an overall linear correlation between the absolute normalized laminar flame speed sensitivities and the normalized extinction residence time. The similarity between the two sensitivity vectors is around -0.94, showing that the extinction reaction state on PSR can capture the important chemistry for the strongly burning flames. The negative value indicates that the reactions which increase the flame speed make the flame harder to extinguish.

While the results are not displayed here, similar results can be observed for n-butane/air and n-heptane/air.

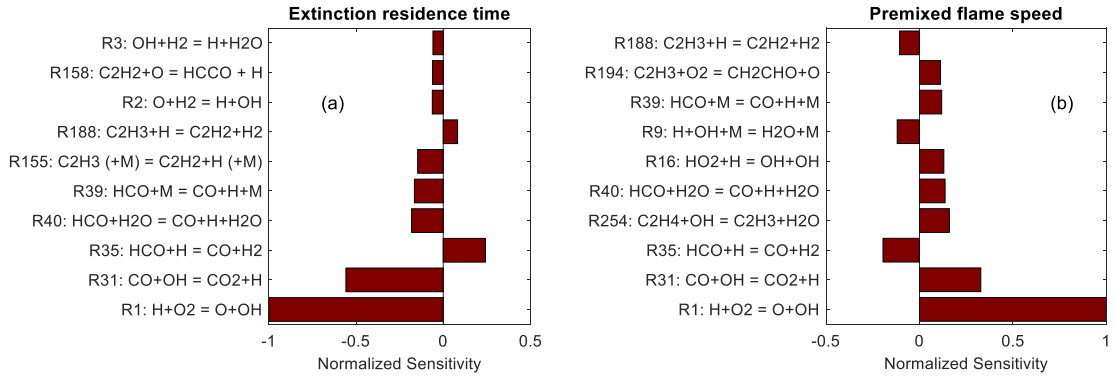

Figure 3-10. The ten most important reactions for (a) the extinction residence time of PSR and (b) the laminar flame speed of stoichiometric ethylene/air mixtures under atmospheric pressure and inlet temperature of 300 K

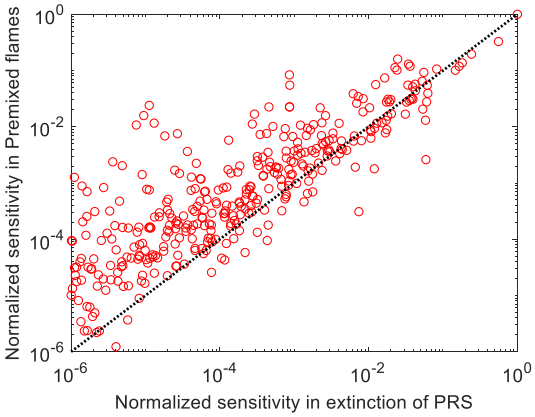

Figure 3-11. The normalized laminar flame speed sensitivities vs. the normalized extinction residence time sensitivities.

3.4. Conclusions

A direct method based on local optimization is developed to accurately and efficiently compute the extinction and ignition turning points of PSR. In the direct method, a set of algebraic equations based on analytic Jacobian are formulated based on Lagrange multipliers and solved by using the Newton solver with a reasonably good initial guess. The direct method is compared with the continuation method in obtaining the ignition and extinction turning points on the *S*-curve of PSR. It is seen that the direct method can accurately capture the turning points while the accuracy of the continuation methods depends on the marching step size. It is also shown that the direct method can be extended to calculate multiple turnings on the *S*-curve and the LBO and RBO of the *O*-curve. Furthermore, extinction and ignition turning points of various operating conditions

can be readily obtained by marching from existing solutions using the direct method, which is substantially more efficient than the continuation method.

Furthermore, an analytical method is proposed to effectively and accurately evaluate the sensitivities of the steady-state PSR solutions. The analytical method is then compared with the commonly used numerical method, demonstrating the validity of the analytical method. Next, the sensitivity of the ignition and extinction residence time are compared with the sensitivity of the ignition delay time and the laminar flame speed. It is seen that the ignition and extinction states on PSR can capture the important chemistries to the ignition process and strongly burning flame, further indicating that reaction states sampled from PSR including both the extinction and the ignition turning points can be adequate to develop reduced mechanisms involving both the fast flame chemistry and the slow ignition chemistry. It is further observed that the controlling reactions to ignition process typically contains fuel-related species, while the strongly burning flame chemistry is highly sensitive to small-molecule reactions regardless of mixtures.

Chapter 4. Skeletal and Reduced Mechanisms for Gasoline and Gasoline/Ethanol Surrogates for Engine CFD Applications

4.1. Introduction

As reviewed in section 1.2.3, to optimize the engine design and apply advanced engine techniques, CFD simulations serve as a valuable tool in understanding the combustion process in SI engines, for example, explaining the knocking phenomena. Due to the complex composition of the real gasoline fuels, it is not practical to include all the fuel components in simulations and simple fuel surrogates consisting of a limited number of components are frequently used to reproduce the physical and chemical properties of real gasoline fuels. Recently, TPRF has been widely used as gasoline surrogate since it can capture both the octane number and octane sensitivity. Meanwhile, to meet the requirements of the clean air act and renewable fuel standard, most of the gasoline presently sold in the United States contains ethanol. Therefore, a comprehensive mechanism for TPRF/ethanol surrogates is needed to accurately predict knocking in engine simulations. A detailed mechanism for gasoline surrogates developed by LLNL is comprised of 1389 species and 5935 elementary reactions [64], while such large-sized mechanism can hardly be applied in 3-D engine simulations, and thus mechanism reduction is required.

In the present study, an integrated method that combines DRG, DRGASA, isomer lumping and LQSSA was employed to derive the skeletal and reduced mechanisms from the detailed LLNL mechanism, incorporating low-temperature kinetics for mixtures of TPRF and ethanol. The skeletal and reduced mechanisms were then extensively validated against the detailed mechanism and available experimental data. The skeletal mechanism was further validated against the experimental data in predicting the critical compression ratio in a CFR engine.

4.2. Methodology

4.2.1. Reaction States Sampling

To derive a skeletal mechanism suitable for SI engine applications, the reduction was performed within the parameter range of pressure from 1 to 100 atm and equivalence ratio from 0.5 to 1.3. The initial temperature for ignition problems was set to be 750 to 1800 K, such that the low-temperature chemistry, which is important in some SI engine ignition studies, is included in the reduction. The inlet temperature for extinction applications in PSR was 300 K. Since the skeletal mechanism is intended to be used in simulations of the mixtures of ethanol and practical gasoline, the sampled fuels should cover all the possible fuel compositions. Based on previous reduction processes, DRGASA for a single fuel with a similar number of species and a similar range of sampling parameters takes around one week, therefore a limited number of fuels should be selected due to the consideration of the computational cost. Lastly, an overall eleven fuel mixtures listed in Table 4-1 were selected. The sampled TPRF fuels had a RON range from 65 to 93 and an octane sensitivity range from 1.1 to 12. These ranges cover almost all the practical gasoline fuels according to the data in Kalghatgi et al. [60]. Ethanol mole percentages of 0%, 50%, and 100% were considered in the sampling, such that the obtained skeletal mechanism can be applied to mixtures of TPRF and ethanol. It's noted that PRF60 and PRF100 were also included in the sampling such that the obtained mechanism could also be applied to PRF surrogates.

Table 4-1. Composition (mole percentage), octane numbers, and sensitivity of the sampled fuels

Fuel	iso-Octane	n-Heptane	Toluene	Ethanol	RON	MON	Sensitivity
1	100	0	0	0	100	100	0
2	60	40	0	0	60	60	0
3	0	50	50	0	65.9	57.7	8.2
4	33	33	34	0	76.2	70.9	5.3

5	75	15	10	0	85.7	84.6	1.1
6	0	25	75	0	93.4	81.5	11.9
7	0	25	25	50	NA	NA	NA
8	16.5	16.5	17	50	NA	NA	NA
9	37.5	7.5	5	50	NA	NA	NA
10	0	12.5	37.5	50	NA	NA	NA
11	0	0	0	100	NA	NA	NA

4.2.2. Reduction Process

DRG was employed as the first step in the reduction due to its high capability in dealing with extremely large mechanisms. In the DRG method, each species in the detailed mechanism is represented by a node in the DRG. The relative error in species *A* induced by the elimination of species *B*, r_{AB}, is estimated for every pair of species in the mechanism. An error tolerance, ϵ, can be specified for the DRG method such that there exists a directed edge from species *A* to species *B* if r_{AB} is larger than ϵ at any reaction state in the sampling space. Then the set of remained species can be obtained by the deep first search (DFS) of the graph from a starting species [12]. Typically, the H radical is selected as the starting species since it is always important in hydrogen and hydrocarbon combustion process. An improved definition of r_{AB} in Luo et al. [14], which considers the presence of large isomer groups, compared with the original definition in Lu and Law [12] was used in the present work. The improved DRG method also features high efficiency and has been implemented for parallel computation. It takes only a few minutes to process tens of thousands of sampled reaction states using a small PC cluster.

The number of remaining species as a function of the user-specified threshold value is plotted in Figure 4-1. Based on Luo et al. [85], a reasonable large reduction error tolerance, say 20~40%, can be specified without the elimination of important species. In the present reduction process, the threshold value was set to be 0.3 such that the possible important species are retained

in the skeletal mechanism. After the implementation of DRG, a skeletal mechanism consisting of 695 species and 3380 reactions was obtained.

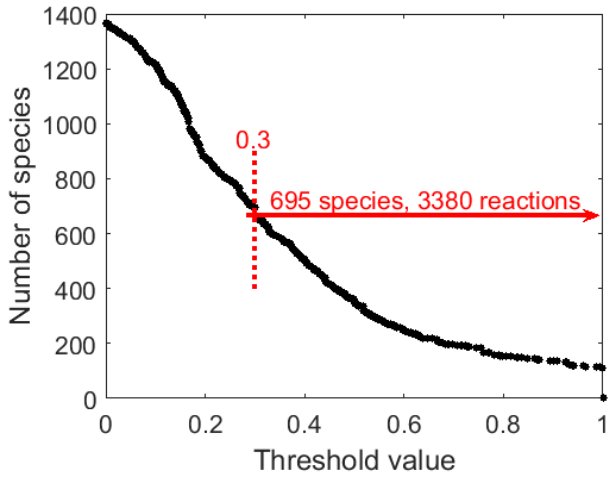

Figure 4-1. The number of remaining species as a function of the threshold value.

Due to the high nonlinearity of chemical kinetics, probably the only reliable approach to quantify the reduction errors is to directly measure the actual reduction errors by comparing the solutions before and after the species elimination. Therefore, DRGASA was subsequently employed to obtain the smallest skeletal mechanisms that can accurately predict the selected targets.

In DRGASA, the first step is to choose the species for sensitivity analysis based on the DRG results. Second, the sensitivities ϵ_i, defined as the worst-case error induced to the parameters of interest due to the elimination of the species i, are computed for each species that are selected for sensitivity analysis. Third, the species are eliminated from the mechanism one at a time following the ascending order of ϵ_i until the worst-case error in the parameters of interest is larger

than the user-specified level. The above procedure is then repeated until further elimination of any single species would result in larger than acceptable error.

In the present study, all the 695 species in the skeletal mechanism were selected for sensitivity analysis in order to achieve the maximum extent of reduction. The target parameters include the ignition delay time of auto-ignition under constant pressure, the extinction residence time and the strongly burning flame temperature in PSR. The worst-case error tolerance was set to be 0.4. It was found that such an error tolerance was comparable to the overall uncertainty of the detailed mechanism such that there is no significant loss in chemical fidelity through the skeletal reduction. Due to the high nonlinearity of the reaction mechanism, the reduction error caused by the removal of a set of species is by no means the sum of the errors induced by the elimination of each species. Therefore, the elimination of two species with the worst-case error larger than the user-specified tolerance may cause a worst-case error smaller than the tolerance. This phenomenon, which is called the error cancellation, was further utilized in the DRGASA to minimize the mechanism size in the present work. The resulting skeletal mechanism consists of 167 species and 839 elementary reactions.

DRGASA is typically accelerated by parallel computing, due to the time consuming iterative evaluation of the global parameters. In the present work, DRGASA was performed on a 256-core PC cluster, and the reduction took around three weeks including the manual stage for problem setup.

To further reduce the size of the skeletal mechanism, isomer lumping developed by Lu and Law [41] is applied. The identification of isomer groups can be achieved through statistics. Two isomers can be grouped if their concentrations are correlated approximately by a constant factor for all the sampled reaction states. For the present study, the isomer lumping process only finds

one isomer group which includes NC7KET24/0.333, NC7KET35/0.409, and NC7KET42/0.258, where the value next to each isomer represents the intragroup mass fraction of the isomer. Finally, a 165-species skeletal mechanism with 839 elementary reactions is obtained.

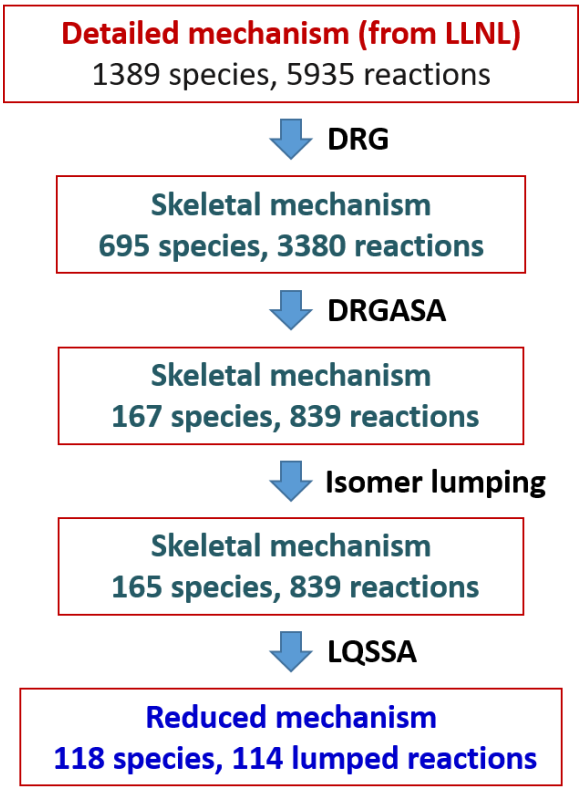

Figure 4-2. The reduction flow chart.

The 165-species skeletal mechanism was further reduced by eliminating the fast exhausted radicals approximated to be in steady-state. In the present study, a critical timescale, τ_c, i.e. the extinction residence time of PSR in extinction applications and auto-ignition delay time in ignition application, was selected to separate the fast and slow chemical modes, such that the chemical processes with a timescale significantly shorter than τ_c can be considered exhausted for a residence time much larger than τ_c. Then the QSS species can be identified if they are only projected to the

fast modes [33]. Consequently, 47 species were identified as globally valid QSS species, and a 118-species reduced mechanism was obtained with the elementary reactions lumped to 114 semi-global steps, where the QSS species concentrations were solved analytically using LQSSA, which is much more efficient compared with the previous internal algebraic iteration method [86].

In summary, the entire reduction flow chart is displayed in Figure 4-2.

4.3. Results and Discussion

4.3.1. Validations of Ignition Delay Time and Flame Speed

In 3-D SI engine simulations, ignition delay time and flame speed are both of great interest. Therefore, to demonstrate the fidelity of the resulting 118-species reduced mechanism and the 165-species skeletal mechanism, validations against the detailed mechanism and experimental results in ignition delay time and laminar flame speed were conducted for various operating conditions when experimental data are available, starting from pure component of iso-octane, n-heptane, toluene and ethanol to the quaternary mixtures of them.

4.3.1.1. Validations of Single Component Fuels

As fundamental components of gasoline surrogates, the ignition delay times of pure iso-octane, n-heptane and toluene have been extensively studied by different groups in recent decades. The ignition delay times for stoichiometric and lean iso-octane/air under different pressures measured by Fiewege et al. [87], Davidson et al.[88], Shen et al. [89], and Mehl et al. [64] are displayed in Figure 4-3. Ciezki et al. [90] and Gauthier et al. [91]'s experimental data of stoichiometric and lean n-heptane/air under different pressures are shown in Figure 4-4. For toluene ignition delay times, the shock tube data obtained by Mehl et al. [64] is shown in Figure 4-5. The simulation results based on the detailed, skeletal and reduced mechanisms, indicated by

solid, dotted and dot-dashed lines respectively, are also displayed in Figure 4-3 to Figure 4-5. It is readily observed that the reduced and skeletal mechanisms agree well with the detailed mechanism and predict the experimental data accurately. It can be further found that the reduced model gives almost the same results as the skeletal model, which is also true for the following validation results, indicating the identification of QSS species is successful.

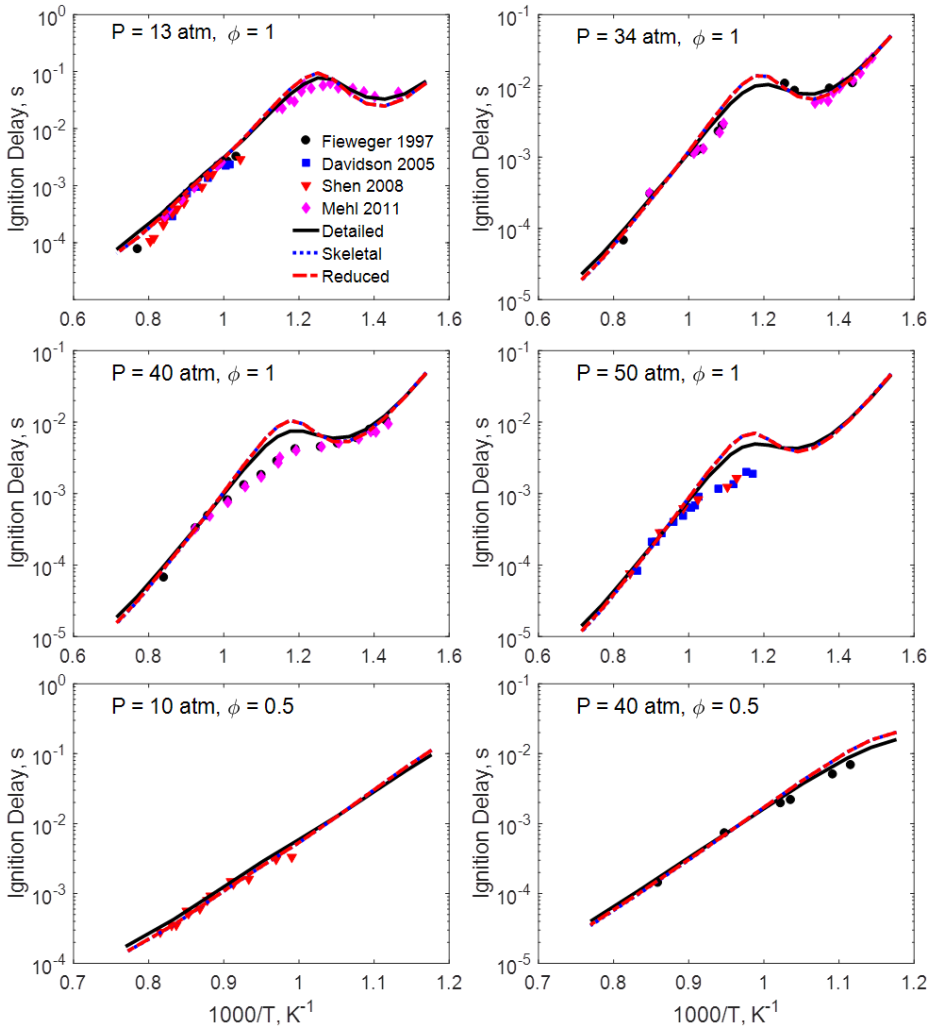

Figure 4-3. Ignition delay times of stoichiometric and lean iso-octane/air under different pressures.

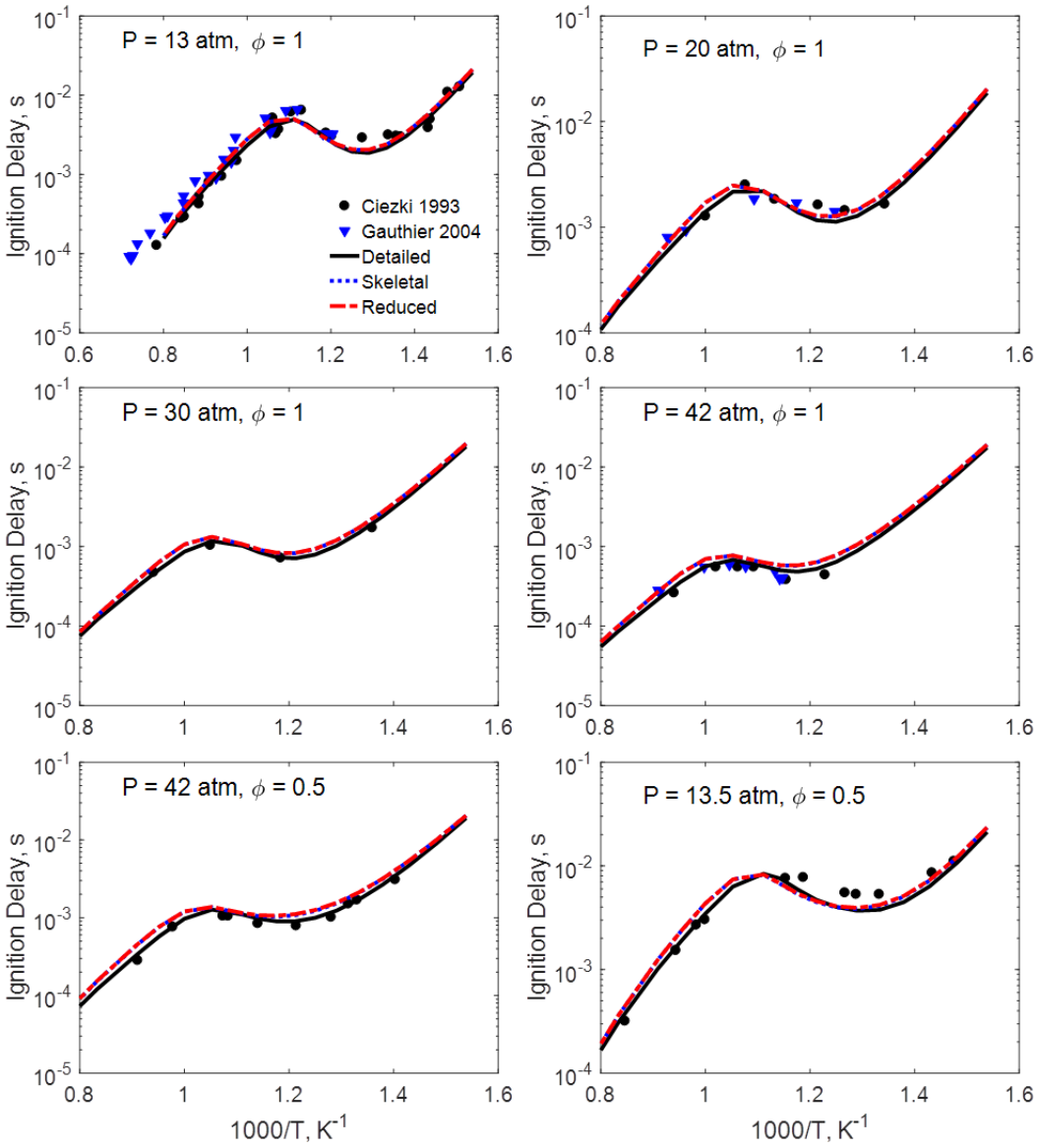

Figure 4-4. Ignition delay times of stoichiometric and lean n-heptane/air under different pressures.

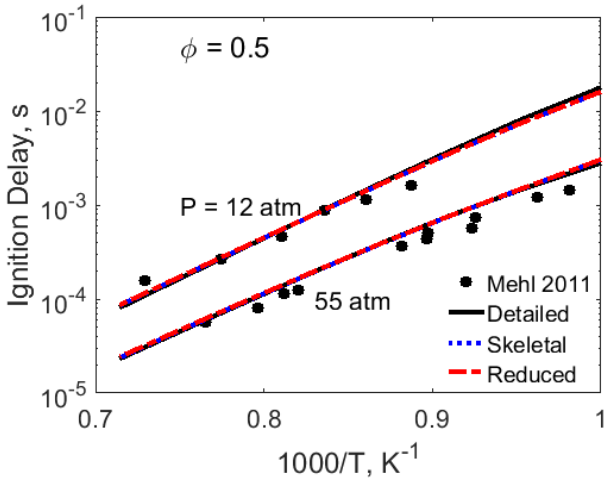

Figure 4-5. Ignition delay times of stoichiometric toluene/air under 12 and 55 atm.

The laminar flame speeds of iso-octane, n-heptane, toluene and ethanol under atmospheric pressure and different initial temperatures are also studied by lots of groups such as Davis et al. [92], Kwon et al. [93], Huang et al. [94], Kumar et al. [95], van Lipzig et al. [96], Dirrenberger et al. [97], and Hirasawa et al. [98] in recent decades. Figure 4-6 to Figure 4-9 show the experimentally measured and numerically simulated flame speeds for iso-octane, n-heptane, toluene, and ethanol respectively. Similar to Figure 4-3 to Figure 4-5, the symbols denote experimental data, while solid, dotted and dot-dashed lines stand for detailed, skeletal and reduced mechanism simulation results respectively.

For iso-octane and ethanol, Figure 4-6 and Figure 4-9 indicate that the reduced and skeletal mechanisms reproduce the results of the detailed mechanism accurately and they both show reasonable agreement with the experimental values. However, the reduced and skeletal models predict slightly higher flame speeds than the detailed model for n-heptane in Figure 4-7, while for toluene, the flame speeds are slightly underpredicted by the reduced and skeletal models compared with the detailed model in Figure 4-8. The possible explanation is that the pure n-heptane or pure

toluene was not directly included in the samplings. Therefore as extended validations, the 15% worst case discrepancies shown in Figure 4-7 and Figure 4-8 are acceptable.

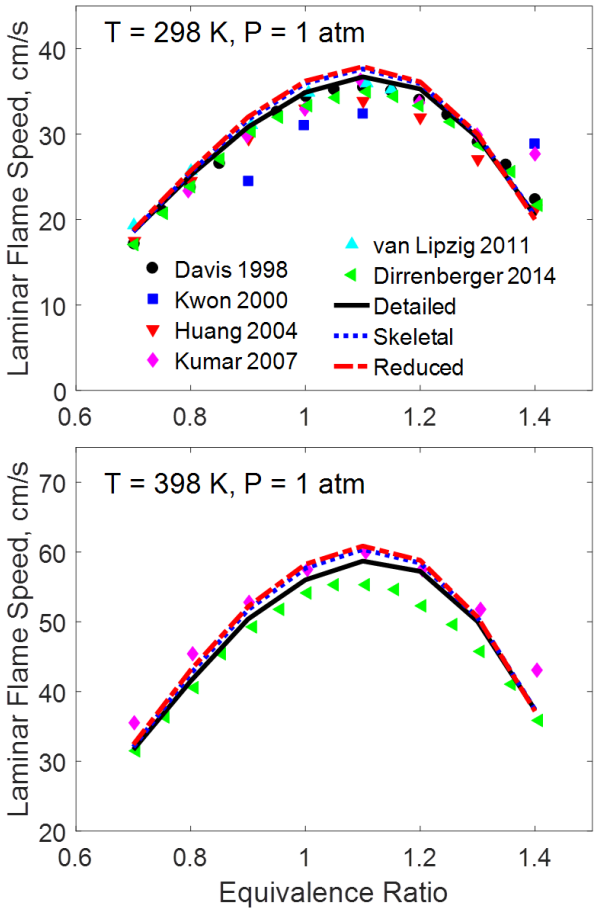

Figure 4-6. Laminar flame speeds of iso-octane/air under atmospheric pressure and initial temperatures of 298 and 398 K.

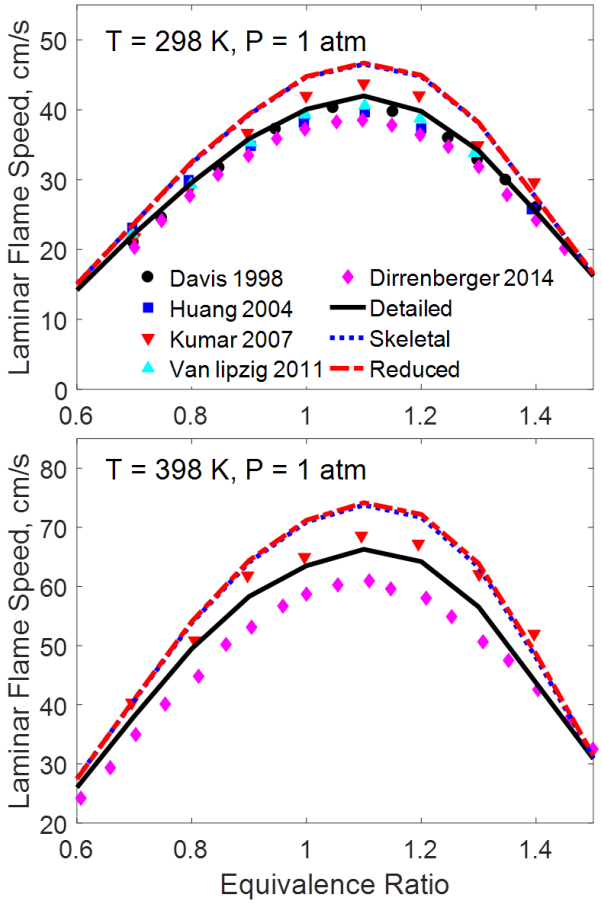

Figure 4-7. Laminar flame speeds of n-heptane/air under atmospheric pressure and initial temperatures of 298 and 398 K.

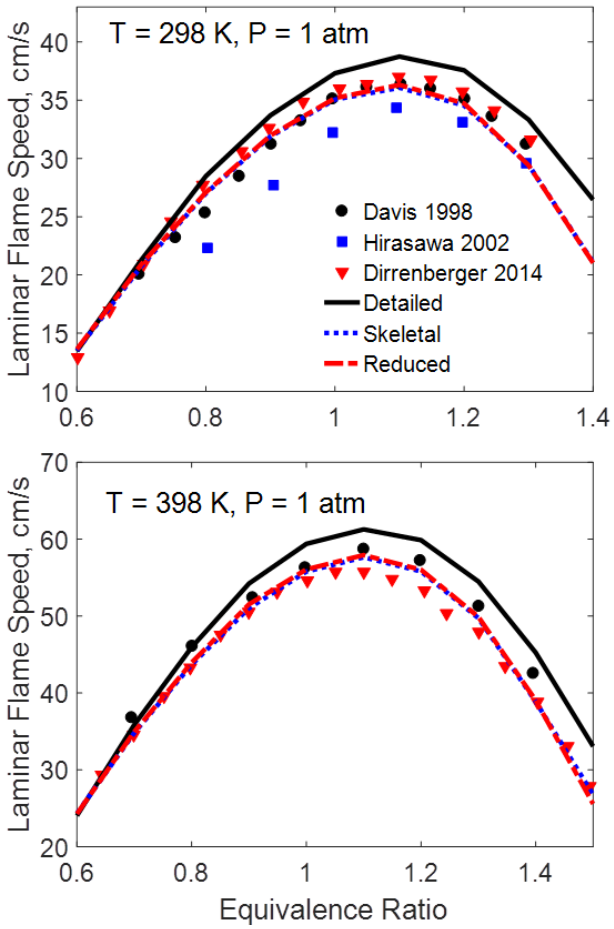

Figure 4-8. Laminar flame speeds of toluene/air under atmospheric pressure and initial temperatures of 298 and 398 K.

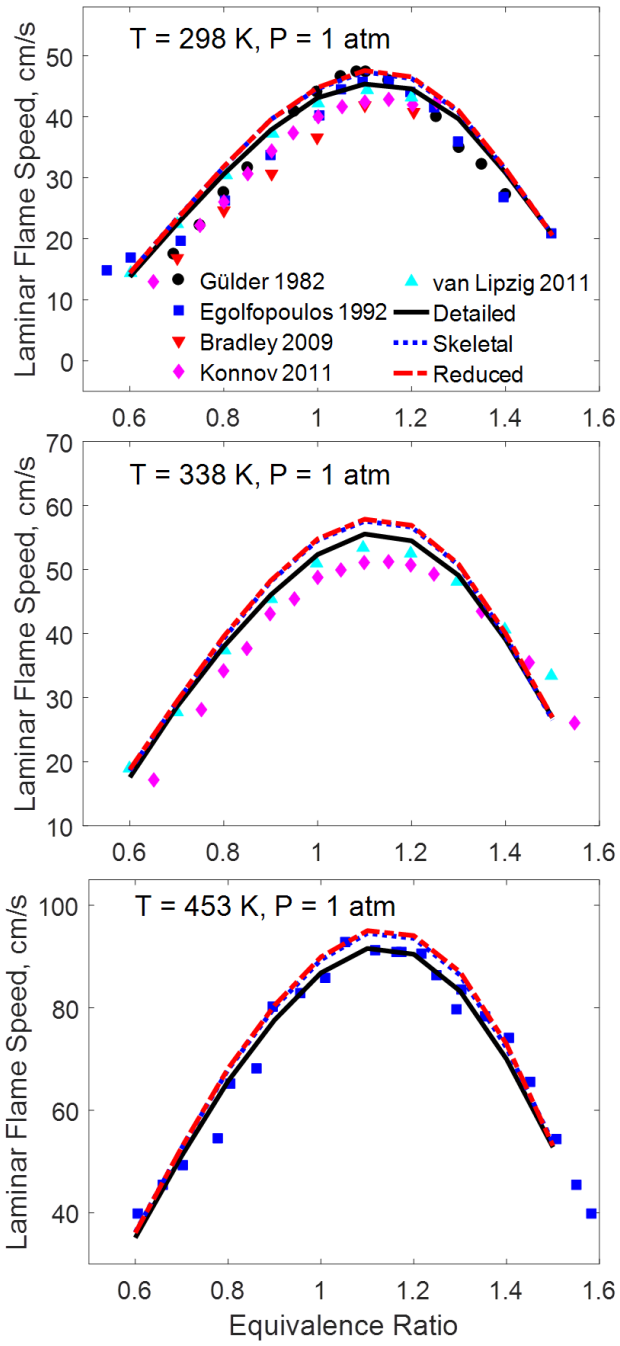

Figure 4-9. Laminar flame speeds of ethanol/air under atmospheric pressure and initial temperatures of 298, 338, and 453 K.

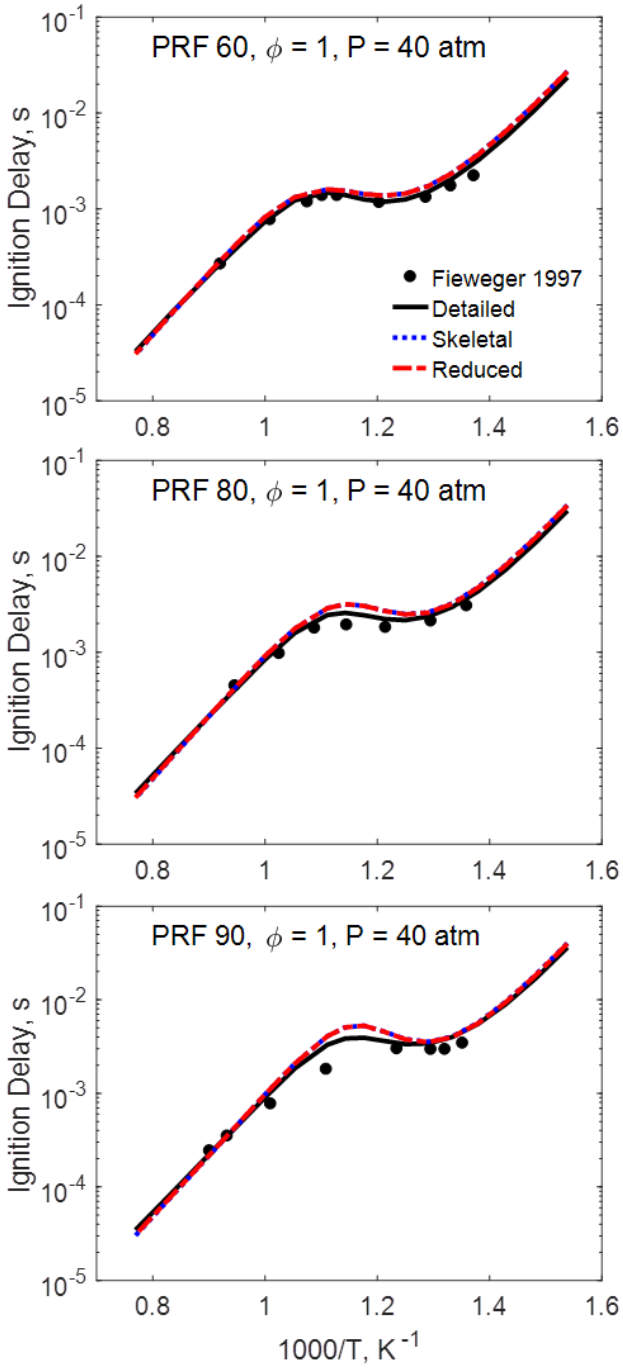

Figure 4-10. Ignition delay times of stoichiometric PRF 60, PRF 80, and PRF 90 under 40 atm.

4.3.1.2. Validations of PRF Surrogates

PRF mixtures are very common gasoline surrogates, such that their ignition delay times and flame burning velocities have been extensively studied by numerous groups. In order to

demonstrate that the reduced and skeletal mechanisms can be applied to PRF mixtures, validations are conducted in this subsection.

For the ignition delay time validations, the shock tube data measured by Fieweger et al. [87] is used. They reported the ignition delay times of stoichiometric PRF 60, PRF 80, and PRF 90 under relatively high pressure of 40 atm. The experimental and simulation values are plotted in Figure 4-10. The figure illustrates that the results of the reduced and skeletal models almost collapse with the detailed model results and they predict the experimental data quite well.

The laminar flame speeds of PRF 90 at ambient pressure were measured by Huang et al. [99] at an initial temperature of 298 K, as well as Bradley et al. [100] at 358 K. As shown in Figure 4-11, the reduced mechanism results collapse with the skeletal mechanism, and their worst-case error compared with the detailed mechanism is 4%, which can be ignored compared to the uncertainty of the detailed mechanism. Moreover, both the reduced and the skeletal mechanism have the capability of reasonably predicting the experimental results.

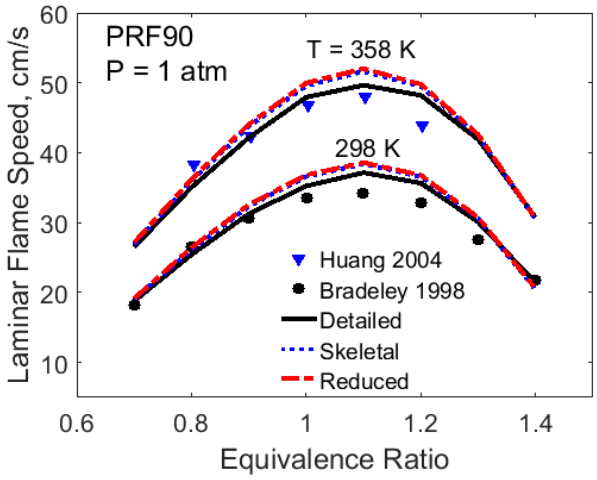

Figure 4-11. Laminar flame speeds of stoichiometric PRF90/air under atmospheric pressure and initial temperature of 298 K and 358 K.

PRF 87 was investigated by Jerzembeck et al.[101] under a relatively high temperature of 373 K and a high pressure of 10 to 25 bar, which are engine conditions. The numerical results based on reduced, skeletal and detailed mechanisms are compared with the experimental data in Figure 4-12, showing that the flame speeds of lean to stoichiometric mixtures are well predicted by the reduced, skeletal and detailed mechanisms. However, there exist relatively large discrepancies when it comes to the rich and high-pressure conditions, which are also found in Beeckmann et al. [102]. This phenomenon might be attributed to the experimental uncertainties caused by the development of wrinkles for rich mixtures in the experiments as reported by Jerzembeck et al. [101]. Despite these discrepancies, the reduced and skeletal mechanisms give almost the same results as the detailed one.

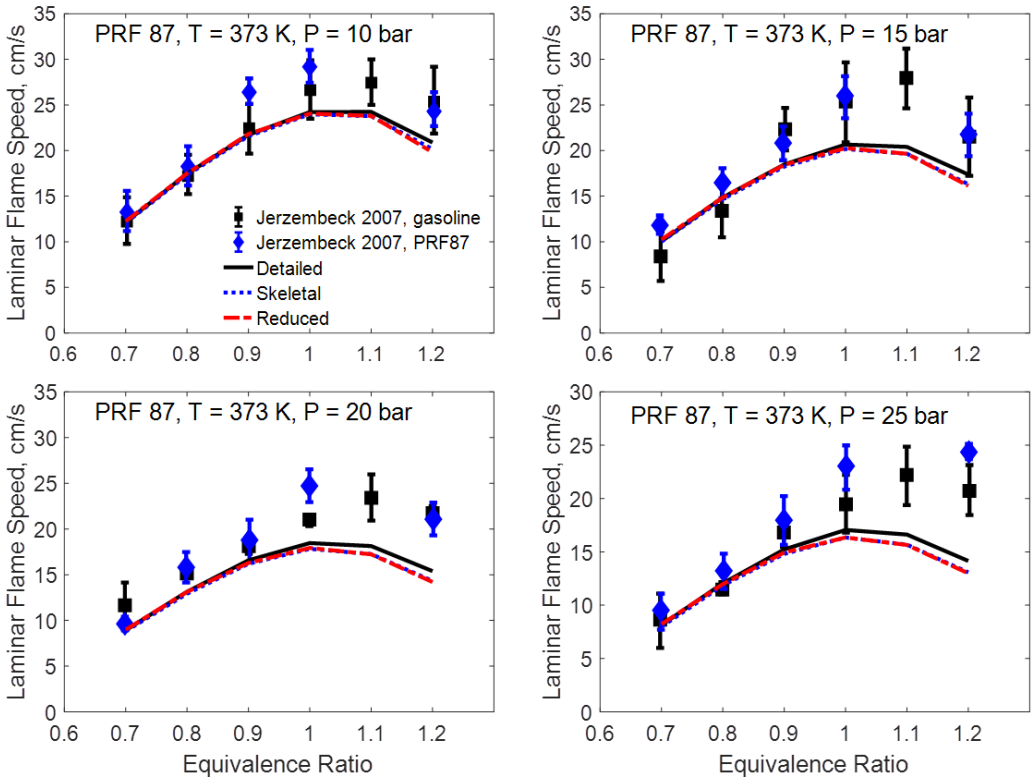

Figure 4-12. Laminar flame speed of PRF87/air under initial temperature of 373 K and pressure of 10, 15, 20, and 25 bar.

Exhaust gas recirculation is an effective method to reduce NOx emissions in engines, while the flame burning velocity will be obviously reduced by the dilution of the exhaust gases. The dilution effects on the laminar flame speed were studied by Zhao et al. [103] for PRF87 under an initial temperature of 353 and 500 K for an equivalence ratio of 0.84 with N2 as the diluent. The measurement results, as well as the simulation values, are plotted in Figure 4-13. From the figure, we can find that the reduced and skeletal mechanism results almost overlap with the detailed mechanism results and agree well with the experimental data. The reduced and skeletal models reproduce the linear dependence between the laminar flame speed and the dilution ration, which is consistent with the studies in Zhao et al. [104].

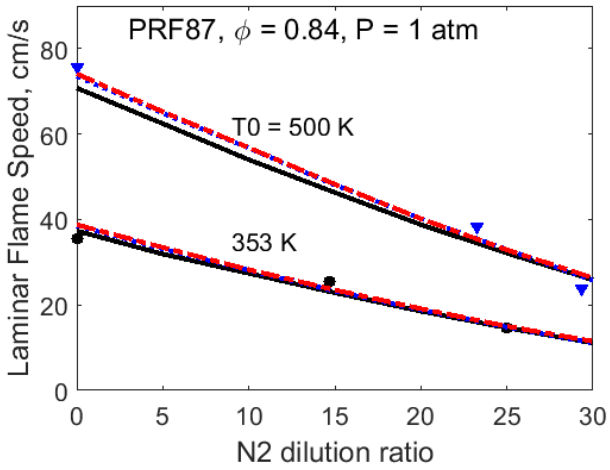

Figure 4-13. Laminar flame speed of PRF 87 as a function of N2 dilution percentages under atmospheric pressure and initial temperature of 353 and 500 K. Symbols denote the experimental measurements by Zhao et al.[103], Solid, dashed and dot-dashed lines show the numerical results based on the detailed, skeletal and reduced mechanism respectively.

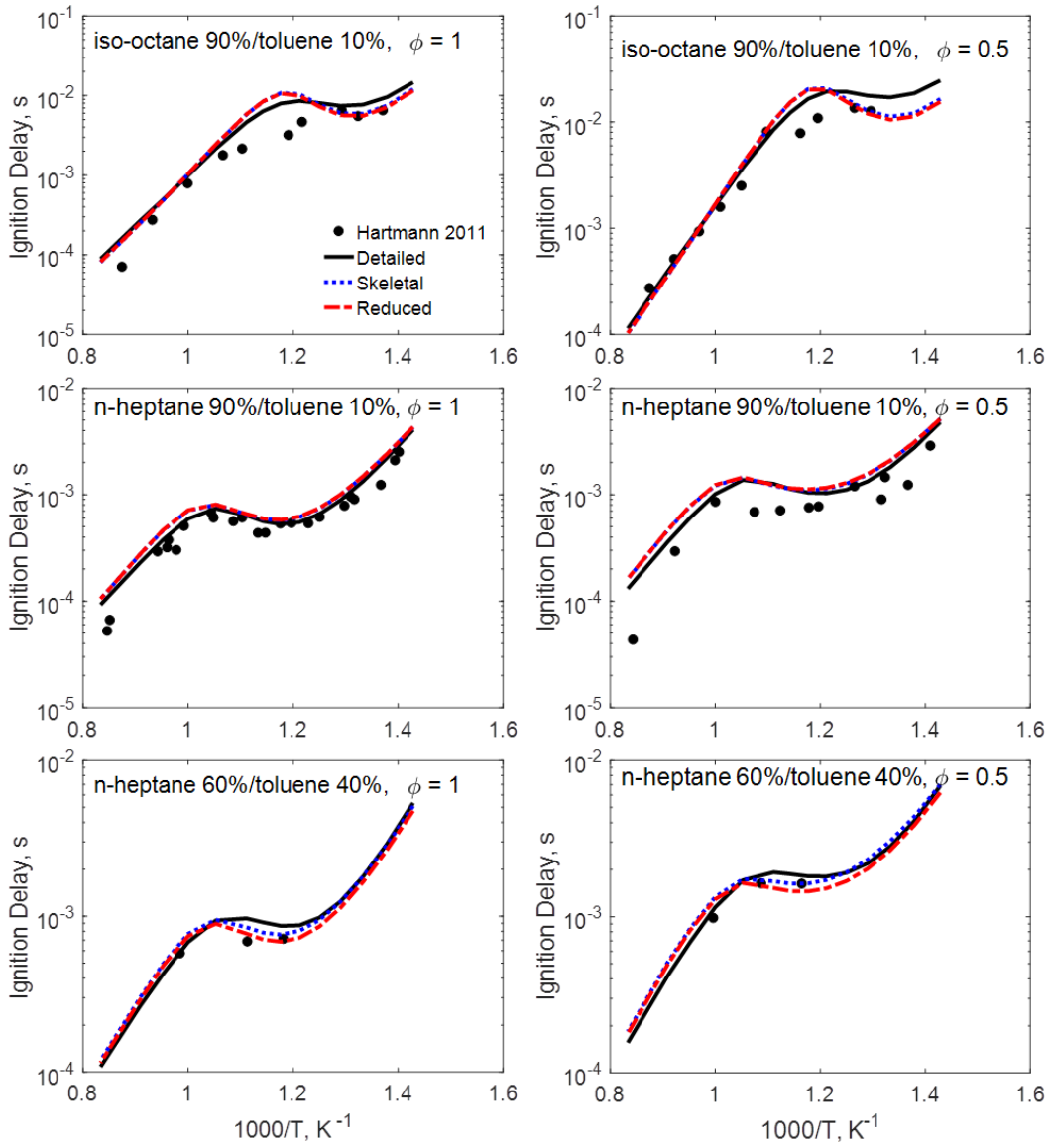

Figure 4-14. Ignition delay times of lean and stoichiometric n-heptane/toluene (90%/10% and 60%/40% by liquid volume) and iso-octane/toluene (90%/10%) under pressure of 40 bar.

4.3.1.3. Validations of Mixtures with Toluene

In this subsection, the performance of reduced and skeletal mechanisms is explored for mixtures with toluene in various experimental configurations.

Firstly bi-composition fuels such as iso-octane/toluene and n-heptane/toluene are validated. Ignition delay times of lean and stoichiometric n-heptane/toluene (90%/10% and 60%/40% by liquid volume), as well as iso-octane/toluene (90%/10%), have been reported under pressure of 40 bar by Hartmann et al. [105]. Experimental data are shown in Figure 4-14 compared with the numerical values and good agreements between the results of the reduced, skeletal and detailed mechanisms can be observed. Also, the simulation results can reasonably predict the experimental data.

Then for the validation of the TPRF surrogates, the shock tube data by Gauthier et al.[106] are used. These data have been reported for two mixtures, referred to as Surrogate A (n-heptane/iso-octane/toluene – 17%/56%/28% by mole fraction) and B (17%/63%/20%). Both surrogates have an average octane number of 87, defined as the average of RON and MON. The ignition delay times of stoichiometric Surrogate A/air and Surrogate B/air under pressure of 20 and 55 atm are displayed in Figure 4-15. It can be observed that the reduced, skeletal and detailed models demonstrate the capability to predict the measured ignition delay time satisfactorily under both pressures.

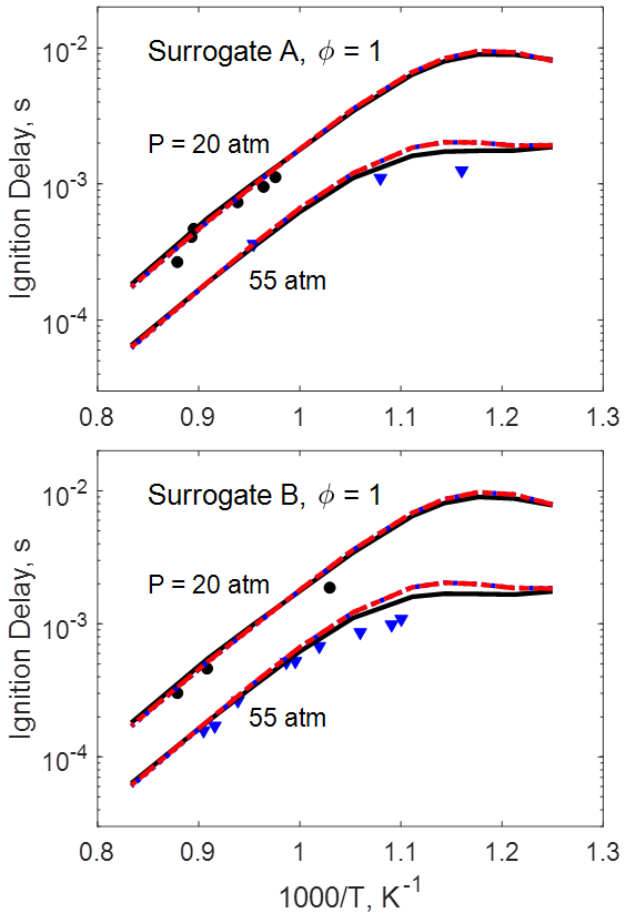

Figure 4-15. Ignition delay times of stoichiometric Surrogate A/air and Surrogate B/air under pressure of 20 and 55 atm. Symbols denote the experimental measurements by Gauthier et al.[106], solid, dashed and dot-dashed lines show the numerical results based on the detailed, skeletal and reduced mechanism respectively.

Exhaust gas recirculation also affects the ignition delay time of the diluted fuel/air mixtures. The dilution's effects on the ignition delay time were studied by Gauthier et al.[106] for Surrogate A under 20 atm with EGR rates of 20% and 30%. The EGR rate is defined as the mole fraction of the exhaust gas in the fuel/air/exhaust gas mixtures, where the distilled water was used as the exhaust gas. Figure 4-16 shows that the numerical results based on reduced, skeletal and detailed mechanisms are almost the same and they can excellently predict the experimental results

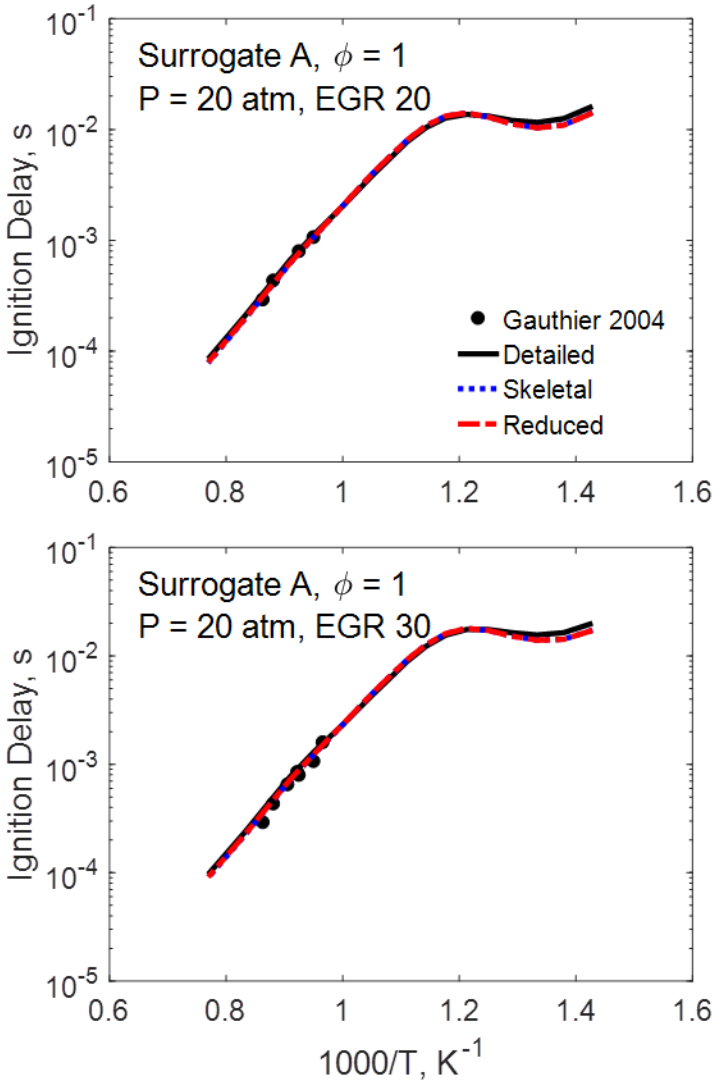

Figure 4-16. Ignition delay times of Surrogate A under 20 atm with EGR rates of 20% and 30%.

The ignition delay times of Surrogate A have also been experimentally investigated by Kukkadapu et al.[107] at intermediate to low temperatures in a rapid compression machine under 20 and 40 bar. These experimental data are compared with the reduced, skeletal and detailed models in Figure 4-17. For both pressures, the reduced and skeletal models again give satisfactory results for a variety of initial temperatures.

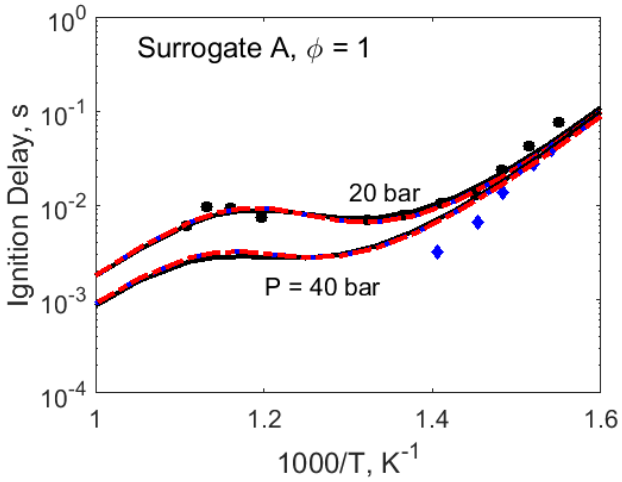

Figure 4-17. Ignition delay times of Surrogate A under 20 and 40 bar and intermediate to low temperatures. Symbols denote the experimental measurements by Kukkadapu et al.[107], solid, dashed and dot-dashed lines show the numerical results based on the detailed, skeletal and reduced mechanism respectively.

Table 4-2. TPRF surrogates investigated in Javed et al. [108]

Surrogate	iso-Octane	n-Heptane	Toluene	RON	MON	Sensitivity
TPRF 70	42.48	36.23	21.29	70	66	4
TPRF 80	39.85	28.58	31.57	80	74.3	5.7
TPRF 91	36.58	19.31	44.1	91	83.4	7.6
TPRF 97.5	11.52	18.04	70.44	97.5	86.6	10.9

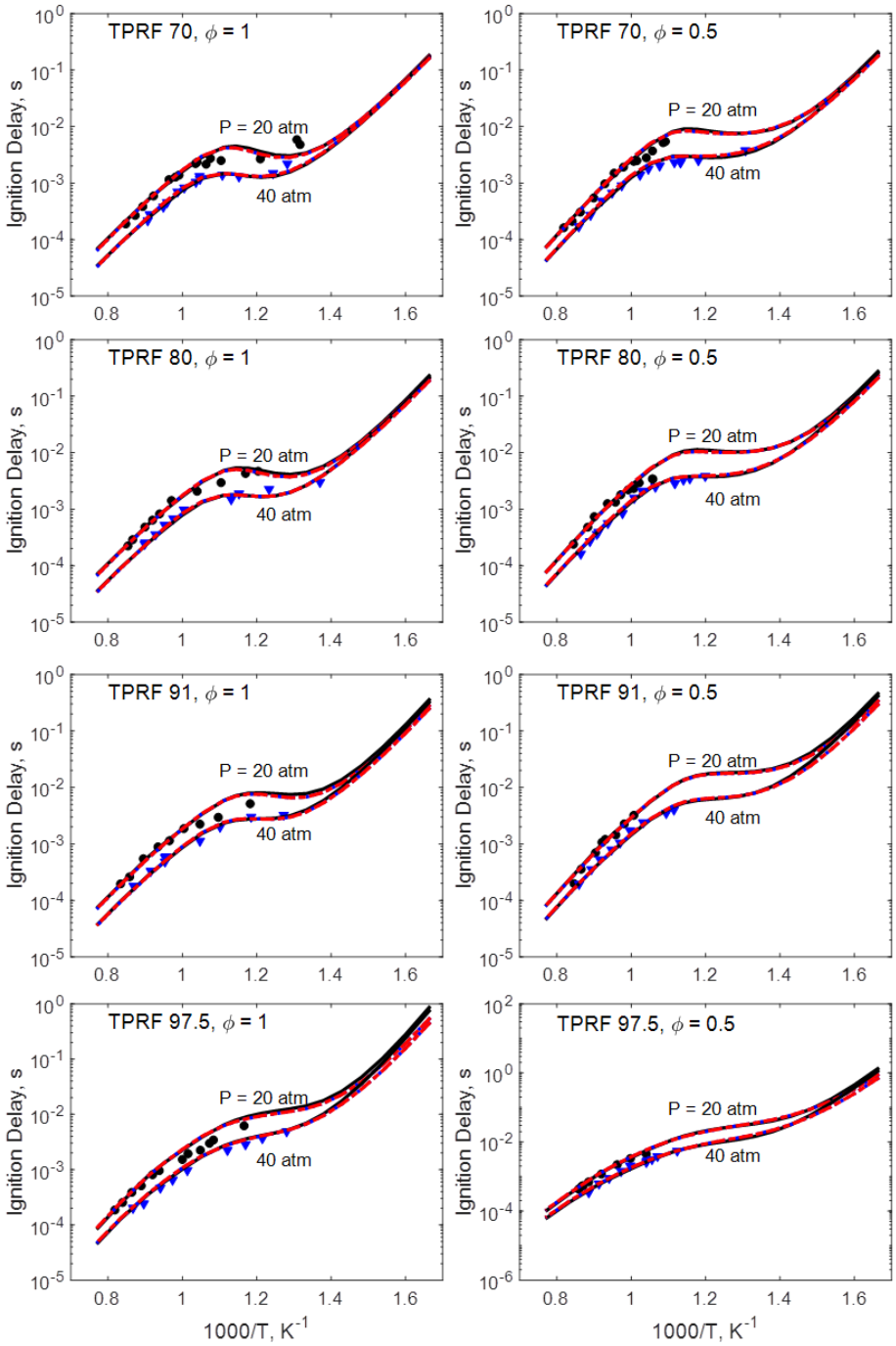

Figure 4-18. Ignition delay times of the four surrogates investigated in Javed et al.[108]. Symbols denote the experimental measurements by Javed et al.[108], solid, dashed and dot-dashed lines show the numerical results based on the detailed, skeletal and reduced mechanism respectively.

Lastly, the experimental data reported by Javed et al.[108] was used in the validation. The four surrogates investigated in Javed et al.'s work are listed in Table 4-2. The RON, MON, and octane sensitivity are calculated based on the correlations developed by Kalghatgi et al.[60]. Table 4-2 shows that the surrogates are formulated over a wide range of octane numbers (RON: 70–97.5) with varying degrees of sensitivity (S: 4–11). For brevity, the surrogate blends will be referred to as TPRF xx where xx represents the RON of the surrogate blend. From Figure 4-18 we can find that the numerical results based on the reduced, skeletal and detailed mechanisms are almost identical and they both predict the experimental data with a very good accuracy.

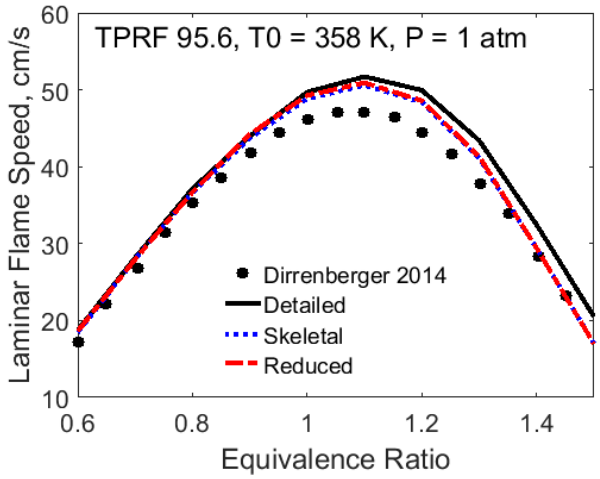

Figure 4-19. Laminar flame speed of TPRF 95.6 under atmospheric pressure and 358 K.

The laminar flame speeds of an n-heptane/iso-octane/toluene blend (13.7%/42.9%/43.4% by the liquid volume fraction) have been experimentally investigated by Dirrenberger et al. [97] under atmospheric pressure and inital temperature of 358 K. For convenience, the surrogate is referred to as TPRF 95.6 since its RON is 95.6 based on the formulation proposed by Kalghatgi et al.[60]. The experimental data are presented in Figure 4-19 with the computed flame speeds based on the reduced, skeletal and detailed mechanisms. It can be seen that for lean to stoichiometric

conditions the reduced and skeletal mechanism reproduce the detailed mechanism results and accurately predict the experimental data and for rich conditions there exist acceptable deviations between the numerical results and the experimental data.

4.3.1.4. Validations of Gasoline Surrogates and Ethanol Mixtures

The reduced and skeletal models are validated in this subsection to show their capability in predicting the ignition delay time and flame speed of mixtures of gasoline surrogates and ethanol.

For mixtures of PRF and ethanol, Fikri et al.[109] measured the ignition delay time of n-heptane/iso-octane/ethanol blend (18%/62%/20% by liquid volume) under a pressure of 10, 30, and 50 atm. The results are shown in Figure 4-20 and we can find that the reduced, skeletal and detailed mechanism results show very good agreement and predict the experimental data very well.

For mixtures of TPRF and ethanol, Cancino et al.[110] have experimentally determined the ignition delay times of n-heptane/iso-octane/toluene/ethanol blend (10.2%/37.8%/12%/40% by liquid volume). The results are displayed in Figure 4-21. It's observed that the reduced and skeletal models satisfactorily reproduce the detailed model's behavior and ignition delay times are slightly overestimated in the low-temperature range compared with the experimental data.

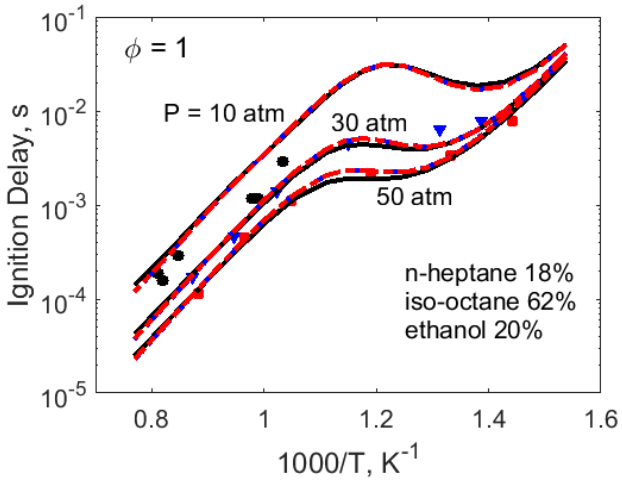

Figure 4-20. Ignition delay times of n-heptane/iso-octane/ethanol blend (18%/62%/20% by liquid volume) at a pressure of 10, 30, and 50 atm. Symbols denote the experimental measurements by Fikri et al.[109], solid, dashed and dot-dashed lines show the numerical results based on the detailed, skeletal and reduced mechanism respectively.

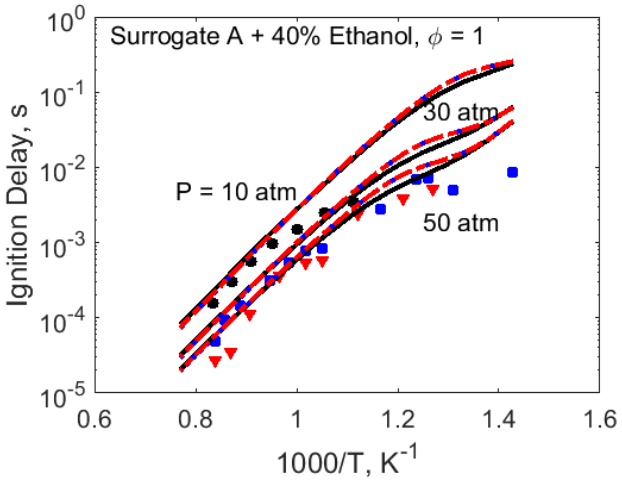

Figure 4-21. Ignition delay times of stoichiometric mixtures of n-heptane/iso-octane/toluene/ethanol blend (10.2%/37.8%/12%/40% by liquid volume) and air under 10, 30, and 50 bar. Symbols denote the experimental measurements by Cancino et al.[110], solid, dashed and dot-dashed lines show the numerical results based on the detailed, skeletal and reduced mechanism respectively.

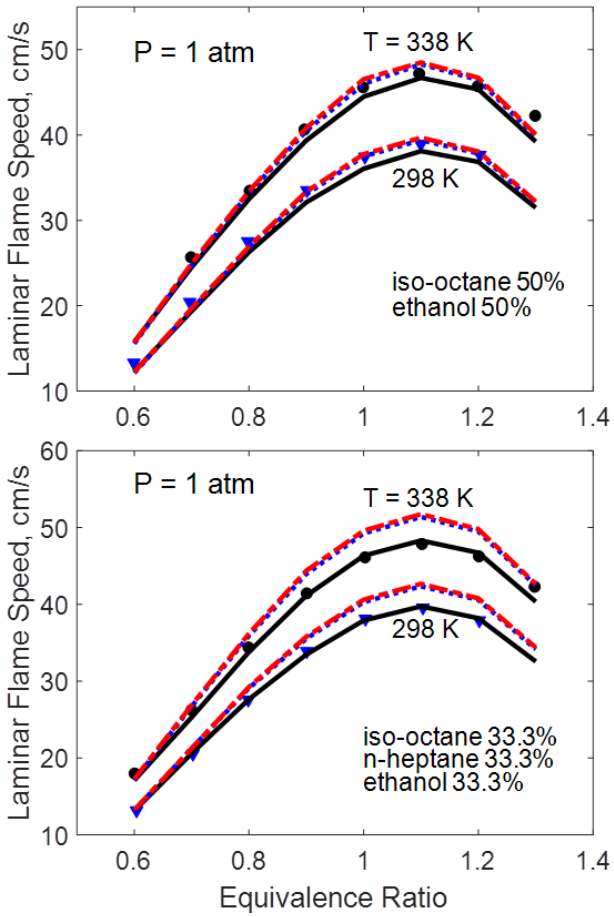

Figure 4-22. Laminar burning velocities of the mixture EO and EHO at 298 and 338 K. Symbols denote the experimental measurements by van Lipzig et al.[96], solid, dashed and dot-dashed lines show the numerical results based on the detailed, skeletal and reduced mechanism respectively.

Laminar burning velocities of the mixture EO (iso-octane/ethanol – 50%/50% by volume fraction) and EHO (n-heptane/iso-octane/ethanol – 33.3%/33.3%/33.3% by volume fraction) under initial temperatures of 298 and 338 K are investigated by van Lipzig et al.[96] The experimental results are shown in Figure 4-22 against the simulation results based on reduced, skeletal and detailed mechanisms. The figure shows that for mixture EO the skeletal mechanism results match the detailed mechanism results and experimental data very well. For mixture EHO,

the reduced and skeletal mechanisms slightly overestimate the flame speed and the worst-case error is only around 6%.

Laminar flame speeds have been reported by Dirrenberger et al.[97] for mixtures of 15% ethanol in volume fraction with TPRF 95.6. These data have been experimentally investigated under atmospheric pressure and initial temperature of 358 K. The numerical results using the reduced, skeletal and detailed models are compared with the experimental measurements in Figure 4-23. For the lean and stoichiometric conditions, an excellent agreement can be observed between experiments and simulations. While for rich conditions, there exist acceptable deviations between the reduced, skeletal and detailed mechanisms.

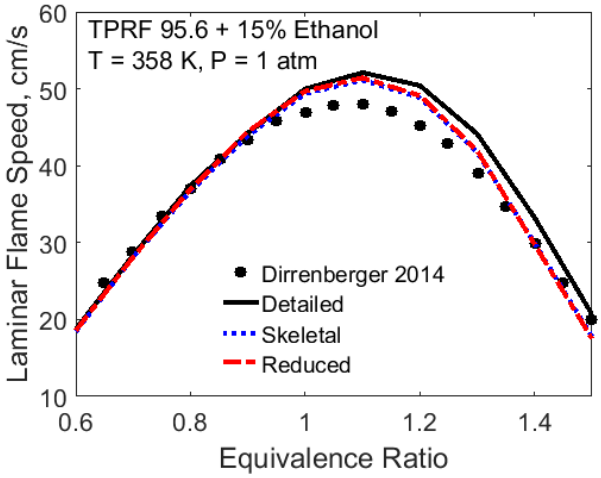

Figure 4-23. Laminar flame speeds for mixtures of 15% volume fraction ethanol with TPRF 95.6 under atmospheric pressure and initial temperature of 358 K.

4.3.2. Validations in SI Engine Simulations

The obtained 165 species skeletal mechanism was further validated against the experimental data in predicting the critical compression ratio (i.e., CR at knock onset) under RON/MON conditions, for PRF60 and PRF80 blends in a CFR engine. The simulation results and

discussions were obtained from Dr. Pinaki Pal at Argonne National Laboratory [111]. A commercial 3D CFD code, CONVERGE (version 2.3) [112], was used to perform the numerical simulations and the hybrid approach combining G-equation and multi-zone [113] models was employed for combustion modeling.

In order to differentiate between knocking and non-knocking cases, the criterion of a threshold knock intensity (KI) was employed. Based on previous studies [114,115], a value of 0.5 bar was used so that KI>0.5 bar corresponded to a knocking condition. KI was quantified using the maximum amplitude of pressure oscillations (MAPO) [116]. To determine MAPO, the local pressure trace at the monitor point placed near the edge of the combustion chamber was considered for knock characterization, since it has the highest peak pressure fluctuation based on observations. Fast Fourier transform of the local pressure trace was calculated and higher frequencies in the range 4–20 kHz [117,118] (relevant to knock) were filtered out using a band-pass filter. Subsequently, the knocking pressure was obtained by computing the inverse fast Fourier transform of the filtered pressure signal and its maximum absolute value was defined as the MAPO.

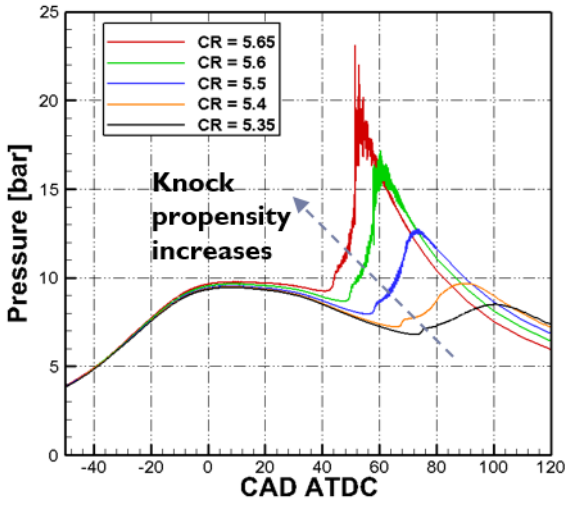

Figure 4-24. Local in-cylinder pressures for stoichiometric PRF60/air at different CRs under RON condition

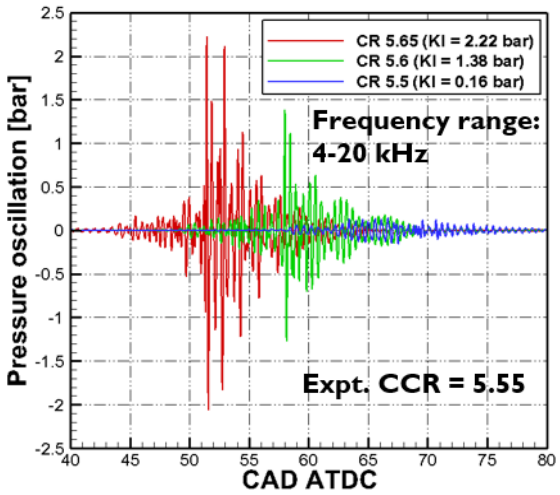

Figure 4-25. Pressure oscillations at different CRs under RON condition for stoichiometric PRF60/air.

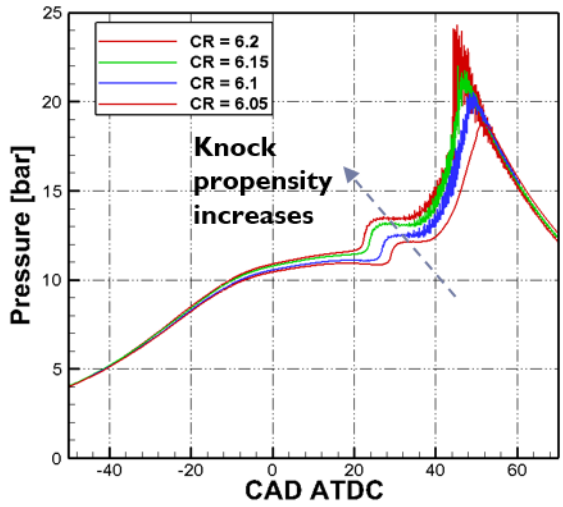

Figure 4-26. Local in-cylinder pressures for stoichiometric PRF80/air at different CRs under RON condition

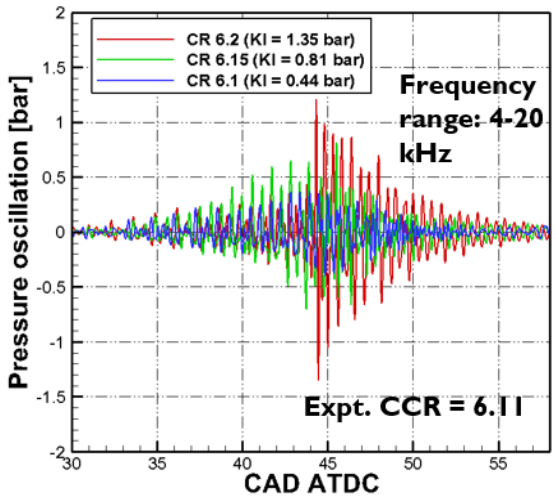

Figure 4-27. Pressure oscillations at different CRs under RON condition for stoichiometric PRF80/air.

Figure 4-24 depicts the temporal evolution of local in-cylinder pressure for stoichiometric PRF60/air with CR range from 5.35 to 5.65 under RON operating condition. It can be seen that a clear transition from no knock to knock occurred with an increase in CR. The results of the corresponding MAPO analysis in Figure 4-25 show that KI = 0.16 bar for CR = 5.5 and KI = 1.38 bar for CR = 5.6, indicating that the critical CR would lie in between these two CRs. On the other hand, the experimental value of critical CR is 5.55, which also falls in the same CR interval, indicating that the numerical results are in good agreement with experiments within the uncertainty of 0.1 CR units. The local pressure traces corresponding to the parametric cases corresponding to stoichiometric PRF80/air at RON condition are presented in Figure 4-26. Furthermore, it is observed in Figure 4-27 that the critical CR is bracketed by CR = 6.1 (KI = 0.44 bar) and CR = 6.15 (KI = 0.81 bar), whereas the corresponding experimental value is 6.11, indicating, the transition to knock is again predicted very well, within the uncertainty of 0.05 CR units. Similar

trends were observed for the two PRF blends under MON conditions as well, with the numerical values of critical CR corresponding well to the experiments.

The numerical study in this subsection demonstrates that the skeletal model is able to capture the critical compression ratio for different fuels (PRFs in this case) and under different operating conditions (RON and MON).

4.4. Conclusions

In the present study, compact 118-species reduced mechanism and 165-species skeletal mechanism were developed from the detailed LLNL mechanism, for gasoline and gasoline/ethanol blend surrogates, employing the DRG, DRGASA, isomer lumping and LQSSA reduction techniques, under a wide range of temperature, pressure and equivalence ratio conditions, including low-temperature ignition in the NTC region.

Validations of the reduced and skeletal mechanism were performed against the detailed mechanism and the available experimental data in ignition delay time and laminar flame speed. Reasonable accuracy was observed for the reduced and skeletal mechanism despite the large extent of reduction by almost a factor of around 10. Furthermore, the skeletal model was shown to accurately capture the critical compression ratio measured by the experiment under RON/MON conditions, for PRF60 and PRF80 blends in a CFR engine. The above satisfactory validation results demonstrate the suitability of the reduced and skeletal models for engine simulations.

Chapter 5. Skeletal Mechanisms for Gasoline/Bio-blend-stock Surrogates and an Upgraded Solver for Chemical Integration

5.1. Introduction

As introduced in Chapter 1, fossil fuel is dominant in energy generation at present and in the foreseeable future. However, as a non-renewable energy source, the formation of fossil fuel requires millions of years, and based on current consumption rates it is estimated that fossil fuel resources will be depleted in about 60 years [1]. Renewable and clean alternative fuels have received increasing attention as a means to mitigate the problem. Among the clean energy sources, biofuels are a promising replacement of fossil fuels because it is sustainable and commonly available. As reviewed in section 1.2.4, new bio-based fuels are one of the focuses in the CoOptima research and eight candidate bio-blend-stocks shown in Figure 1-4 were identified for further assessing by using engine simulations.

To investigate whether octane numbers are sufficient to describe a fuel's knock-limited performance under boosted SI conditions regardless of the fuel's chemical compositions, three bio-blend-stocks including di-isobutylene (DIB), anisole and iso-butanol were selected in the engine simulations. The composition of the corresponding TPRF/bio-blend-stock surrogates, henceforth referred to as DIB30, Isobutanol10, and Anisole20, respectively, are listed in Table 5-1. However, the detailed mechanism for transport fuels developed by LLNL consists of 2878 species and 12839 reactions [74], such that, the mechanism reduction is necessary to allow for the compressive detailed chemistry to be applicable in 3-D engine combustion CFD.

Table 5-1. Volume composition of the gasoline/bio-blend-stock surrogates

(Vol%)	DIB30	Isobutanol10	Anisole20
iso-octane	28.55	49.83	29.02

n-heptane	17.47	10.76	14.23
toluene	23.98	29.41	36.75
DIB	30.00	0	0
iso-butanol	0	10.00	0
anisole	0	0	20.00

In the present study, separate mechanisms were developed by using DRG, LEP and sensitivity analysis for different TPRF/bio-blend-stock surrogates to minimize the number of species and reactions in each skeletal mechanism. To accelerate the ignition delay evaluations during the sensitivity analysis, an upgraded solver which utilizes the analytical Jacobian and sparse matrix operations was developed. Lastly, the obtained skeletal mechanisms were validated against the detailed mechanism in ignition delay time, extinction residence time and flame speed.

5.2. Methodology

The reductions were based on a large set of reaction states sampled over the parameter range of pressure from 1 to 80 atm and equivalence ratio from 0.8 to 1.2. For the extinction applications an inlet temperature of 700 K is used for perfectly stirred reactors (PSR), and for the ignition applications initial temperatures range from 600 to 1600 K are used for auto-ignition, covering the low-temperature chemistry which is important for engine combustion.

DRG features a linear reduction time, such that it is highly efficient in reducing extremely large mechanisms, therefore was employed as the first step in the present reduction. H radical was selected as the starting species and the worst-case error tolerance was set to be approximately 30%.

Then LEP is applied in species elimination to minimize the species for sensitivity analysis. In LEP, the PSR reaction states are sampled with inlet temperatures range from 600 to 1600 K including both the ignition and extinction states and a 0.1 threshold is specified in H radical.

Subsequently, to achieve the largest extent of reduction, sensitivity analysis, which measures the actual reduction errors, is implemented, such that species can be safely removed if the measured error is smaller than the user-specified threshold value. In the sensitivity analysis, the parameters of interest e.g. ignition delay time and extinction residence time of PSR, are directly targeted, and a worst-case relative error of 20% was specified in the present reductions, such that the obtained skeletal mechanisms remain high accuracy.

The challenge in sensitivity analysis is the time consuming iterative evaluation of the target global parameters, especially ignition delay time for large-sized mechanisms. A single ignition delay time evaluation of a mechanism with around 1000 species takes tens of minutes while using the commonly used SENKIN program [119], such that the entire sensitivity analysis can take up to several months even with parallelization.

The most time-consuming parts of a typical implicit solver for auto-ignition problems, e.g. SENKIN, are the Jacobian evaluation and the LU factorization in solving the linear system. The time complexity of the Jacobian evaluation using the brute force numerical perturbation and LU factorization are $O(K^2)$ and $O(K^3)$ respectively, where K is the number of species in the mechanism. Since the Jacobian evaluation involves enormous exponential evaluations in computing the reaction rate, it dominant the solver time, therefore the overall time complexity of the solver is $O(K^2)$.

To accelerate the integration solver, the analytical Jacobian can be applied to speed up the Jacobian matrix evaluations. Analytical Jacobian evaluation subroutines can be automatically generated for any specific mechanism by an in house generator and have shown to achieve a linear time complexity [80]. However in the sensitivity analysis due to the change in the species and reactions, it is inflexible to dynamically generate mechanism-specific Jacobian evaluation

subroutines. Therefore, a general subroutine, which can be applied to any mechanism, compatible with the CHEMKIN data structure, is developed to analytically evaluate the Jacobian matrix given the CHEMKIN workspace of the mechanism and the reaction state including species mole concentration and temperature.

Both the general Jacobian subroutine and the mechanism-specific Jacobian subroutine can accurately evaluate the Jacobian matrix with different advantages. The former can be applied to any mechanism, which is more feasible. Therefore, it suits better in the sensitivity analysis where the mechanism is perturbed or the dynamic adaptive chemistry (DAC) [120] where skeletal mechanisms are generated based on local conditions. On the other hand, the latter is computationally faster due to the optimized reaction coefficient evaluations. Such that it is preferred when the mechanism is fixed, for example, post-processing or simulations with a consistent mechanism.

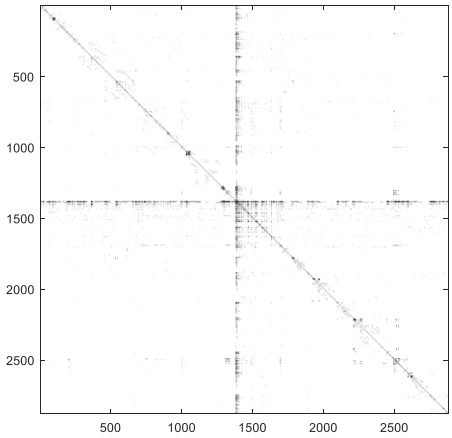

Figure 5-1. The sparsity structure of the Jacobian of the detailed mechanism.

It is further observed that the Jacobian matrix is highly sparse especially for large mechanisms, for example, the sparsity structure of the Jacobian matrix for the 2878 species detailed mechanism is displayed in Figure 5-1, where the black and white pixels indicate nonzero and zero values respectively. To achieve the largest extent of sparsity, the density and total mole concentration are assumed to be functions of temperature only [121]. It can be observed in Figure 5-1 that only a small portion of the Jacobian contains nonzero values, therefore a sparse ordinary differential equations (ODE) solver LSODES [122] can be applied to improve the computational efficiency. Compared to LSODE [123], LSODES determines the sparsity structure of the Jacobian matrix and uses parts of the Yale Sparse Matrix Package (YSMP) [124] to solve the linear systems that arise, by a sparse (direct) LU factorization method.

After applying the upgraded solver which is a combination of LSODES and the analytical Jacobian subroutine, the computational time of sensitivity analysis is dramatically reduced, for example from months to several days for the present reduction works. Lastly skeletal mechanisms with 150, 121, 129 species, henceforth referred to as sk150, sk121, and sk129, are obtained for DIB30, Isobutanol10, and Anisole20 respectively.

5.3. Results and Discussion

5.3.1. Performance of the Upgraded Solver in Auto-ignition

LSODES with analytical Jacobian is compared with LSODE with numerical Jacobian in constant pressure auto-ignition with nine different mechanisms (from 32 to 2878 species) listed in Table 5-2. Involved flame conditions, including fuel, pressure, equivalence ratio, and initial temperature in auto-ignition are also shown in Table 5-2. The simulation time for auto-ignition is

five times the ignition delay. All the numerical codes are implemented in FORTRAN and compiled with the Intel FORTRAN Compiler and tested on Intel CPUs.

Table 5-2. Mechanisms tested in the Jacobian evaluations.

Number of Species	Number of Reactions	Ref.	Fuel	Pressure (atm)	Initial temperature (K)	Equivalence ratio
32	206	[125]	C2H4	1	1000	1
111	784	[80]	CH4	1	1000	1
165	839	[49]	PRF80	1	1000	1
233	959	[13]	Iso-octane	1	1000	1
339	1690	[126]	PRF80	1	1000	1
654	2827	[4]	n-Heptane	1	1000	1
840	3606	[127]	Iso-octane	1	1000	1
1389	5935	[64]	PRF80	1	1000	1
2878	12839	[128]	PRF80	1	1000	1

Average per-step computational costs for LSODE and LSODES, as well as the Jacobian evaluation using analytical subroutine and numerical perturbation, are shown in Figure 5-2. It can be observed that the computational time scales as a linear function of the mechanism size for the analytical Jacobian evaluation while scales as a quadratic function of the mechanism size for the numerical perturbation. Furthermore, the analytical evaluation is more than two orders of magnitude faster than the numerical perturbation for mechanisms with more than 100 species. It is also observed that the numerical Jacobian evaluation dominant the computational time of the LSODE solver, which thus also scales as a quadratic function of the mechanism size. Furthermore, it is seen that the overall computational time of the LSODES solver scale as a linear function of the mechanism size, which can be explained by the fact that the number of the floating-point operation for sparse matrix scales as a linear function of the number of non-zero elements in the matrix [129], which is a linear function of the number of species. Lastly, it is observed that the

speedup factor can reach more than 100 for a mechanism with more than 1000 species after applying the analytical Jacobian and sparse matrix technique.

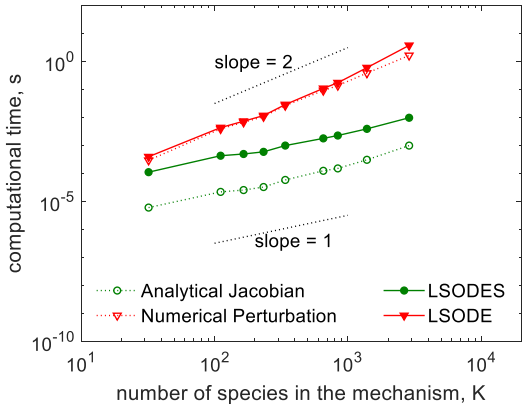

Figure 5-2. Average per-step computational cost of the solvers and the Jacobian evaluations and the number of non-zero elements in the Jacobian matrix for different sized mechanisms.

5.3.2. Skeletal Mechanism Validations

Since no experimental data for the TPRF/bio-blend-stock blends are available presently, the obtained skeletal mechanisms were then validated against the detailed mechanism. Firstly the three mechanisms were validated against the detailed mechanism in homogeneous applications including auto-ignition and PSR. The auto-ignition simulations were performed using the upgraded solver described in section 5.2 and the PSR simulations were performed using CHEMKIN-II [130].

The left panel of Figure 5-3 shows the ignition delay time as a function of initial temperature calculated using the detailed mechanism and sk150 for DIB30/air under different pressures and equivalence ratios covered in the reduction process, while the right panel of Figure 5-3 further compares the temperature profiles in PSR, calculated at different residence times using the sk150 and the detailed mechanism.

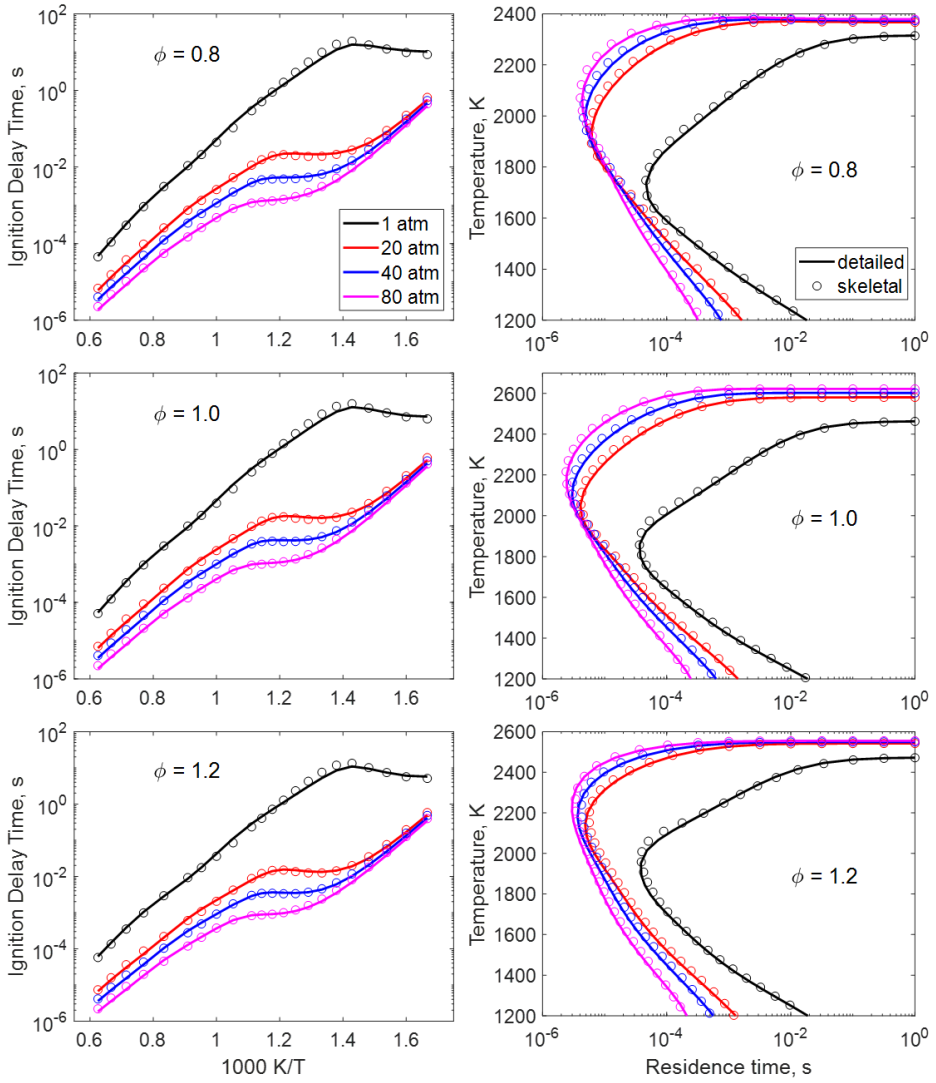

Figure 5-3. Ignition delay time of constant-pressure auto-ignition as a function of initial temperature (left panels) and PSR *S*-curves at inlet temperature of 700K (right panels) for DIB30/air under different pressures and equivalence ratios, calculated with the detailed mechanism (lines) and sk150 (symbols), respectively.

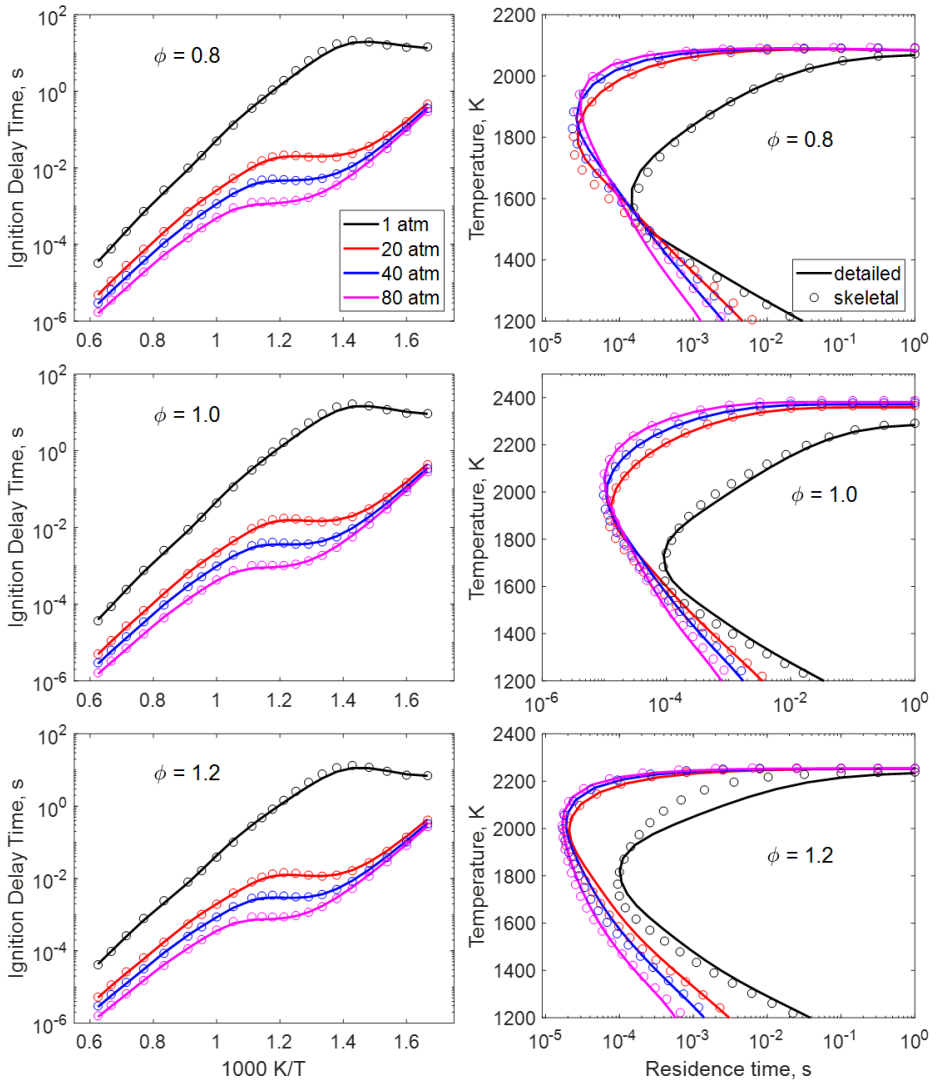

Figure 5-4. Ignition delay time of constant-pressure auto-ignition as a function of initial temperature (left panels) and PSR *S*-curves at inlet temperature of 700K (right panels) for Isobutanol10/air under different pressures and equivalence ratios, calculated with the detailed mechanism (lines) and sk121 (symbols), respectively.

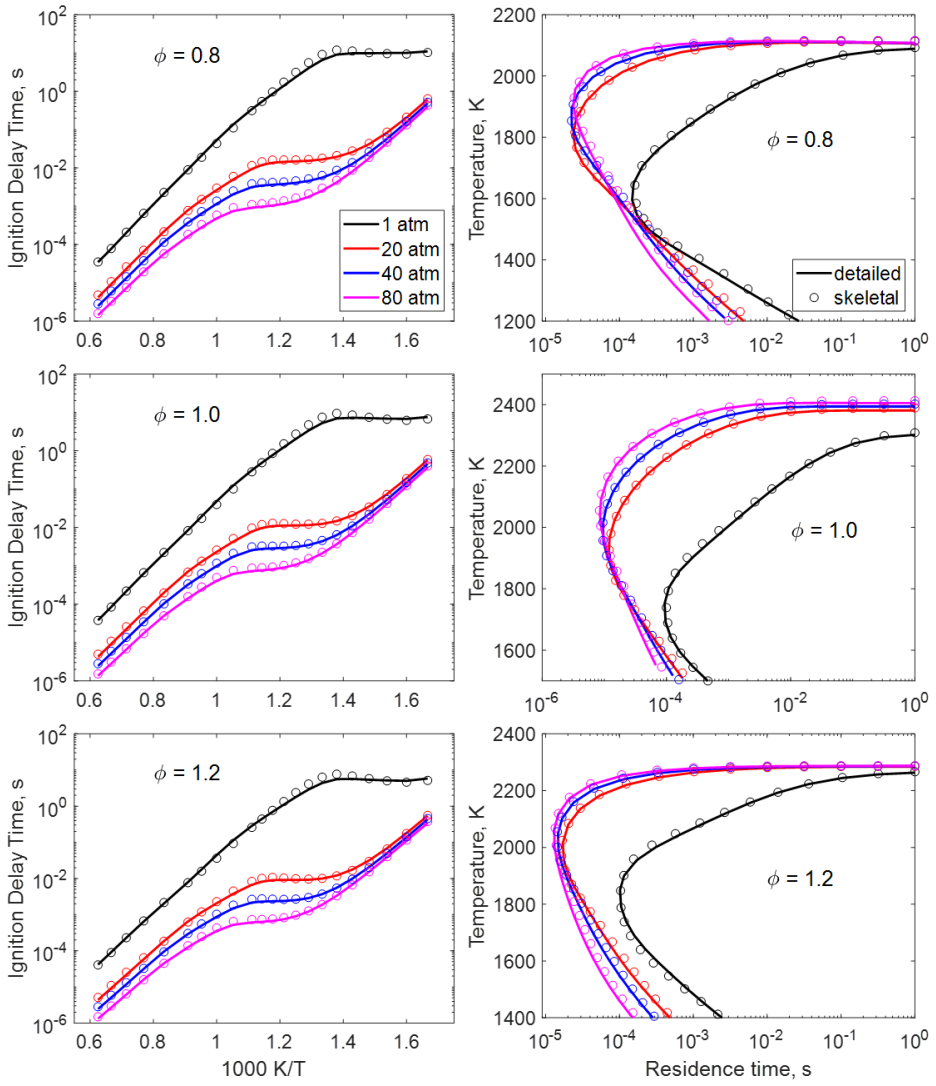

Figure 5-5. Ignition delay time of constant-pressure auto-ignition as a function of initial temperature (left panels) and PSR *S*-curves at inlet temperature of 700K (right panels) for Anisole20/air under different pressures and equivalence ratios, calculated with the detailed mechanism (lines) and sk129 (symbols), respectively.

It can be observed in Figure 5-3 that sk150 matches quite well against the detailed mechanism under almost all the displayed conditions, with a worst-case error of 19.96% for ignition delay time and a worst-case error of 14.57% for the extinction residence time in PSR. It is further observed that the middle branch of the temperature profiles shows relatively larger discrepancies.

This is because the current combustion model employed in engine simulations was based on reaction states sampled from the upper branches as stated in Section 5.2, while the conditions on middle branches are less relevant to steady-state combustion. Figure 5-4 and Figure 5-5 further show the ignition delay time and PSR temperature profile validation results for sk129 and sk121. It can be observed that both sk129 and sk121 show high accuracy in the ignition and extinction problem. The worst-case errors of the three skeletal mechanisms are listed in

Table 5-3, showing that all the three skeletal mechanisms satisfied the 20% error tolerance specified in the sensitivity analysis.

Table 5-3. Worst case error of the three skeletal mechanisms in different applications

	Ignition delay time	PSR extinction residence time	Flame speed
sk150 (DIB30)	19.96%	14.59%	6.12%
sk121 (Isobutanol10)	16.46%	15.28%	4.64%
sk129 (Anisole20)	19.92%	7.99%	3.08%

Since in engine applications, ignition delay time and flame speed are both of great interest, the skeletal mechanisms are then further validated against the detailed mechanism in flame speed. Figure 5-6 depicts laminar flame speeds of DIB30, Anisole20, and Isobutanol10 at different initial temperatures under unity equivalence ratio and pressure of 40 atm calculated by the skeletal and detailed mechanisms. The flame speed computations were performed using a sparse, iterative flame solver with approximate Jacobian, which has been shown to be two orders of magnitude faster than commonly used codes [131]. Again, predictions of the skeletal mechanisms agree well with those of the detailed mechanism, and the worst-case errors are listed in

Table 5-3. It is seen that the worst-case errors are smaller than 7%, showing a very high accuracy of the skeletal mechanisms.

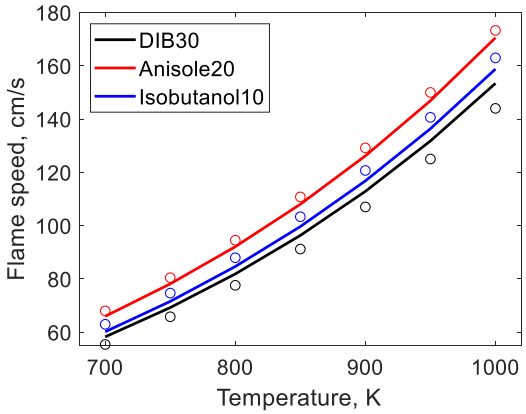

Figure 5-6. Flame speeds of DIB30, Anisole20, and Isobutanol10 at different initial temperatures under unity equivalence ratio and pressure of 40 atm calculated by the skeletal (symbol) and detailed (line) mechanisms, respectively.

5.4. Conclusion

Three skeletal mechanisms with 150, 121, 129 species for DIB30, Isobutanol10 and Anisole20, respectively, including low-temperature chemistry, were developed from the detailed 2878-species LLNL mechanism. The reduction was performed using DRG, LEP and sensitivity analysis. In the sensitivity analysis, a worst-case error of 20% was specified for ignition delay time and extinction residence time in PSR. To expedite the iterative ignition delay evaluations in the sensitivity analysis, an upgraded solver, which is a combination of LSODES and the analytical Jacobian subroutine, was utilized to achieve linear-time integration, resulting in a speedup factor of about 100, and the reduction time is dramatically reduced.

Comprehensive validations of the skeletal mechanisms against the detailed mechanism were next carried out to guarantee their chemical fidelity. The skeletal mechanisms were shown to be versatile and robust since they perform satisfactorily in predicting the ignition delay, extinction

residence time and flame speed. As such these skeletal mechanisms are suitable for accurately capturing end-gas auto-ignition, knocking, as well as flame propagation characteristics in engines.

Chapter 6. Summary and Future Work

The present research was conducted to develop improved reduction strategies and generate accurate reduced mechanisms of gasoline, gasoline/ethanol, and gasoline/bio-blend-stock surrogates for 3-D SI engine simulations. The study is motivated by the extreme sizes of the detailed mechanisms of practical engine fuel surrogates involving thousands of species, and thus the detailed mechanism is prohibited from being directly applied in multi-dimensional engine simulations. Skeletal and reduced mechanisms are therefore developed to enable high fidelity engine simulations that require accurate chemistry to understand complex engine combustion phenomena and to further optimize the engine design to achieve higher efficiency and lower emissions.

First, a method of LEP based on Jacobian analysis is developed for systematic skeletal mechanism reduction. LEP is based on Jacobian analysis to estimate the reduction error in selected target species induced by the elimination of other species. Skeletal mechanisms are obtained by eliminating species that induce negligible worst-case errors to the target species. LEP is compared with DRG and DRGEP on the accuracy of reduction error estimation. It is shown that DRG can effectively control the worst-case error of every species in the skeletal mechanism by assuming that error may not decay in the worst cases along the graph-search paths, while it tends to overestimate the errors in the starting species in average cases, which may retain unnecessary species. As a result, the skeletal mechanism can typically be further reduced if only the starting species are of interest. In contrast, DRGEP assumes geometric error decay along graph-search paths and may overestimate the error decay and subsequently underestimate the reduction errors in species far away from the starting species, resulting in potentially unsafe species-eliminations. Compared with DRG and DRGEP, LEP can overall more accurately estimate the errors in the

target species such that smaller mechanisms can be obtained compared with that from DRG, while unsafe species eliminations are less likely compared with DRGEP. To demonstrate the performance of the LEP method, skeletal mechanisms are derived based on steady-state PSR solutions sampled along the *S*-curves, including both the ignition and extinction reaction states. A 35-species skeletal mechanism is obtained for ethylene/air based on the 111-species USC-Mech II, and a 146-species skeletal mechanism for n-heptane/air is obtained based on a 188-species skeletal mechanism previously developed using DRG. Validation of global flame behaviors, such as PSR ignition and extinction residence time, auto-ignition delay, and laminar flame speed, shows no significant errors further induced by LEP. It is further shown that reaction states sampled from PSR alone, including both the extinction and the ignition turning points, can be adequate to develop reduced mechanisms involving both the fast flame chemistry and the slow ignition chemistry, while such reaction states were sampled from both PSR and auto-ignition in previous studies.

Steady-state PSR provide a simple and effective approach to study ignition and extinction limits of continuous flow combustors, which are associated with the lower and upper turning points on the *S*-curves, respectively. The turning points are typically obtained by using marching-based methods such as arc-length continuation. However, the marching-based solution methods are rather computationally involved and may not be suitable when high computational efficiency and accuracy are required. Therefore, a direct method is developed to accurately and efficiently compute the turning points of PSR by transforming the local optimization problem to solving a set of algebraic equations using Lagrange multipliers. The new set of equations are formulated with the analytic Jacobian of the original PSR equations to achieve adequate accuracy and high numerical efficiency. The direct method is then compared with the continuation method in obtaining the turning points of PSR. It is shown that the direct method can be significantly more

efficient with the accuracy controlled by the Newton solver. Furthermore, an analytical method is proposed to effectively and accurately evaluate the sensitivities of the steady-state PSR solutions. The analytical method is then compared with the numerical perturbation method, demonstrating its validity. The ignition and extinction residence time sensitivities are subsequently compared with the sensitivities of ignition delay time and laminar flame speed. Results show that the reactions controlling the ignition residence time in PSR and ignition delay time are similar, and dominant reactions to the extinction residence time are also important to the flame speed. Therefore the ignition and extinction states of PSR can capture important chemistries to the ignition process and strongly burning flames, which further indicates that by sampling PSR only covering both the ignition and extinction states, controlling kinetics can be identified and comprehensive mechanisms can be obtained by the reduction process.

Then a compact skeletal chemical kinetic mechanism with 165 species and 839 reactions and a 118 species reduced mechanism with lumped reactions were developed for gasoline and gasoline/ethanol surrogates, where TPRF comprised of iso-octane, n-heptane, and toluene serves as the gasoline surrogate. DRG, DRGASA, isomer lumping and LQSSA techniques were employed to reduce the detailed mechanism containing 1389 species and 5935 reactions. Eleven fuel surrogates with different compositions of the TPRF and ethanol components were selected in the sampling process, covering a wide range of octane number and octane sensitivity, such that the skeletal mechanism could be applied to almost all practical gasoline fuels and mixtures of gasoline and ethanol. The reduction was performed for the pressure range of 1-100 atm and equivalence ratio in the range 0.5-1.3, with respect to both homogeneous auto-ignition delay and extinction residence time in perfectly stirred reactors. In addition, the initial temperature range considered for auto-ignition was 750-1800 K, thereby incorporating low-temperature chemistry. The

developed reduced and skeletal mechanisms were extensively validated against the detailed mechanism as well as experimental data available in the literature, including ignition delays and laminar flame speeds for a wide range of surrogate composition since in the SI engine simulations ignition delay time and flame speed are of great interest. Good agreements were observed despite the large extent of reduction by almost a factor of 10. The skeletal model was further validated in predicting the critical compression ratio under RON/MON conditions, for PRF60 and PRF80 blends in a CFR engine. The numerical values of the critical compression ratio agree well to the experiments, demonstrating that the skeletal model is suitable for CFD simulations of engine combustion.

Engine simulations of gasoline/bio-blend-stock surrogates provide a means to optimize engine designs and identify efficient bio-blend-stocks to blend with gasoline. In the present study, three highly reduced skeletal mechanisms for TPRF/DIB, TPRF/Anisole and TPRF/iso-butanol, respectively, were developed for engine simulations by subsequently applying DRG, LEP and sensitivity analysis based on the 2878-species detailed LLNL mechanism. The reductions were based on a large set of reaction states sampled over the parameter range of pressure from 1 to 80 atm, equivalence ratio from 0.8 to 1.2, inlet temperature of 700 K for PSR, and initial temperature from 600 to 1600 K for auto-ignition, covering the low-temperature chemistry which is important for engine combustion. The most time-consuming step in the sensitivity analysis is the iterative evaluations of ignition delay time. To speed up the reduction process, an upgraded solver based on LSODES and analytical Jacobian was employed, such that the overall integration time using the upgraded solver scales as a linear function of the mechanism size. In contrast, the previous integration solver based on numerical Jacobian has a quadratic time complexity. For mechanism with more than 1000 species, a speedup factor of more than 100 can be achieved, such that the

computational time for sensitivity analysis is dramatically reduced, for example from several months to several days in the present case. The skeletal mechanisms were then validated against the detailed mechanism in auto-ignition delay time, extinction residence time of PSR and laminar flame speed. Good agreement between the skeletal mechanisms and detail mechanism indicates that the highly reduced skeletal mechanisms are suitable for engine simulations of TPRF/bio-blend-stock surrogates.

The present study can be extended in the future in the following aspects. 1) Application of LEP in on-the-fly mechanism reduction. 2) Applying the direct method in evaluating the extinction and/or ignition residence time based on the local mixture compositions to provide the critical mixture timescales for advanced turbulent combustion modeling. 3) Further reducing the skeletal mechanisms for engine fuel surrogates to less than 50 species for DNS applications. New reduction strategies will be required for this purpose.

References

[1] BP Statistical Review of World Energy 2019, 2019.
[2] BP Energy Outlook 2019 edition, 2019.
[3] E. Sher, Handbook of Air Pollution From Internal Combustion Engines, Academic Press, 1998.
[4] T. Lu, C.K. Law, Toward accommodating realistic fuel chemistry in large-scale computations, Prog. Energy Combust. Sci. 35 (2009) 192–215.
[5] J.H. Chen, Petascale direct numerical simulation of turbulent combustion - Fundamental insights towards predictive models, Proc. Combust. Inst. 33 (2011) 99–123.
[6] T. Turányi, Sensitivity Analysis of Complex Kinetic Systems. Tools and Applications, J. Math. Chem. 5 (1990) 203–248.
[7] S. Vajda, P. Valko, T. Turanyi, T. Turányi, Principal component analysis of kinetic models, Int. J. Chem. Kinet. 17 (1985) 55–81.
[8] T. Turanyi, T. Turányi, Reduction of large reaction mechanisms, New J. Chem. 14 (1990) 795–803.
[9] B. Bhattacharjee, D.D.A. Schwer, P.I.P. Barton, W.H. Green, Optimally-reduced kinetic models: Reaction elimination in large-scale kinetic mechanisms, Combust. Flame. 135 (2003) 191–208.
[10] S.D. Harris, L. Elliott, D.B. Ingham, M. Pourkashanian, C.W. Wilson, Optimization of reaction rate parameters for chemical kinetic modelling of combustion using genetic algorithms, Comput. Methods Appl. Mech. Eng. 190 (2000) 1065–1090.
[11] H. Wang, M. Frenklach, Detailed reduction of reaction mechanisms for flame modeling, Combust. Flame. 87 (1991) 365–370.
[12] T. Lu, C.K. Law, A directed relation graph method for mechanism reduction, Proc. Combust. Inst. 30 (2005) 1333–1341.
[13] T. Lu, C.K. Law, Linear time reduction of large kinetic mechanisms with directed relation graph: N-Heptane and iso-octane, Combust. Flame. 144 (2006) 24–36.
[14] Z. Luo, T. Lu, M.J. MacIaszek, S. Som, D.E. Longman, A reduced mechanism for high-temperature oxidation of biodiesel surrogates, Energy and Fuels. 24 (2010) 6283–6293.
[15] P. Pepiot-Desjardins, H. Pitsch, An efficient error-propagation-based reduction method for large chemical kinetic mechanisms, Combust. Flame. 154 (2008) 67–81.
[16] W. Sun, Z. Chen, X. Gou, Y. Ju, A path flux analysis method for the reduction of detailed chemical kinetic mechanisms, Combust. Flame. 157 (2010) 1298–1307.
[17] L. Tosatto, B.A. V Bennett, M.D. Smooke, A transport-flux-based directed relation graph method for the spatially inhomogeneous instantaneous reduction of chemical kinetic mechanisms, Combust. Flame. 158 (2011) 820–835.
[18] K. He, I.P. Androulakis, M.G. Ierapetritou, Multi-element flux analysis for the incorporation of detailed kinetic mechanisms in reactive simulations, Energy and Fuels. 24 (2010) 309–317.
[19] P. Zhao, S.M. Nackman, C.K. Law, On the application of betweenness centrality in chemical network analysis: Computational diagnostics and model reduction, Combust. Flame. 162 (2015) 2991–2998.
[20] X.L. Zheng, T.F. Lu, C.K. Law, Experimental counterflow ignition temperatures and reaction mechanisms of 1,3-butadiene, Proc. Combust. Inst. 31 I (2007) 367–375.
[21] R. Sankaran, E.R. Hawkes, J.H. Chen, T. Lu, C.K. Law, Structure of a spatially

developing turbulent lean methane-air Bunsen flame, Proc. Combust. Inst. 31 I (2007) 1291–1298.
[22] K.E. Niemeyer, C.J. Sung, M.P. Raju, Skeletal mechanism generation for surrogate fuels using directed relation graph with error propagation and sensitivity analysis, Combust. Flame. 157 (2010) 1760–1770.
[23] N. Peters, Numerical and Aymptotic Analysis of Systematically Reduced Reaction Schemes for Hydrocarbon Flames, Numer. Simul. Combust. Phenom. (1985) 90–109.
[24] M.D. Smoke, V. Giovangigli, Formulation of the premixed and nonpremixed test problems, Reduc. Kinet. Mech. Asymptot. Approx. Methane-Air Flames. 384 (1991) 1–28.
[25] C.J. Sung, C.K. Law, J.-Y. Chen, An augmented reduced mechanism for methane oxidation with comprehensive global parametric validation, Symp. Combust. 27 (1998) 295–304.
[26] U. Maas, S.B. Pope, Simplifying chemical kinetics: Intrinsic low-dimensional manifolds in composition space, Combust. Flame. 88 (1992) 239–264.
[27] H. Bongers, J.A. Van Oijen, L.P.H. De Goey, Intrinsic low-dimensional manifold method extended with diffusion, Proc. Combust. Inst. 29 (2002) 1371–1378.
[28] Z. Ren, S.B. Pope, The use of slow manifolds in reactive flows, Combust. Flame. 147 (2006) 243–261.
[29] D.A. Goussis, S.H. Lam, A study of homogeneous methanol oxidation kinetics using CSP, Symp. Combust. 24 (1992) 113–120.
[30] S.H. Lam, D.A. Goussis, The CSP method for simplifying kinetics, Int. J. Chem. Kinet. 26 (1994) 461–486.
[31] D.A.GOUSSIS, V. M, An Efficient Iterative Algorithm for the Approximation of the Fast and Slow Dynamics of Stiff Systems, J. Comput. Phys. 214(1) (2006) 316–346.
[32] S.H. Lam, Reduced chemistry-diffusion coupling, Combust. Sci. Technol. 179 (2007) 767–786.
[33] T. Lu, C.K. Law, A criterion based on computational singular perturbation for the identification of quasi steady state species: A reduced mechanism for methane oxidation with NO chemistry, Combust. Flame. 154 (2008) 761–774.
[34] J.C. Keck, Rate-controlled constrained-equilibrium theory of chemical reactions in complex systems, Prog. Energy Combust. Sci. 16 (1990) 125–154.
[35] W.P. Jones, S. Rigopoulos, Rate-controlled constrained equilibrium: Formulation and application to nonpremixed laminar flames, Combust. Flame. 142 (2005) 223–234.
[36] S. Rigopoulos, The Rate-Controlled Constrained Equilibrium (RCCE) Method for Reducing Chemical Kinetics in Systems with Time-Scale Separation, Int. J. Multiscale Comput. Eng. 5 (2008) 11–18.
[37] G. Li, A.S. Tomlin, H. Rabitz, J. Tóth, A general analysis of approximate nonlinear lumping in chemical kinetics. I. Unconstrained lumping, J. Chem. Phys. 101 (1994) 1172–1187.
[38] G. Li, A.S. Tomlin, H. Rabitz, J. Tóth, G. Li, H. Rabitz, J. Tóth, A general analysis of approximate nonlinear lumping in chemical kinetics. II. Constrained lumping, J. Chem. Phys. 101 (1994) 1188–1201.
[39] E. Ranzi, M. Dente, A. Goldaniga, G. Bozzano, T. Faravelli, Lumping procedures in detailed kinetic modeling of gasification, pyrolysis, partial oxidation and combustion of hydrocarbon mixtures, Prog. Energy Combust. Sci. 27 (2001) 99–139.

[40] S.S. Ahmed, Mau, G. Moreac, T. Zeuch, A.S. S., M. F., M. G., Z. T., A comprehensive and compact n-heptane oxidation model derived using chemical lumping, Phys. Chem. Chem. Phys. 9 (2007) 1107–1126.
[41] T.F. Lu, C.K. Law, Strategies for mechanism reduction for large hydrocarbons: n-heptane, Combust. Flame. 154 (2008) 153–163.
[42] P. Pepiot-Desjardins, H. Pitsch, An automatic chemical lumping method for the reduction of large chemical kinetic mechanisms, Combust. Theory Model. 12 (2008) 1089–1108.
[43] C.K. Law, Combustion Physics, Cambridge University Press, New York, USA, 2006.
[44] M.D. Smooke, J. Crump, K. Seshadri, V. Giovangigli, Comparison between experimental measurements and numerical calculations of the structure of counterflow, diluted, methane-air, premixed flames, Symp. Combust. 23 (1991) 463–470.
[45] R. Seiser, H. Pitsch, K. Seshadri, W.J.J. Pitz, H.J. Gurran, H.J. Curran, Extinction and autoignition of n-heptane in counterflow configuration, Proc. Combust. Inst. 28 (2000) 2029–2037.
[46] K. Seshadri, T. Lu, O. Herbinet, S. Humer, U. Niemann, W.J. Pitz, R. Seiser, C.K. Law, Experimental and kinetic modeling study of extinction and ignition of methyl decanoate in laminar non-premixed flows, Proc. Combust. Inst. 32 I (2009) 1067–1074.
[47] C. Ji, E. Dames, Y.L. Wang, H. Wang, F.N. Egolfopoulos, Propagation and extinction of premixed C5-C12 n-alkane flames, Combust. Flame. 157 (2010) 277–287.
[48] C.G. Fotache, T.G. Kreutz, D.L. Zhu, C.K. Law, An experimental study of ignition in nonpremixedcounterflowing hydrogen versus heated air, Combust. Sci. Technol. 109 (1995) 373–393.
[49] Y. Wu, P. Pal, S. Som, T. Lu, A skeletal chemical kinetic mechanism for gasoline and gasoline/ethanol blend surrogates for engine CFD applications, 10th Int. Conf. Chem. Kinet. (2017).
[50] B. Magda, Reduced Mechanism Validation and Analysis Near Extinction Limits of Perfectly Stirred Reactors, 2016.
[51] G.T. Kalghatgi, Developments in internal combustion engines and implications for combustion science and future transport fuels, Proc. Combust. Inst. 35 (2015) 101–115.
[52] G. Kalghatgi, H. Levinsky, M. Colket, Future transportation fuels, Prog. Energy Combust. Sci. 69 (2018) 103–105.
[53] G. Kalghatgi, Knock onset, knock intensity, superknock and preignition in spark ignition engines, Int. J. Engine Res. 19 (2018) 7–20.
[54] J.B. Heywood, Internal combustion engine fundamentals, McGraw-Hill, 1988.
[55] T.J. Wallington, E.W. Kaiser, J.T. Farrell, Automotive fuels and internal combustion engines: a chemical perspective., Chem. Soc. Rev. 35 (2006) 335–47.
[56] Gautam Kalghatgi, Fuel / Engine Interactions, SAE International, Warrendale, Pennsylvania :, 2014.
[57] ASTM Book of Standards - Section 5: Petroleum Products, Lubricants, and Fossil Fuels, American Society of Testing Materials, 2018.
[58] C. V. Naik, W.J. Pitz, C.K. Westbrook, M. Sjöberg, J.E. Dec, J. Orme, H.J. Curran, J.M. Simmie, Detailed Chemical Kinetic Modeling of Surrogate Fuels for Gasoline and Application to an HCCI Engine, in: SAE Tech. Pap. Ser., 2005.
[59] M. Chaos, Z. Zhao, A. Kazakov, P. Gokulakrishnan, M. Angioletti, F.L. Dryer, A PRF + Toluene Surrogate Fuel Model for Simulating Gasoline Kinetics, 5th US Combust. Meet. (2007) 1–19.

[60] G. Kalghatgi, H. Babiker, J. Badra, A Simple Method to Predict Knock Using Toluene, N-Heptane and Iso-Octane Blends (TPRF) as Gasoline Surrogates, SAE. 8 (2015) 2015-01–0757.
[61] T. Wagner, D. Gray, B. Zarah, A.A. Kozinski, Practicality of Alcohols as Motor Fuel, in: SAE Tech. Pap. Ser., 2010.
[62] Jian-Xin Wang, J.-H. Xiao, X.-G. Yan, B.-Q. He, J.-M. Hao, A study on emission characteristics of an EFI engine with ethanol blended gasoline fuels, Atmos. Environ. 37 (2003) 949–957.
[63] M. Al-Hasan, Effect of ethanol-unleaded gasoline blends on engine performance and exhaust emission, Energy Convers. Manag. 44 (2003) 1547–1561.
[64] M. Mehl, W.J. Pitz, C.K. Westbrook, H.J. Curran, Kinetic modeling of gasoline surrogate components and mixtures under engine conditions, Proc. Combust. Inst. 33 (2011) 193–200.
[65] W.R. Leppard, The Chemical Origin of Fuel Octane Sensitivity, in: SAE Tech. Pap. Ser., 2010.
[66] C.K. Westbrook, M. Mehl, W.J. Pitz, M. Sjöberg, Chemical kinetics of octane sensitivity in a spark-ignition engine, Combust. Flame. 175 (2017) 2–15.
[67] G.T. Kalghatgi, Auto-Ignition Quality of Practical Fuels and Implications for Fuel Requirements of Future SI and HCCI Engines, in: SAE Tech. Pap. Ser., 2010.
[68] G.T. Kalghatgi, Fuel Anti-Knock Quality - Part I. Engine Studies, in: SAE Tech. Pap. Ser., 2010.
[69] G.T. Kalghatgi, Fuel Anti-Knock Quality- Part II. Vehicle Studies - How Relevant is Motor Octane Number (MON) in Modern Engines?, in: SAE Tech. Pap. Ser., 2010.
[70] B. Zhang, S.M. Sarathy, Lifecycle optimized ethanol-gasoline blends for turbocharged engines, Appl. Energy. 181 (2016) 38–53.
[71] M.D. Boot, M. Tian, E.J.M. Hensen, S. Mani Sarathy, Impact of fuel molecular structure on auto-ignition behavior – Design rules for future high performance gasolines, Prog. Energy Combust. Sci. 60 (2017) 1–25.
[72] J. Farrell, J. Holladay, R. Wagner, Co-Optimization of Fuels & Engines: Fuel Blendstocks with the Potential to Optimize Future Gasoline Engine Performance: Identification of Five Chemical Families for Detailed Evaluation, 2018.
[73] J. Farrell, J. Holladay, R. Wagner, Fuel Blendstocks with the Potential to Optimize Future Gasoline Engine Performance, NREL TP-5400-69009. (2018).
[74] M. Mehl, K. Zhang, S. Wagnon, G. Kukkadapu, C.K. Westbrook, W.J. Pitz, Y. Zhang, H. Curran, M. Al Rachidi, N. Atef, M.S. Sarathy, A comprehensive detailed kinetic mechanism for the simulation of transportation fuels, in: 10th U.S. Natl. Combust. Meet., 2017: pp. 1–6.
[75] Z. Luo, Development of Reduced Chemical Kinetics for Combustion Simulations with Transportation Fuels, Ph.D. Thesis. (2013).
[76] Y. Xin, C.J. Sung, C.K. Law, A mechanistic evaluation of Soret diffusion in heptane/air flames, Combust. Flame. 159 (2012) 2345–2351.
[77] M. Nishioka, C.K. Law, T. Takeno, A flame-controlling continuation method for generating S-curve responses with detailed chemistry, Combust. Flame. 104 (1996) 328–342.
[78] G. Balakrishnan, M.D. Smooke, F.A. Williams, A numerical investigation of extinction and ignition limits in laminar nonpremixed counterflowing hydrogen-air streams for both

elementary and reduced chemistry, Combust. Flame. 102 (1995) 329–340.
[79] J.O. Olsson, O. Lindgren, O. Andersson, Efficient Formation of Numerical Jacobian Used in Flame Codes, Combust. Sci. Technol. 77 (1991) 319–327.
[80] H. Wang, X. You, A. V. Joshi, S.G. Davis, A. Laskin, F. Egolfopoulos, C.K. Law, USC Mech Version II. High-Temperature Combustion Reaction Model of H2/CO/C1-C4 Compounds, (2007).
[81] R. Shan, T. Lu, Ignition and extinction in perfectly stirred reactors with detailed chemistry, Combust. Flame. 159 (2012) 2069–2076.
[82] A.R. Conn, N.I.M. Gould, P.L. Toint, Trust Region Methods, Society for Industrial and Applied Mathematics, Philadelphia, USA, 2000.
[83] A. Bhagatwala, Z. Luo, H. Shen, J.A. Sutton, T. Lu, J.H. Chen, Numerical and experimental investigation of turbulent DME jet flames, Proc. Combust. Inst. 35 (2015) 1157–1166.
[84] R. Shan, T. Lu, A bifurcation analysis for limit flame phenomena of DME/air in perfectly stirred reactors, Combust. Flame. 161 (2014) 1716–1723.
[85] Z. Luo, M. Plomer, T. Lu, S. Som, D.E. Longman, S.M. Sarathy, W.J. Pitz, A reduced mechanism for biodiesel surrogates for compression ignition engine applications, Fuel. 99 (2012) 143–153.
[86] T. Lu, C.K. Law, Systematic approach to obtain analytic solutions of quasi steady state species in reduced mechanisms, J. Phys. Chem. A. 110 (2006) 13202–13208.
[87] K. Fieweger, R. Blumenthal, G. Adomeit, Self-Ignition of S.I. Engine Model Fuels: a Shock Tube Investigation at High Pressure, Combust. Flame. 109 (1997) 599–619.
[88] D.F. Davidson, B.M. Gauthier, R.K.R. Hanson, Shock tube ignition measurements of iso-octane/air and toluene/air at high pressures, Proc. Combust. Inst. 30 (2005) 1175–1182.
[89] H.S.P.S. Shen, J. Vanderover, M.A. Oehlschlaeger, A shock tube study of iso-octane ignition at elevated pressures: The influence of diluent gases, Combust. Flame. 155 (2008) 739–755.
[90] H.K. Ciezki, G. Adomeit, Shock-tube investigation of self-ignition of n-heptane-air mixtures under engine relevant conditions, Combust. Flame. 93 (1993) 421–433.
[91] B.M. Gauthier, D.F. Davidson, R.K. Hanson, Shock tube measurements of ignition delay times in n-heptane, gasoline and surrogate fuel mixtures, in: Int. Symp. Combust. Abstr. Work. Posters, 2004: p. 483.
[92] S.G. Davis, C.K. Law, Determination of and Fuel Structure Effects on Laminar Flame Speeds of C1 to C8 Hydrocarbons, Combust. Sci. Technol. 140 (1998) 427–449.
[93] O. Kwon, M. Hassan, G. Faeth, Flame/Stretch Interactions of Premixed Fuel-Vapor/O<inf>2</inf>/N<inf>2</inf> Flames, J. Propuls. Power. 16 (2000).
[94] Y. Huang, C.J. Sung, J.A. Eng, Laminar flame speeds of primary reference fuels and reformer gas mixtures, Combust. Flame. 139 (2004) 239–251.
[95] K. Kumar, J.E. Freeh, C.J. Sung, Y. Huang, Laminar Flame Speeds of Preheated iso-Octane/O2/N2 and n-Heptane/O2/N2 Mixtures, J. Propuls. Power. 23 (2007) 428–436.
[96] J.P.J. Van Lipzig, E.J.K. Nilsson, L.P.H. De Goey, A.A. Konnov, Laminar burning velocities of n-heptane, iso-octane, ethanol and their binary and tertiary mixtures, Fuel. 90 (2011) 2773–2781.
[97] P. Dirrenberger, P.A. Glaude, R. Bounaceur, H. Le Gall, A.P. Da Cruz, A.A. Konnov, F. Battin-Leclerc, Laminar burning velocity of gasolines with addition of ethanol, Fuel. 115 (2014) 162–169.

[98] T. Hirasawa, C. Sung, A. Joshi, Z. Yang, H. Wang, C.K. Law, Determination of laminar flame speeds using digital particle image velocimetry: Binary Fuel blends of ethylene, n-Butane, and toluene, Proc. Combust. Inst. 29 (2002) 1427–1434.
[99] C. Huang, V. Golovitchev, A. Lipatnikov, Chemical model of gasoline-ethanol blends for internal combustion engine applications, (2010).
[100] D. Bradley, R. a. Hicks, M. Lawes, C.G.W. Sheppard, R. Woolley, The Measurement of Laminar Burning Velocities and Markstein Numbers for Iso-octane – Air and Iso-octane – n- Heptane – Air Mixtures at Elevated Temperatures and Pressures in an Explosion Bomb, Combust. Flame. 115 (1998) 126–144.
[101] S. Jerzembeck, N. Peters, Measurements of Laminar Flame Velocity and Markstein Length for Standard Gasoline and a Corresponding Reference Fuel Mixture (PRF87), SAE Int. (2007) 448–455.
[102] J. Beeckmann, L. Cai, H. Pitsch, Experimental investigation of the laminar burning velocitiesof methanol, ethanol, n-propanol, and n-butanol at high pressure, Fuel. 117 (2014) 340–350.
[103] Z. Zhao, J.P. Conley, a Kazakov, F.L. Dryer, Burning velocities of real gasoline fuel at 353 K and 500 K, SAE-Transactions. 112 (2003) 2624–2629.
[104] Z. Zhao, A. Kazakov, J. Li, F.L. Dryer, Dilution Effect on the Laminar Flame Speed of Propane/Air, Combust. Sci. Technol. 176 (2004) 1705–1723.
[105] M. Hartmann, I. Gushterova, M. Fikri, C. Schulz, R. Schießl, U. Maas, Auto-ignition of toluene-doped n-heptane and iso-octane/air mixtures: High-pressure shock-tube experiments and kinetics modeling, Combust. Flame. 158 (2011) 172–178.
[106] B.M. Gauthier, D.F. Davidson, R.K. Hanson, Shock tube determination of ignition delay times in full-blend and surrogate fuel mixtures, Combust. Flame. 139 (2004) 300–311.
[107] G. Kukkadapu, K. Kumar, C.J. Sung, M. Mehl, W.J. Pitz, Autoignition of gasoline and its surrogates in a rapid compression machine, Proc. Combust. Inst. 34 (2013) 345–352.
[108] T. Javed, C. Lee, M. AlAbbad, K. Djebbi, M. Beshir, J. Badra, H. Curran, A. Farooq, Ignition studies of n-heptane/iso-octane/toluene blends, Combust. Flame. 171 (2016) 223–233.
[109] M. Fikri, J. Herzler, R. Starke, C. Schulz, P. Roth, G.T. Kalghatgi, Autoignition of gasoline surrogates mixtures at intermediate temperatures and high pressures, Combust. Flame. 152 (2008) 276–281.
[110] L.R. Cancino, M. Fikri, A.A.M. Oliveira, C. Schulz, Autoignition of gasoline surrogate mixtures at intermediate temperatures and high pressures: Experimental and numerical approaches, Proc. Combust. Inst. 32 I (2009) 501–508.
[111] P. Pal, Personal Communication, 2017.
[112] Convergent Science, CONVERGE 2.3 Theory Manual, Convergent Science, Middleton, WI, 2016.
[113] A. Babajimopoulos, D.N. Assanis, D.L. Flowers, S.M. Aceves, R.P. Hessel, A fully coupled computational fluid dynamics and multi-zone model with detailed chemical kinetics for the simulation of premixed charge compression ignition engines, Int. J. Engine Res. 6 (2005) 497–512.
[114] G. Kalghatgi, I. Algunaibet, K. Morganti, On Knock Intensity and Superknock in SI Engines, SAE Int. J. Engines. 10 (2017) 1051–1063.
[115] S. Breda, A. D'Adamo, S. Fontanesi, N. Giovannoni, F. Testa, A. Irimescu, S. Merola, C. Tornatore, G. Valentino, CFD Analysis of Combustion and Knock in an Optically

Accessible GDI Engine, SAE Int. J. Engines. 9 (2016) 641–656.
[116] G.T. Kalghatgi, M. Golombok, P. Snowdon, Fuel Effects on Knock, Heat Release and "CARS" Temperatures in a Spark Ignition Engine, Combust. Sci. Technol. 110–111 (1995) 209–228.
[117] G. Brecq, J. Bellettre, M. Tazerout, A new indicator for knock detection in gas SI engines, Int. J. Therm. Sci. 42 (2003) 523–532.
[118] G. Brecq, O. Le Corre, Modeling of in-cylinder pressure oscillations under knocking conditions: Introduction to pressure envelope curve, (2005).
[119] A. Lutz, R. Kee, SENKIN: A FORTRAN program for predicting homogeneous gas phase chemical kinetics with sensitivity analysis, Sandia Natl. Lab. Rep. (1988).
[120] L. Liang, J.G. Stevens, J.T. Farrell, A dynamic adaptive chemistry scheme for reactive flow computations, Proc. Combust. Inst. 32 I (2009) 527–534.
[121] C. Xu, Y. Gao, Z. Ren, T. Lu, A sparse stiff chemistry solver based on dynamic adaptive integration for efficient combustion simulations, Combust. Flame. 172 (2016) 183–193.
[122] P.N. Brown, A.C. Hindmarsh, Reduced storage matrix methods in stiff ODE systems, Appl. Math. Comput. 31 (1989) 40–91.
[123] K. Radhakrishnan, A.C. Hindmarsh, Description and use of LSODE, the Livemore Solver for Ordinary Differential Equations, 1993.
[124] S.C. Eisenstat, H.C. Elman, M.H. Schultz, A.H. Sherman, The (New) Yale Sparse Matrix Package, in: Elliptic Probl. Solvers, Academic Press, 1984: pp. 45–52.
[125] Z. Luo, C.S. Yoo, E.S. Richardson, J.H. Chen, C.K. Law, T. Lu, Chemical explosive mode analysis for a turbulent lifted ethylene jet flame in highly-heated coflow, Combust. Flame. 159 (2012) 265–274.
[126] L. Cai, H. Pitsch, Optimized chemical mechanism for combustion of gasoline surrogate fuels, Combust. Flame. 162 (2015) 1623–1637.
[127] M. Mehl, H. Curran, Chemical kinetic modeling of component mixtures relevant to gasoline, Eur. Combust. Meet. (2009) 1–6.
[128] O. Herbinet, W.J. Pitz, C.K. Westbrook, Detailed chemical kinetic oxidation mechanism for a biodiesel surrogate, Combust. Flame. 154 (2008) 507–528.
[129] O. Østerby, Z. Zlatev, Direct Methods for Sparse Matrices, DAIMI Rep. Ser. 9 (2016).
[130] R.J. Kee, F.M. Rupley, J. a Miller, CHEMKIN-II: A FORTRAN chemical kinetics package for the analysis of gas phase chemical kinetics, Sandia Natl. Lab. Rep. (1989) 3–164.
[131] S. Lapointe, R.A. Whitesides, M.J. McNenly, Sparse, iterative simulation methods for one-dimensional laminar flames, Combust. Flame. (2019) 23–32.